Alma Mater Studiorum – Università di Bologna

Dipartimento di Fisica e Astronomia
Corso di Laurea Magistrale in Astrofisica e Cosmologia

Analytic models of self-gravitating rotating gaseous tori with central black hole

Tesi di laurea

Presentata da:
Stefano Sotira

Relatore:
Chiar.mo Prof. Carlo Nipoti

Correlatore:
Chiar.mo Prof. Luca Ciotti

Anno Accademico 2021-2022

Abstract

In this thesis project, I present stationary models of rotating fluids with toroidal distributions that can be used to represent the active galactic nuclei (AGN) central obscurers, i.e. molecular tori (Combes et al., 2019), as well as geometrically thick accretion discs, like advection-dominated accretion flow (ADAF) discs (Narayan and Yi, 1995b) or Polish doughnuts (Abramowicz, 2005). In particular, I study stationary rotating systems with a more general baroclinic distribution (with a vertical gradient of the angular velocity), which are often more realistic and less studied, due to their complexity, than the barotropic ones (with cylindrical rotation), which are easier to construct. The thesis is structured as follows. In the introduction, I show an outline of the astrophysical systems, to which these models could be applied. Systems with toroidal distribution are present on small scales, like the thick accretion discs around the black holes, and on larger scales, like the molecular tori around the AGN or the gas in the galactic nuclei. Analytical models of these components are uncommon in literature. Observational data suggest that molecular tori are clumpy systems or dominated by turbulent pressure. The stationary fluid models that I present can also be interpreted as discrete systems of gas clouds: in this case the pressure support is not given by thermal pressure but by the velocity dispersion of the random motion of the small clouds that compose the tori.

In the thesis, I compute analytically the main intrinsic and projected properties of the tori based on the potential-density pairs of Ciotti and Bertin (2005), described by the power-law density $\rho \propto R^2(R^2+z^2)^{-\alpha/2}$. I study the density distribution and the resulting gravitational potential for different values of α, in the range $2 < \alpha < 5$. For the same models, I compute the circular velocity and the surface density of the systems when seen face-on and edge-on. I then apply the stationary Euler equations to obtain rotational velocity and temperature distributions of the self-gravitating models in the absence of an external gravitational potential.

In the thesis I also consider the power-law tori with the presence of a central black hole in addition to the gas self-gravity, and solving analytically the stationary Euler equations, I compute how the properties of the system are modified by the black hole and how they vary as a function of the black hole mass.

Finally, applying the Solberg-Høiland criterion, I show that these baroclinic stationary models are linearly stable in the absence of the black hole. In the presence of the black hole I derive the analytical condition for stability, which depends on α and on the black hole mass. I also study the stability of the tori in the hypothesis that they are permeated by a weak magnetized field (Balbus, 1995), finding that they are always unstable to this instability, which can be seen as a generalization of the magneto-rotational instability.

Contents

Introduction

The study of rotating fluids is essential in astrophysics. Their applications spread over a big range of astrophysical sizes. On small scales, there are rotating stars and accretion discs around compact objects. Increasing the scale there are molecular tori of active galactic nuclei (AGN), gaseous structures in galactic nuclei, like resonant rings or spiral arms, up to the galactic gaseous discs, extra-planar gas, and galactic coronae. On very large scales rotation could be important for the intracluster medium. The construction of axisymmetric stationary models is useful for all these applications.

The usual approach with axisymmetric rotating models is to consider an angular velocity stratified on cylinders. The cylindrical rotation works relatively well for many astrophysical objects and the advantage is the ease of the construction of these kinds of models. Considering a model with a rotation velocity that depends only on the cylindrical radius means making particular assumptions about the macroscopic distribution of the gas. The Poincaré-Wavre theorem, as we will see in the following brief fluid dynamics review, states that an axisymmetric stationary rotating system with a cylindrical rotation has a particular distribution of the pressure and the density, in practice the surfaces of equal pressure and equal density coincide, i.e. the system is barotropic. The theorem holds also in the opposite direction, if a system has a pressure distribution that depends only on the density distribution, therefore it follows that the angular velocity of the system depends only on the cylindrical radius. In these special systems, we can simplify the Euler equation by considering an effective potential. The Euler equation of the stationary rotating fluid takes the same form as the hydrostatic equilibrium equation.

On the other hand, considering an angular rotation with a vertical gradient of the angular velocity is often more suitable and realistic for many astrophysical situations. Of course, considering such type of velocity distribution is more complex and these models are very little studied. Following the statement of the Poincaré-Wavre theorem, a system with an angular velocity that depends both on the cylindrical radius R and the vertical coordinate z has a different distribution of the pressure and the density. These types of systems are called baroclinic, they have a pressure distribution that depends on the density and the temperature. Therefore the surfaces of equal density and equal pressure do not coincide, and it

is not possible to define an effective potential.

Rotating stationary models with an angular velocity that varies vertically are useful to describe systems with a sizeable height, where the cylindrical rotation can fail, especially in the regions at a certain height above the equatorial plane. Limiting to gaseous systems, for example, two types of astrophysical objects in which the baroclinic distribution can be expected, are the hot galactic coronae and gaseous toroidal systems, like the central obscurer around the black hole or the geometrically thick accretion discs. Innovative works on this topic are Barnabè et al. (2006) and Sormani et al. (2018). These papers present the construction of stationary baroclinic models and their application to the galactic coronae.

Models of thick accretion discs around compact objects, such as advection dominated accretion flows (ADAF) discs (Narayan and Yi, 1995a,b) and the so-called Polish doughnuts (Abramowicz, 2005), have been studied so far especially after the work of Narayan and Yi (1995b), mainly focusing on the accretion flow and often simplifying the dynamics of the stationary rotation at larger radii. Whereas analytic dynamical models of dusty molecular tori obscuring the central regions of the active galactic nuclei are very uncommon in literature. With the advent of high resolution observations with the Atacama Large Millimeter/submillimeter Array[1] (ALMA), the possibilities of observing the central region of AGN are open (Combes et al., 2019). With the high resolution observations of the CO emission it is possible to resolve molecular structures of $10 - 30$ pc and with the combined use of the spectra, it is possible to derive the rotation and the velocity dispersion of the gas. The observation of the morphologies and the kinematics of the AGN molecular obscurer needs the presence of dynamical models to understand the nature of these components.

We recall that in astrophysical systems the pressure support is not necessarily due to the thermal pressure. In reality, the pressure support can be due to turbulent pressure generated by the velocity dispersion of the turbulent motion of the gas. The millimeter spectra suggest that molecular tori have a high velocity dispersion comparable with the rotational velocity of the system (Combes et al., 2019). Therefore the pressure support in these systems is provided by the velocity dispersion rather than the temperature, which for the systems considered is very low.

On the other hand, the X-rays observations predict, in some cases, a little covering factor for the central absorber (García-Bernete et al., 2019) and so suggest the possibility that the torus is clumpy like a discrete system composed of small clouds . In this case, it is not the velocity dispersion of the gas that causes the thickness of the rotating system, but the velocity dispersion of the random motion of the small clouds.

In this work, I present rotating stationary fluid models, which have analytic potential-density pairs derived by Ciotti and Bertin (2005). The potential-density

[1] https://www.almaobservatory.org/en/

pairs resolve the Poisson equation, i.e. the potential is generated by the density distribution and describe the self-gravity of the system. The density distribution has a power-law form with a toroidal geometry, with a power-law index α that can assume values in the range $2 < \alpha < 5$. I study analytically the main physical characteristics of the potential-density pairs, compute the dynamical properties of the stationary models in the self-gravitating case and with the addition of a central black hole. I then study the linear stability of the systems also when the gas is permeated by a week magnetic field, for different values of α. These toroidal models could be applied to the thick accretion discs around the black hole, and the dusty molecular tori that obscure the central parts of the AGNs.

In particular the thesis are structured as follows:

- In chapter 1, I describe the observational properties of the molecular tori, especially based on Combes et al. (2019). Then I review the theoretical characteristics of the accretion discs models.

- In chapter 2, I describe very briefly a few concepts of fluid dynamics, that are useful in the following. In particular, I focus on the Poincaré-Wavre theorem and the nature of the pressure supports.

- In chapter 3, I describe the power-law tori potential-density pairs properties, and compute the projected surface density for the system as seen face-on and edge-on.

- In chapter 4, I compute the rotational velocity and temperature distributions of the power-law tori, applying the axisymmetric stationary Euler equation in the presence of self-gravity, without an external potential.

- In chapter 5, I study the models obtained with the addition of a central black hole.

- In chapter 6, I apply the Solberg-Høiland criterion (Tassoul, 1978) to study the stability against linear axisymmetric perturbations, in the presence and in the absence of a central black hole.

- In Chapter 7, I study the stability of the systems in the presence of a weak magnetic field (Balbus, 1995).

At the end of chapters 3, 4, and 5 I show, as examples, model tori in physical units, constructed to broadly resemble the observed molecular tori of AGN. This will only be an illustration of a possible application and not a proper fit of the models to the observational data.

In conclusion I present all the obtained results and discuss future perspectives of the work.

Chapter 1

Toroidal systems in astrophysics

Toroidal shapes have been proposed to explain the observational characteristics of different astrophysical environments. Mainly, the tori are proposed like central obscurers of active galactic nuclei or thick accretion discs in some accretion conditions around black holes or neutron stars. In this brief introductory chapter, we outline the observed or theoretically expected features of this class of astrophysical objects.

1.1 Molecular tori

The 1% of galaxies in the Universe show an emission much greater than the thermal emission from their stars. These galaxies host an active galactic nucleus (AGN), one of the most energetic phenomena in the Universe, produced by the accretion on the supermassive black hole at the center of the galaxies.

The physical models of these systems (Antonucci and Miller, 1985; Urry and Padovani, 1995) involve, among others, the following components: a supermassive black hole that accretes from an accretion disc and, on larger scale, a dusty molecular torus that absorbs most of the radiation. Inside the torus, near the black hole, there are very compact clouds that rotate rapidly due to the strong black hole gravitational potential and produce broad emission lines: this region is called broad-line region (BLR). Farther from the black hole, in the ionization cones, where the radiation is not absorbed by the molecular torus, there are gaseous clouds that emit narrow emission lines: this region is called the narrow-lines region (NLR).

AGN are observed in two categories, type 1 that show both the BLR and the NLR, and type 2 with only the NLR. The unification paradigm proposes that in type 2 AGN the BLR is obscured by the molecular torus along the line of sight, so the system is seen almost edge-on. Whereas in type 1 AGN the system and thus the torus are seen face-on and the observer can see both the NLR and the BLR, which is not obscured. From this geometrical considerations, initially,

the existence of a toroidal obscurer has been proposed. From the characteristics of the extinction and the emission in the infra-red, it has been understood that the tori are composed by molecular gas and dust. The expected tori have sizes of $3-30$ pc, thus they are so small that it has not been possible to resolve them until now. Recently, with the high resolution observations of the CO emission detected with ALMA, it has been possible to resolve the torus structure in different nearby galaxies (Combes et al., 2019).

The nuclei of these nearby active galaxies show the presence of structures, with size of order of magnitude $0.1-1$ kpc, with different morphologies: some of them are resonant rings, others are spiral arms (Combes et al., 2019). These components are composed by molecular gas and are star forming regions: some of them host a starburst. Inner structures around the central black hole are morphologically and kinematically decoupled from the larger structures. The inner structures are identified as the molecular tori. The tori are almost always concentric with the AGN point source, but they are off center with respect to the larger structures and are not aligned with the galaxy disc. This suggests that the black hole with the torus oscillates around the mass barycenter of the galaxy. In several cases there are dust lanes that connect the tori with the inner edge of the spiral arms or rings.

Combes et al. (2019) observed several central molecular tori in nearby galaxies with AGN. We take this paper as reference for the physical observational properties of the tori. The measured radii of the tori are in the range of $6-27$ pc. The column densities of molecular hydrogen are in the range of $10^{23.5}-10^{25.3}$ numbers of particles per centimeter squared.

The range of estimated masses of the tori is of $\sim 1-4\times10^7 M_\odot$. The masses are not correlated with the stellar masses of the galaxies and are slightly anticorrelated with the power of the AGN. The tori host central black holes with mass in the range $10^{6.6}-10^{7.7}\ M_\odot$. Therefore comparing the tori and the black holes masses, we expect that the self-gravity of the torus is not negligible with respect to the central black hole. In fact, the tori and the black holes gravitational fields are comparable, at least for the sample studied by Combes et al. (2019). Fig. 1.1 shows the molecular tori of NGC 1672 and NGC 1365 observed by Combes et al. (2019). The first is seen almost edge-on, the second almost face-on. In the first panels a measure of the density distribution is plotted. The rotational velocity and the velocity dispersion of the gas are plotted in the middle and in the right panels, respectively. We note that rotation velocity has an order of magnitude of tens km s^{-1}. The velocity dispersion has the same order of magnitude, but it is everywhere slightly lower.

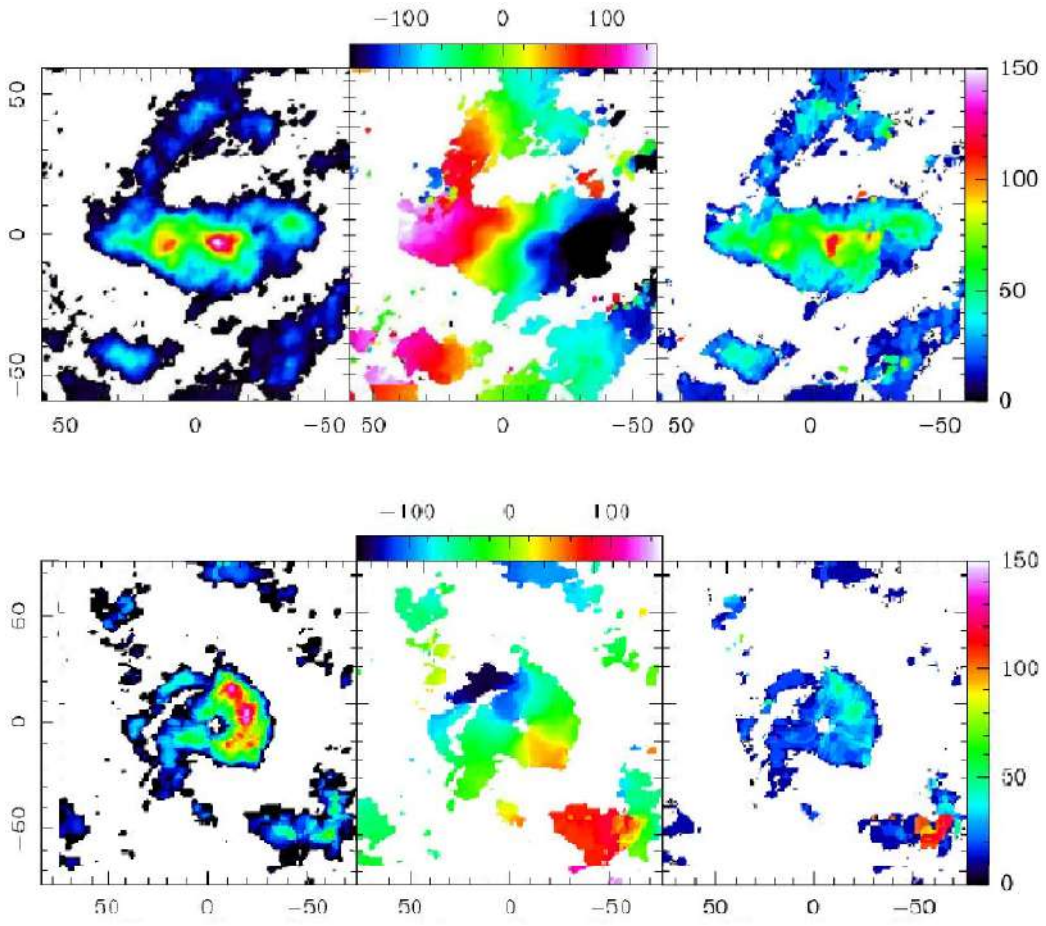

Figure 1.1: Flux of the CO(3-2) line (left), line-of-sight rotation velocity (middle), and line-of-sight velocity dispersion (right), for the central molecular tori of NGC 1672 (top) and NGC 1365 (bottom). The x and y axis are in parsec. In the left panel, red colors indicate larger flux. The velocity color scales are in km s^{-1}. Figures taken from Combes et al. (2019)

1.2 ADAF discs

In this section, we describe briefly the expected characteristics of the thick accretion discs around black holes or neutron stars. In the 80', Paczyńsky, Abramowicz, Rees, and others began the description of accretion objects with a toroidal geometry (Paczyński and Wiita, 1980; Paczyński, 1982; Abramowicz et al., 1980; Rees et al., 1982). The accretion disc models proposed by Paczyński and Abramowicz were later called Polish doughnuts (Abramowicz, 2005). Those proposed by Rees are referred to as ions tori.

In the 90' Narayan and Yi presented their models of advection dominated accretion flow (ADAF) discs (Narayan and Yi, 1995a,b). The models presented by Narayan and Yi renewed the interest on these types of accretion objects, which were studied in great detail in the following years.

Without entering in the details of the different models, here we discuss only the main characteristics that these types of accretion discs should have. In practice, the ADAF discs do not efficiently radiate energy, thus the discs do not cool and the heat is stored as internal energy. Due to this stored energy the temperature in the disc is very high and the thermal pressure enhances the vertical size of the disc. The structure has a height H similar to the radius R, i.e has a ratio $H/R \simeq 1$. Therefore the structure is torodoial and this is why the power-law tori models presented in this work could be applied to these types of accretion discs. Due to the low density the gas is optically thin. The ADAF discs are less luminous than the geometrically thin, optically thick discs because the energy is not radiated away but it is advected into the black hole. Despite the super-Eddington accretion rate that these accretion discs can have, this does not imply necessarily a very high accretion rate. About the thermodynamics of the gas, the temperature is very high and the gas is ionized. The model considers gas with decoupled temperature for ions and electrons. The temperature of the electron found by Narayan and Yi (1995b) is $T_e = 10^9 - 10^{10}$ for accretion discs around super massive black holes, whereas for neutron stars $T_e = 10^{8.5} - 10^9$. The ions temperature can reach $T_i = 10^{10} - 10^{11}$.

Rees et al. (1982) proposed that the toroidal structure with funnels close to the rotational axis of the black hole can drive the formation of radio jets through the presence of a strong magnetic field anchored to the torus. Therefore it is thought that the geometrically thick, and optically thin discs are present almost in all the radio-loud AGN. But the presence of the ADAF or the standard geometrically thin, optically thick discs (Shakura and Sunyaev, 1973) it is not still clearly associated to a type of AGN. However, this is a simplified subdivision because in reality there are several different kinds of accretion discs. Whether the accretion discs can evolve from a type into another or what kind of accretion is associated to different phenomena is still matter of debate.

Fig. 1.2 (top) shows the isodensity contours of a ADAF disc model (Narayan

and Yi, 1995a). Fig. 1.2 (bottom) shows the geometry in the meridional plane of the toy-model proposed by Paczyński (1998). Fig. 1.3 shows the scheme of the possibility of the creation of radio jets (top), and the contours of equal temperature (bottom) of the Rees' ions torus. These figures illustrate the resemblance of some models of geometrically thick accretion discs with the dynamical models that we present in this work.

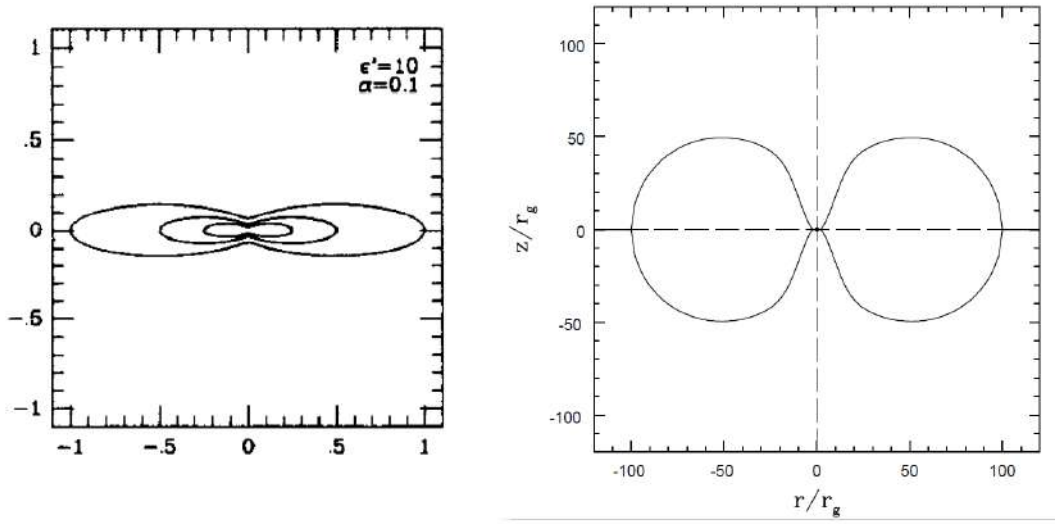

Figure 1.2: Left: Isodensity contours in the meridional plane of a advection dominated accretion flow disc model of Narayan and Yi (Narayan and Yi, 1995a). Right: Geometry in the meridional plane of the toy model of accretion disc presented by Paczyński (Paczyński, 1998). $r_g \equiv 2GM/c^2$, where M is the black hole mass, c is the light speed and G is the gravitational constant.

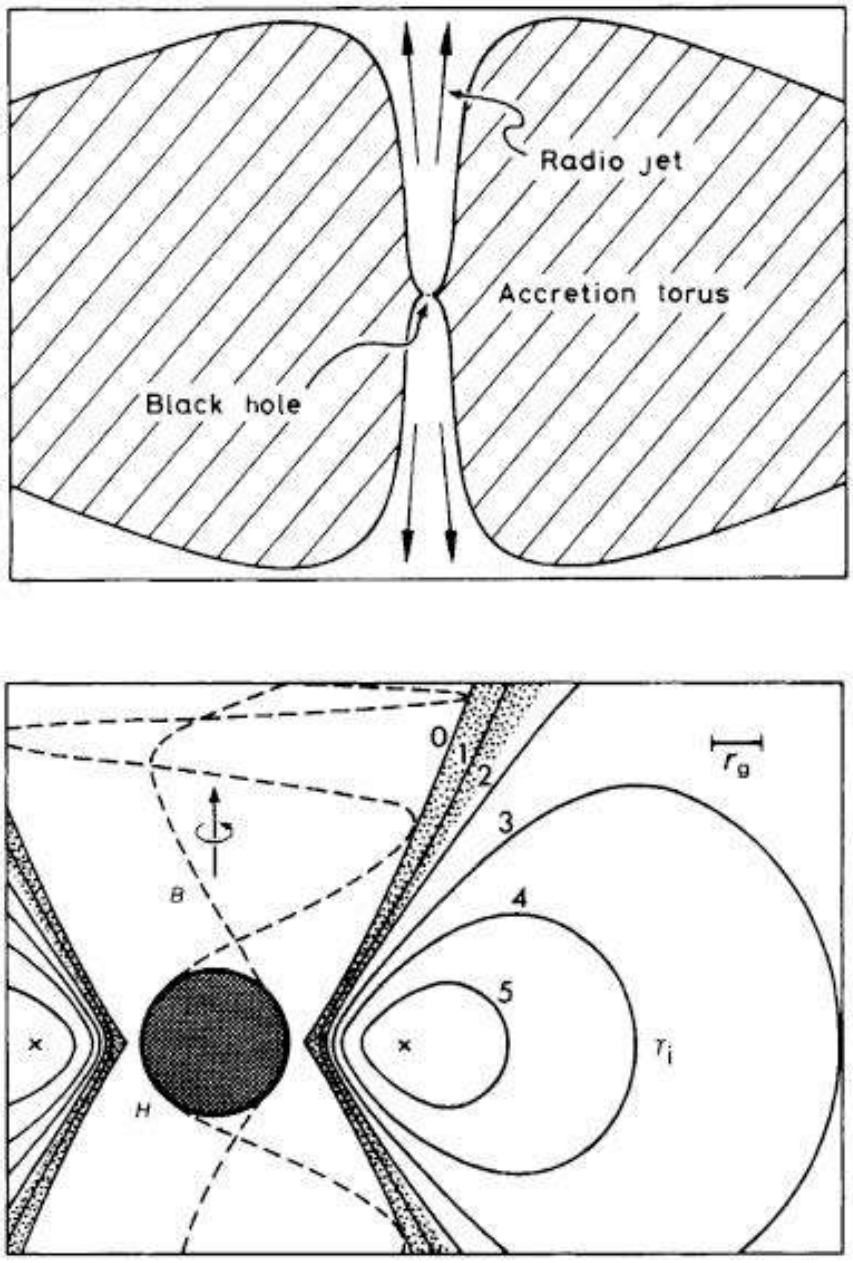

Figure 1.3: Scheme of the geometrical structure (top) and contours of equal temperature (solid line, bottom) of the ions torus presented by Rees (Rees et al., 1982). $r_g = GM/c^2$, where M is the black hole mass. The dark circle on the left is the region with radius r_g around the black hole.

Chapter 2

Some useful concepts of fluid dynamics

In this chapter, we discuss briefly some concepts of fluid dynamics that are useful for this work. The reference books are Clarke and Carswell (2014), Shu (1992), Feynman (1964) and Fermi (1956).

2.1 Fluid dynamics equations

Concept of fluid

A system can be defined as fluid and ruled by the fluid dynamics equations, when it can be represented as an object composed of so-called fluid elements. The fluid element is assumed to be such that it satisfies specific properties. Let us consider that l is the size of the fluid element, so the quantity l^3 is its volume. The fluid element must be big enough to contain a large number of particles. If n is the number density of particles, this gives the condition

$$nl^3 \gg 1. \tag{2.1}$$

On the other hand, the fluid element is small enough that there is not any variation in the physical quantities that describe the system, like pressure, temperature, etc... Thus it is smaller than the scale length for change of any variable. Considering that q is a macroscopic variable of the system, the scale length over which q varies by order of unity is

$$L \equiv \frac{|q|}{\|\nabla q\|}. \tag{2.2}$$

So we have the condition

$$l \ll L. \tag{2.3}$$

Finally, there is a fundamental condition that distinguishes the fluids. A fluid is said collisional if the particles into the fluid element interact with each other. So,

considering λ the mean free path of the particles, the fluid is collisional if it holds the condition

$$l \gg \lambda. \tag{2.4}$$

Otherwise, the fluid is said collisionless. If a fluid is collisional we can describe it with an equation of state, that relates, in general, the density, the pressure, and the temperature of the system. However there are some particular conditions, where the system is not properly a fluid as we have defined it, but we can still use the fluid equations to describe it (see sec. 2.3).

System of fluid equations

The fluid physical properties are described by 4 equation system. Considering that ρ, P, and $\mathbf{v}$ are the density, the pressure, and the velocity fields of the system, and $\epsilon_{\rm tot}$ is the total energy per unit volume, and that, generally, any quantity q depends on the position $\mathbf{x} = (x, y, z)$ and time t, $q = q(x, y, z, t)$, the fluid equations are

$$\frac{\partial \rho}{\partial t} + \nabla \cdot (\rho \mathbf{v}) = 0, \tag{2.5}$$

$$\rho \frac{\partial \mathbf{v}}{\partial t} + \rho(\mathbf{v} \cdot \nabla)\mathbf{v} + \nabla P = 0, \tag{2.6}$$

$$\frac{\partial \epsilon_{\rm tot}}{\partial t} + \nabla \cdot \left[(\epsilon_{\rm tot} + P)\mathbf{v}\right] = 0. \tag{2.7}$$

The equations are known as mass, Euler or momentum, and energy equation, respectively. They are written in the conservative form, and imply mass, momentum, and energy conservation. On the right-hand side, the source/sink terms can be added. An important term in astrophysics is the gravitational potential which enters both the Euler and the energy equation. We will discuss it in section 2.1. Other additional source terms can be net radiative cooling and heat thermal conduction, which enter the energy equation.

Given the gravitational potential, and the source/sink terms, the gas motion can be solved numerically by considering also an equation of state. In this case, there are six variables (ρ, P, $\mathbf{v}, \epsilon_{\rm tot}$) and six equations. However, in some special cases, the equations can be simplified, and the solutions can be found analytically.

Gravitational potential and self-gravitating systems

With the presence of the gravitational potential $\Phi_{\rm tot}$, the Euler equation is

$$\rho \frac{\partial \mathbf{v}}{\partial t} + \rho(\mathbf{v} \cdot \nabla)\mathbf{v} = -\nabla P - \rho \nabla \Phi_{\rm tot}. \tag{2.8}$$

The gravitational potential might be due to the fluid itself, or due to other external components, or it can be the sum of both. The choice is made by the problem

we want to study. For example, if we consider a gas cloud in a galaxy and we want to study its motion under the galaxy gravitational potential, we have to use the latter. It can be the sum of the stars, the dark matter, and the interstellar medium gravitational potentials. We can neglect one or more of these components, depending on the context. If we neglect the gravitational field of the cloud itself, the gravitational potential is said to be external.

On other hand, if we want to study, e.g. the equilibrium or the compression/expansion of the cloud, we can consider only its gravitational potential, which is dominant in this issue. In this case, we are considering the self-gravity of the system without external contributions. Obviously, we can consider both the external and the fluid gravitational fields if they are comparable. Summarizing, the gravitational potential $\Phi_{\rm tot}$, that appears in the fluid equations system, can be

$$\begin{aligned}\Phi_{\rm tot} &= \Phi,\\ \Phi_{\rm tot} &= \Phi_{\rm ext},\\ \Phi_{\rm tot} &= \Phi + \Phi_{\rm ext},\end{aligned}$$

where Φ is the gravitation potential of the gas, and $\Phi_{\rm ext}$ is the sum of all the external contributions we want to consider.

In the self-gravitating case, we can relate the density distribution and the gravitational potential through Poisson's equation

$$\nabla^2\Phi = 4\pi G\rho, \tag{2.9}$$

where $G = 6.67 \times 10^{-8}$ cm^3 g^{-1} s^{-2} is the universal gravitation constant.

In this work, we are going to consider first the systems in equilibrium in their gravitational potential, then in the external gravitational potential of a black hole, and, finally, in the sum of the two contributions.

Energy equation

In this paragraph, we consider the energy equation for the different cases of gravitational potential.

The total energy per volume unit, $\epsilon_{\rm tot}$, of the gas is the sum of all the contributions to energy

$$\epsilon_{\rm tot} = \epsilon_{\rm kin} + \epsilon_{\rm th} + \epsilon_{\rm grav},$$

where $\epsilon_{\rm th}$ is the internal energy per unite volume of the system, i.e. disordered kinetic energy of the particles (we will see in in sec. 2.2 its expression for ideal gases), $\epsilon_{\rm kin} = \rho v^2/2$ is the macroscopic ordered kinetic energy, where $v = |\mathbf{v}|$, and $\epsilon_{\rm grav}$ is the gravitational energy. The latter is different based on the gravitational forces we are considering. If the gravitational potential is external, so $\epsilon_{\rm grav} = \rho\Phi_{\rm ext}$, the energy equation is

$$\frac{\partial\epsilon_{\rm tot}}{\partial t} + \nabla\cdot\left[(\epsilon_{\rm tot} + P)\mathbf{v}\right] = \rho\frac{\partial\Phi_{\rm ext}}{\partial t}. \tag{2.10}$$

In the self-gravitating case, $\epsilon_{\rm grav} = \frac{1}{2}\rho\Phi$, the energy equation is

$$\frac{\partial \epsilon_{\rm tot}}{\partial t} + \nabla \cdot \left[(\epsilon_{\rm tot} + P + \frac{1}{2}\rho\Phi)\mathbf{v}\right] = -\nabla \cdot \left[\frac{1}{8\pi G}\left(\Phi\frac{\partial \nabla\Phi}{\partial t} - \nabla\Phi\frac{\partial \Phi}{\partial t}\right)\right]. \quad (2.11)$$

Finally, considering the sum of all contributions, $\epsilon_{\rm grav} = \rho\Phi_{\rm ext} + \frac{1}{2}\rho\Phi$, we get

$$\frac{\partial \epsilon_{\rm tot}}{\partial t} + \nabla \cdot \left[(\epsilon_{\rm tot} + P + \frac{1}{2}\rho\Phi)\mathbf{v}\right] = -\nabla \cdot \left[\frac{1}{8\pi G}\left(\Phi\frac{\partial \nabla\Phi}{\partial t} - \nabla\Phi\frac{\partial \Phi}{\partial t}\right)\right] + \rho\frac{\partial \Phi_{\rm ext}}{\partial t}. \quad (2.12)$$

2.2 Ideal gas

In this work, when necessary we will assume that the fluid is an ideal gas. In this section we describe the main physical properties that hold for this type of gas.

Equation of state

An equation of state is, in general, an expression that correlates the pressure with the density and the temperature of the system, which can be written as $P = P(\rho, T)$. An equation of state is said barotropic if the pressure depends only on the density $P = P(\rho)$. The ideal gas equation of state is

$$P = \frac{k_{\rm B}T}{\mu m_{\rm p}}\rho, \quad (2.13)$$

where $k_{\rm B} = 1.38 \times 10^{-16}$ erg K^{-1} is the Boltzmann's constant, $m_{\rm p} = 1.6 \times 10^{-24}$ g is the proton mass, and μ is the mean molecular (or atomic) weight.

Adiabatic index

The adiabatic index γ is the ratio of the specific heats at constant pressure c_P and at constant volume c_V,

$$\gamma \equiv \frac{c_P}{c_V}, \quad (2.14)$$

which are defined as follows:

$$c_P \equiv \left(\frac{\partial Q}{\partial T}\right)_P = T\left(\frac{\partial s}{\partial T}\right)_P \quad (2.15)$$

and

$$c_V \equiv \left(\frac{\partial Q}{\partial T}\right)_V = T\left(\frac{\partial s}{\partial T}\right)_V, \quad (2.16)$$

where δQ is the heat transfer per unit mass, and $ds = \delta Q/T$ is the specific entropy. For an ideal gas, the adiabatic index γ is

$$\gamma = \frac{5+q}{3+q}, \quad (2.17)$$

where q is the number of internal degree of freedom. For a monoatomic gas $q = 0$, thus $\gamma = 5/3$. For a biatomic gas $q = 2$, considering the molecule rotation, thus $\gamma = 7/2$. Therefore in this work, we consider especially these two values of γ: the monoatomic adiabatic index $\gamma = 5/3$ when we consider, for example, the application of the models to the ionized thick accretion discs around the black hole, since it holds also for plasma, and the biatomic adiabatic index $\gamma = 7/5$ when we consider the molecular hydrogen tori that obscure the central parts of the AGN.

Entropy and energy

The internal energy per unit mass for an ideal gas is

$$e = \frac{2+q}{3}\frac{k_{\rm B}T}{\mu m_{\rm p}}, \tag{2.18}$$

it can be rewritten, in terms of the adiabatic index γ, as

$$e = \frac{1}{\gamma-1}\frac{k_{\rm B}T}{\mu m_{\rm p}}. \tag{2.19}$$

Thus, using the equation of state, the internal energy per unit volume is

$$\epsilon = \rho e = \frac{P}{\gamma-1}. \tag{2.20}$$

Therefore the total energy per unit volume of an ideal gas in the presence of the self-gravitating potential Φ, the external potential $\Phi_{\rm ext}$, the sum of self-gravitating and external potential $\Phi_{\rm tot} = \Phi + \Phi_{\rm ext}$ are, respectively,

$$\epsilon_{\rm tot} = \frac{\rho v^2}{2} + \frac{P}{\gamma-1} + \frac{1}{2}\rho\Phi, \tag{2.21}$$

$$\epsilon_{\rm tot} = \frac{\rho v^2}{2} + \frac{P}{\gamma-1} + \rho\Phi_{\rm ext}, \tag{2.22}$$

and

$$\epsilon_{\rm tot} = \frac{\rho v^2}{2} + \frac{P}{\gamma-1} + \frac{1}{2}\rho\Phi + \rho\Phi_{\rm ext}. \tag{2.23}$$

The specific entropy for an ideal gas is

$$s = \frac{1}{\gamma-1}\frac{k_{\rm B}}{\mu m_{\rm p}}\ln\left(\frac{P}{\rho^\gamma}\right) + const. \tag{2.24}$$

Because we are interested only in relative variation of s, in this work we can consider a normalized entropy defined as

$$\sigma \equiv \ln\left(\frac{P}{\rho^\gamma}\right). \tag{2.25}$$

The normalized entropy is the physical quantity that appear in the Solberg-Høiland criterion (sec. 2.4) and in the stability criteria in the presence of a weak magnetic field (sec. 2.5). When we compute the entropy for our systems, we will include the constants that multiply the pressure and the density in the additive constant of the entropy.

2.3 Stationary axisymmetric rotating fluids

In this section, we define and describe the physical properties of rotating axisymmetric stationary fluids, in equilibrium in the gravitational potential. To study the problem we use the cylindrical coordinates R, ϕ, z. A fluid is stationary when the time partial derivatives of all the physical quantities q that describe the system are null ($\partial q/\partial t = 0$). The fluid does not have to be necessarily at rest, the velocity can be not null but it does not to be time dependent. The assumption of axisymmetry implies that all the partial derivatives with respect the azimuthal angle are null ($\partial q/\partial \phi = 0$). Thus all the physical properties are functions of R and z ($q = q(R, z)$). Consider an axisymmetric stationary rotating fluid with $v_R = v_z = 0$, and $v_\phi \neq 0$. The mass, the energy, and the azimuthal component of Euler equations are satisfied. The radial and vertical components of Euler equation are

$$\frac{1}{\rho}\frac{\partial P}{\partial R} = -\frac{\partial \Phi_{\rm tot}}{\partial R} + \Omega^2 R \tag{2.26}$$

and

$$\frac{1}{\rho}\frac{\partial P}{\partial z} = -\frac{\partial \Phi_{\rm tot}}{\partial z}, \tag{2.27}$$

where $\Omega = v_\phi/R$ is the angular velocity. Given the density distribution ρ of the fluid and the gravitational potential $\Phi_{\rm tot}$, in which the fluid is in equilibrium, the system of equations 2.26-2.27 can be solved analytically.

2.3.1 Poincaré-Wavre theorem

We present here an important result that describes the differences between the rotating fluids that have a cylindrical angular velocity, from the more general ones, which have an angular velocity with a vertical gradient. This depends on how the pressure is distributed with respect the density and the temperature of the system. In particular, the barotropic distributions[1], where the pressure is stratified on the density $P = P(\rho)$, have an angular velocity that depends only on R: $\Omega = \Omega(R)$. The baroclinic distributions, where the pressure is not stratified on the density

[1]We note that a barotropic distribution does not imply a barotropic equation of state. The former is a spatial property of a stationary configuration, the latter a general property of the gas.

and depends on the density and the temperature $P = P(\rho, T)$, have an angular velocity that depends on both R and z: $\Omega = \Omega(R, z)$. This is established by the Poincaré-Wavre theorem, which we prove here below.

Introducing the quantity $\mathbf{g} = (g_R, g_\phi, g_z)$ defined like

$$g_R \equiv \frac{v_\phi^2}{R} - \frac{\partial \Phi_{\text{tot}}}{\partial R}, \tag{2.28}$$

$$g_\phi \equiv 0, \tag{2.29}$$

$$g_z \equiv -\frac{\partial \Phi_{\text{tot}}}{\partial z}. \tag{2.30}$$

The R and z components of Euler equation can be written as

$$\frac{1}{\rho}\nabla P = \mathbf{g}. \tag{2.31}$$

In particular conditions, the quantity $\mathbf{g}$ can be expressed like the gradient of a scalar Φ_{eff}, called the effective potential. If $\mathbf{g} = -\nabla\Phi_{\text{eff}}$, it follows that

$$g_R = \frac{\partial \Phi_{\text{eff}}}{\partial R}, \tag{2.32}$$

$$g_z = \frac{\partial \Phi_{\text{eff}}}{\partial z}, \tag{2.33}$$

and this implies that

$$\frac{\partial g_R}{\partial z} = -\frac{\partial^2 \Phi_{\text{eff}}}{\partial z \partial R} = -\frac{\partial^2 \Phi_{\text{eff}}}{\partial R \partial z} = \frac{\partial g_z}{\partial R}. \tag{2.34}$$

The equation 2.34 is the condition to define an effective gravitational potential. Computing the terms of equations 2.34 we find

$$\frac{\partial g_z}{\partial R} = \frac{2v_\phi}{R}\frac{\partial v_\phi}{\partial z} - \frac{\partial^2 \Phi_{\text{eff}}}{\partial R \partial z} \tag{2.35}$$

and

$$\frac{\partial g_R}{\partial z} = -\frac{\partial^2 \Phi_{\text{eff}}}{\partial z \partial R}. \tag{2.36}$$

These two terms are equal only if $\partial v_\phi/\partial z = 0$, or equivalently $\partial\Omega/\partial z = 0$. Thus we can define an effective potential, for which holds the condition

$$\frac{1}{\rho}\nabla P = -\nabla \Phi_{\text{eff}}, \tag{2.37}$$

if and only if the angular velocity depends only on the radial coordinate $\Omega = \Omega(R)$. From $\nabla P/\rho = -\nabla\Phi_{\text{eff}}$ it follows that the pressure is stratified on the effective potential $P = P(\Phi_{\text{eff}})$. Considering the curl of eq. 2.37, we obtain

$$\nabla \times (\nabla P) = -\nabla \times (\rho \nabla \Phi_{\text{eff}}) = -\rho \nabla \times (\nabla \Phi_{\text{eff}}) - \nabla\rho \times \nabla\Phi_{\text{eff}}.$$

Since $\nabla \times (\nabla P) = \nabla \times (\nabla \Phi_{\rm eff}) = 0$, it follows

$$\nabla \rho \times \nabla \Phi_{\rm eff} = 0,$$

thus also the density is stratified on the effective potential, so the pressure is stratified like the density $P = P(\rho)$, i.e. the system is barotropic.

Considering now the vorticity equation (Clarke and Carswell, 2014; Balbus, 2017)

$$R\frac{\partial \Omega^2}{\partial z} = \frac{1}{\rho}\left(\frac{\partial P}{\partial z}\frac{\partial \rho}{\partial R} - \frac{\partial P}{\partial R}\frac{\partial \rho}{\partial z}\right). \tag{2.38}$$

If the system is barotropic $P = P(\rho)$ it follows that

$$\frac{\partial P}{\partial R} = \frac{{\rm d}P}{{\rm d}\rho}\frac{\partial \rho}{\partial R} \tag{2.39}$$

and

$$\frac{\partial P}{\partial z} = \frac{{\rm d}P}{{\rm d}\rho}\frac{\partial \rho}{\partial z}. \tag{2.40}$$

The term in the parenthesis of eq. 2.38 gets null and $\partial \Omega^2/\partial z = 0$, thus $\Omega = \Omega(R)$. So we have proved the Poincaré-Wavre theorem: an effective gravitational potential $\Phi_{\rm eff}$ exists if and only if the angular velocity depends only on R ($\Omega = \Omega(R)$), which implies that the pressure is barotropic $P = P(\rho)$ and vice-versa, if the system is barotropic, this implies necessarily that the angular velocity depends only on R, i.e. the isorotation surfaces are stratified on cylinders. Otherwise if the system is baroclinic $P = P(\rho, T)$, the angular velocity depends also on z $\Omega = \Omega(R, z)$. In this work we study baroclinic systems, thus we cannot define an effective potential $\Phi_{\rm eff}$.

2.3.2 Pressure support

In the beginning of this chapter, we illustrated the conditions that strictly define a fluid system. However, in some particular conditions we can apply the fluid dynamics equations also for systems that are not strictly speaking fluids. This holds for the rotating systems in equilibrium, also when they are not composed by fluid elements. In equations 2.26 and 2.27 we can consider other types of pressure support.

When in a system composed of ideal gas in equilibrium, the pressure support is thermal, the fluid is ruled by the equation of state $P_{\rm th} = k_{\rm B}T\rho/\mu m_{\rm p}$, but, for example, a gaseous system can have the addition of a pressure support due to the turbulent motion of the gas $P_{\rm turb}$. If the turbulent velocity dispersion of the gas $\sigma_{\rm turb}$ is isotropic, the total gas pressure is $P = P_{\rm th} + P_{\rm turb}$, where $P_{\rm turb} = \rho\sigma^2_{\rm turb}$. We can define $\sigma^2_{\rm g} = (\sigma^2_{\rm turb} + \sigma^2_{\rm th})$, where $\sigma^2_{\rm th} = k_{\rm B}T/\mu m_{\rm p}$, thus $P = \rho\sigma^2_{\rm g}$.

The considerations above can apply also to a discrete system composed of small or point objects with an isotropic velocity dispersion, in this case the pressure support is given by the random motion of the objects that compose the system.

The power-law tori models that we are going to study can be considered like gaseous systems where the thermal pressure is dominant with respect to the turbulent pressure, thus the temperature is given by the equation of state (eq. 2.13) and the internal energy by eq. 2.18. For the application of the models to the molecular tori of AGN, for simplicity, considered composed of a continuous fluid of only molecular hydrogen, the biatomic adiabatic index $\gamma = 7/5$ has to be used, whereas for accretion discs plasma, the monoatomic adiabatic index $\gamma = 5/3$ has to be used. The molecular tori can be interpreted as dominated by turbulence, thus the pressure is $P = P\sigma^2_{\rm turb}$. This is the case of the molecular tori observed by Combes et al. (2019), where the temperature of the gas is low and the velocity dispersion is high (see fig. 1.1.)

The other possible interpretation is considering the AGN molecular tori as discrete systems composed of molecular gas clouds. In this case, the pressure support is given by the velocity dispersion, assumed isotropic, of the random motion of the small clouds that compose the tori. If σ_c is the velocity dispersion, the pressure is $P = \rho_c \sigma_c^2$, where ρ_c is the density of the clouds, for example in solar masses per parsec cubed. The clouds themselves have their own gas density and their thermal pressure support. Unfortunately, in the latter cases, we can not define the energy and the entropy of the systems through the adiabatic index γ, this means that the stability criteria that involve entropy gradients cannot be used to evaluate the stability of the systems with these interpretations. The stability criteria hold only for fluids strictly defined.

2.4 Solberg-Høiland stability criterion

In this section, we describe the Solberg-Høiland stability criterion (Tassoul, 1978). In general, a stability criterion can check if a system in equilibrium is stable against particular perturbations. Applying the Solberg-Høiland criterion to a stationary rotating axisymmetric fluid system, we can know if this system is stable against linear axisymmetric perturbations. The criterion applies to both barotropic and baroclinic systems.

The fluid stability criteria, in general, are found perturbing the fluid equations of the unperturbed fluid system in equilibrium. The analysis can be made considering small, i.e. linear, perturbations with $|\delta q/q| \ll 1$, where q is a generic quantity of the fluid and δq is the perturbation of the quantity q. Since we consider only linear perturbations, once the systems of equations is perturbed, it can be linearised neglecting all the non-linear perturbed terms. We consider Eulerian perturbations that are defined as $\delta q \equiv q(\mathbf{x}, t) - q_0(\mathbf{x})$, where q_0 is the unperturbed quantity.

Using the Fourier theorem, the perturbation can be written as

$$\delta q(\mathbf{x}, t) = \frac{1}{(2\pi)^4} \int \hat{\delta q}(\mathbf{k}, w) e^{i(\mathbf{k}t - \omega t)} d^3\mathbf{k} d\omega, \tag{2.41}$$

where $\mathbf{k}$ is the wave vector, ω is the wave angular frequency, and $\hat{dq}$ is a coefficient that depends on the wave properties $\mathbf{k}$ and ω. In practice, a generic perturbation can be decomposed in Fourier components. Thus, using the superposition principle, i.e. the fact that a linear combination of solutions is also a solution, we can study the behaviour of all possible perturbations by studying only a single Fourier mode

$$\delta q = \hat{\delta q} e^{i(\mathbf{k}\mathbf{x} - \omega t)}. \tag{2.42}$$

The wave vector and angular frequency are related by the linearised equations: solving this equations system it is possible to find the dispersion relation $\omega = \omega(\mathbf{k})$. Thus assuming real $\mathbf{k}$, the behaviour of the perturbation is given by the imaginary part $\Im(\omega)$ of ω. Let us consider a dispersion relation that depends on ω only through ω^2, as it is the case for the Solberg-Høiland analysis. If $\omega^2 > 0$, i.e. ω is real and $\Im(\omega) = 0$, the perturbation oscillates and the system are stable to these perturbations. Otherwise if $\omega^2 < 0$, there are two solutions, one with $\Im(\omega) < 0$,and the other with $\Im(\omega) > 0$. The former describes a perturbation that decays with the time, which is stable, the latter describes a perturbation that grows exponentially with time, i.e. that drives the system toward instability. Thus the conditions to verify the stability of a systems is derived by the study of the dispersion relation. If $\omega^2 > 0$ for all the types of perturbations, i.e. for all the possible wavevectors $\mathbf{k}$ of the perturbations considered, the system is stable.

We consider now axisymmetric stationary rotating fluids, which have pressure, entropy and angular momentum gradients. The stability criterion that we are going to show, i.e. the Solberg-Høiland stability criterion, can be seen as a generalization of the Rayleigh rotational stability and the Schwarzschild convective stability criteria. We recall briefly, that in a static system in which the pressure decreases outward, the Schwarzschild criterion imposes that the entropy has to increase outward for the stability to convective motions. The Rayleigh criterion for rotating discs imposes that the squared angular momentum has to increase outward for stability. For barotropic systems, the Solberg-Høiland criterion reduces to a combination of the convective and the rotational criteria. For baroclinic systems, studied in this work, the Solberg-Høiland criterion involves the presence of the pressure, entropy and angular momentum gradients mixed.

To find the Solberg-Høiland criterion, a baroclinic axisymmetric fluid in equilibrium is perturbed with a linear axisymmetric perturbation with a wavevector $\mathbf{k} = (k_R, 0, k_z)$, in the form

$$\delta q = \hat{\delta q} e^{i(k_R R + k_z z - \omega t)}. \tag{2.43}$$

The dispersion relation obtained from the perturbed linearised system of fluid dynamical equations is

$$\omega^2 = -\frac{1}{R^3}\left(x\frac{\partial\Omega^2R^4}{\partial R} - \frac{\partial\Omega^2R^4}{\partial z}\right) - \frac{1}{\gamma\rho}\left(x\frac{\partial P}{\partial z} - \frac{\partial P}{\partial R}\right)\left(x\frac{\partial\sigma}{\partial z} - \frac{\partial\sigma}{\partial R}\right), \quad (2.44)$$

where $x \equiv k_R/k_z$. We note that, in the right-hand side of this equation, the first term involves the squared angular momentum gradient, thus the rotation of the fluid (as it occur in the Rayleigh stability criterion), whereas the second term involves the entropy and the pressure gradients, quantities that appear in the Schwarzschild convective criterion. The squared angular frequency must be positive for stability, so we obtain the condition

$$\frac{1}{\gamma\rho}\frac{\partial P}{\partial z}\frac{\partial\sigma}{\partial z}x^2 + \left(\frac{1}{R^3}\frac{\partial\Omega^2R^4}{\partial z} - \frac{1}{\gamma\rho}\left[\frac{\partial P}{\partial R}\frac{\partial\sigma}{\partial z} - \frac{\partial P}{\partial z}\frac{\partial\sigma}{\partial R}\right]\right)x + \frac{1}{\gamma\rho}\frac{\partial P}{\partial R}\frac{\partial\sigma}{\partial R} - \frac{1}{R^3}\frac{\partial\Omega^2R^4}{\partial R} < 0. \quad (2.45)$$

This condition has to be satisfied for every possible perturbation mode, thus for every value of k_R and k_z. The equation 6.7 for stability is verified for every x, if the following conditions are both satisfied:

$$\frac{1}{\gamma\rho}\left(\frac{\partial P}{\partial R}\frac{\partial\sigma}{\partial R} + \frac{\partial P}{\partial z}\frac{\partial\sigma}{\partial z}\right) - \frac{1}{R^3}\frac{\partial\Omega^2R^4}{\partial R} < 0 \quad (2.46)$$

and

$$\frac{\partial P}{\partial z}\left[\frac{\partial\Omega^2R^4}{\partial R}\frac{\partial\sigma}{\partial z} - \frac{\partial\Omega^2R^4}{\partial z}\frac{\partial\sigma}{\partial R}\right] < 0. \quad (2.47)$$

Equations 6.1 and 6.2 are the Solberg-Høiland stability criterion. We will use them to evaluate the stability of the gaseous power-law tori in chapter 6. We recall that this criterion holds only for linear axisymmetric perturbations. The behaviour of the system against non-linear or non-axisymmetric perturbations has to be studied with other tools.

2.5 Stability of rotating, weakly magntized fluids

In this work we present dynamical models with toroidal geometry that could be applied also for the thick accretion discs around the black holes or neutron stars, as those described in sec. 1.2. The accretion discs around the black holes or neutron stars are very hot, thus the gas in them is totally ionized (see sec. 1.2), and is expected to be magnetized. In this section we show the main physical characteristics of a plasma, focusing in plasma permeated by a weak magnetic field, and describe how the stability criteria are modified by the presence of the weak magnetic field.

The Lorentz force in a plasma, since the electric field is negligible, is

$$\mathbf{f}_{\mathrm{L}} = \frac{1}{4\pi}(\mathbf{B}\cdot\nabla)\mathbf{B} - \frac{1}{8\pi}\nabla B^2 \tag{2.48}$$

where $\mathbf{B}$ is the magnetic field and $B = |\mathbf{B}|$. The first term is the magnetic tension, a force which tends to align the magnetic field lines, whereas the second term is the gradient of the magnetic pressure $B^2/(8\pi)$, a force which is against the compression of the magnetic field. In the Euler equation that describes a plasma, the pressure gradient is substituted by the gradient of the sum of the thermal pressure and the magnetic pressure $\nabla P \to \nabla(P + B^2/8\pi)$. We can define two types of magnetized fluids, based on the strength of the magnetic field, with the β parameter

$$\beta \equiv \frac{P_{\mathrm{th}}}{P_{\mathrm{mag}}} = \frac{8\pi P}{B^2}. \tag{2.49}$$

In practice, the β parameter is the ratio between the thermal and the magnetic pressure in a magnetized fluid. If $\beta \gg 1$, the fluid has a dynamically unimportant magnetic field, otherwise, if $\beta \lesssim 1$, the fluid is permeated by a strong magnetic field and the contribution of the magnetic field is dynamically important. In this work, for simplicity, we consider only high β plasma, i.e. permeated by a weak magnetic field. The equilibrium in this type of plasma does not have contributions from the magnetic field, thus to find stationary solutions, the unmagnetized Euler equation can be used. The magnetic field, despite its weakness, is very important when we consider the stability of the systems. Indeed many rotating astrophysical systems in the presence of a weak magnetic field are unstable, and as we will see, the instability occurs also for the power-law tori studied in this work. Instead the presence of a strong magnetic field, could help the stability of the system as explained in Balbus and Hawley (1991).

We describe now the criteria for stability of a baroclinic stationary rotating axysimmetric fluid permeated by a weak magnetic field, for linear axysimmetric perturbations. We refer to Balbus (1995) for the derivation of the criterion. Perturbing the magneto-hydro-dynamics equations with a linear axisymmetric perturbation of the form 2.43, it is possible to obtain the dispersion relation, which in the limit of a weak magnetic field, is

$$\omega^2 = -R\left(x\frac{\partial\Omega^2}{\partial R} - \frac{\partial\Omega^2}{\partial z}\right) - \frac{3}{5\rho}\left(x\frac{\partial P}{\partial z} - \frac{\partial P}{\partial R}\right)\left(x\frac{\partial\sigma}{\partial z} - \frac{\partial\sigma}{\partial R}\right). \tag{2.50}$$

We note that the magnetic field does not appear in the dispersion relation, and thus in the stability condition, for weakly magnetized plasma. The limits for an unmagnetized fluid cannot be derived from eq. 7.1. To obtain the Solberg-Høiland criterion, the limit of a null magnetic field has to be considered in the perturbed fluid equations (see Balbus (1995) for a discussion). Imposing that $\omega^2 > 0$ for

stability, one obtains the conditions for generalized magneto rotational stability for stratified baroclinic rotating systems

$$\frac{3}{5\rho}\left(\frac{\partial P}{\partial R}\frac{\partial \sigma}{\partial R}+\frac{\partial P}{\partial z}\frac{\partial \sigma}{\partial z}\right)-R\frac{\partial \Omega^2}{\partial R}<0 \tag{2.51}$$

and

$$\frac{\partial P}{\partial z}\left[\frac{\partial \Omega^2}{\partial R}\frac{\partial \sigma}{\partial z}-\frac{\partial \Omega^2}{\partial z}\frac{\partial \sigma}{\partial R}\right]<0, \tag{2.52}$$

(for stability). We note that equations 7.2 and 7.3 differ from the Solberg-Høiland criterion (eqs. 6.1 and 6.2) only in the fact that the angular velocity takes the place of the angular momentum. We use eqs. 7.2 and 7.3 to study the stability of the power-law tori in chapter 7, under the assumption that they are a weakly magnetized plasma.

Chapter 3

Potential-density pairs of power-law tori

In this work, we analyze the families of toroidal fluid systems given by the axisymmetric density distribution (Ciotti and Bertin, 2005)

$$\rho = \rho_0 \frac{R^2}{r^\alpha}, \quad (\alpha > 2), \tag{3.1}$$

where $r = \sqrt{R^2 + z^2}$ is the spherical radial coordinate and R and z are the radial and vertical cylindrical coordinates. r, R, and z are in units of a, where a is a reference length, and are thus dimensionless. ρ_0 is a reference density such that $\rho(a, 0) = \rho_0$. The density distribution has the functional form of a power-law, where α is the power-law index.

The power-law density produces the following gravitational potential:

$$\Phi = -\Phi_0 \frac{r^{2-\alpha}}{(\alpha-2)(7-\alpha)} \left[\frac{4r^2}{(\alpha-4)(5-\alpha)} + R^2 \right] \quad (\alpha \neq 4), \tag{3.2}$$

$$\Phi = \frac{\Phi_0}{3} \left[2 \ln r - \frac{1}{2} \frac{R^2}{r^2} \right] \quad (\alpha = 4), \tag{3.3}$$

where $\Phi_0 = 4\pi G \rho_0 a^2$. Expliciting $r = \sqrt{R^2 + z^2}$, the equations 3.1, 3.2 and 3.3 are

$$\rho(R, z) = \rho_0 \frac{R^2}{(R^2 + z^2)^{\frac{\alpha}{2}}}, \quad (\alpha > 2) \quad , \tag{3.4}$$

$$\Phi(R, z) = -\Phi_0 \frac{(-\alpha^2 + 9\alpha - 16)R^2 + 4z^2}{(7-\alpha)(5-\alpha)(\alpha-4)(\alpha-2)(R^2+z^2)^{\frac{\alpha}{2}-1}} \quad (\alpha \neq 4), \tag{3.5}$$

$$\Phi(R, z) = \frac{\Phi_0}{3} \left[\ln(R^2 + z^2) - \frac{1}{2} \frac{R^2}{R^2 + z^2} \right] \quad (\alpha = 4). \tag{3.6}$$

However, it is useful to write the equations using the radial distance r where it explicitly appears. In addition to simplifying the equations, it allows us to look straightforwardly at the behavior of the physical quantities at large and small distances from the center.

We refer the reader to Ciotti and Bertin (2005) for the description of the construction of the potential-density pairs, which is based on homeidal expansion. Ciotti and Bertin (2005) show that the lower limit on α is $\alpha > 2$. We do not prove formally this result, but we note that for $\alpha = 2$, substituting $R = r\sin\theta$ in the density distribution, we obtain $\rho \propto \sin^2\theta$ and the toroidal structure does not exist anymore. The upper limit on the range of α is $\alpha < 5$. It is given by the constraint due to the divergence of the mass at the center, as we will see in sec. 3.1.

So we consider the power-law density (3.1) in the range $2 < \alpha < 5$. The geometry and the properties of the tori depend strongly on the value of α. In particular, as we will see, there are values of α for which the tori experiences changes of behavior in some of their properties. Two of these critical values of α are the only two integer values that α can hold, $\alpha = 3$ and $\alpha = 4$. In the following we will show the behavior of the tori with several values of α that are interesting in that context. The aim is to provide, at the end of the work, the characteristics of the models in every sub-range of α and their limit to a possible astrophysical application.

Before solving the fluid dynamics equations of the stationary models, in this chapter we make some preliminary considerations. In sec. 3.1, we compute the mass of the models, which, as we will see, is infinite; in sec. 3.2 and 3.3 we study graphically the differences of the tori density distribution and potential for different values of α. Then, we compute the circular velocity of the system (sec. 3.4) and, finally, the projected surface density of the systems when seen face-on and edge-on (sec. 3.5). In sec. 3.6, we present examples of power-law tori applications to the AGN molecular tori.

3.1 Mass integration

In this section we compute the mass of the tori. The density for $\alpha > 2$ at the limit $r \to \infty$ converges to zero, but the mass does not converges. Indeed, the power-law tori have infinite mass. For evaluating the integration it is convenient to switch to polar coordinates

$$\rho(R, z) \longrightarrow \rho(r, \theta)$$

. Considering $R = r\sin\theta$, one obtains

$$\rho(r, \theta) = \rho_0 \frac{\sin^2\theta}{r^{\alpha-2}}. \tag{3.7}$$

Thus the integration gives

$$M = \int_V \rho dV = a^3 \int_V \rho(r,\theta) \sin\theta r^2 d\phi d\theta dr$$

$$= 2\pi\rho_0 a^3 \int_0^\pi \sin^3\theta d\theta \int_0^\infty r^{4-\alpha} dr = \frac{8\pi}{3}\rho_0 a^3 \int_0^\infty r^{4-\alpha} dr. \tag{3.8}$$

For $\alpha < 5$ the mass always diverges at infinity. This problem can be avoided by considering a truncation radius. For $\alpha = 5$ the integral diverges also at the center,

$$\int_0^\infty \frac{1}{r} dr = \big[\ln r\big]_0^\infty.$$

The integral diverges at $r = 0$ also for larger values of α. Hence we consider only density distributions with $\alpha < 5$.

3.2 Isodensity curves and density profiles

The geometry of the torus depends on the value of α. Here, we show isodensity contours of the models for some values of α, to illustrate some differences among them. The choice of the values becomes clearer when we study other characteristics of the tori, although some peculiar characteristics also appear from the density distribution.

The density profiles in the equatorial plane for $\alpha = 2.1$, $\alpha = 3$, $\alpha = 4$ and $\alpha = 4.9$ and the corresponding isodensity contours in the meridional plane are plotted in fig. 3.1 and in fig. 3.2, respectively. The density profiles in the equatorial plane are power-law with slope $\alpha - 2$, so they are steeper for larger values of α. Looking at the contours of constant density we note that the torus with $\alpha = 4$ has isodensity curves that are circles, while for larger values of α the contours are elongated along the vertical direction. Instead, for lower values of α they are flattened, and elongated horizontally. The case with $\alpha = 2.1$ near the lower limit of the possible value of α ($\alpha > 2$) has isodensity contours very flattened horizontally.

Fig. 3.3 (top) shows the density profiles along the axis for $z = 1$. In these profiles it appears the torus structure: a central depression, where the density increases with R, then reaches a maximum, after which, it decreases. For all the four cases, the density in the equatorial plane increases roughly in the same way, it reaches the maximum near the scale length a and then decreases with different slopes for the four cases, flatter for lower values of α and steeper for the larger ones. The profile of the torus with $\alpha = 2.1$, near the lower limit of α, has a slope after the maximum nearly flat.

Along the z axis, i.e. for $R = 0$, the density vanishes. Too see the behavior of the density along z, we show the density profile along the z axis for $R = 1$ in fig.

3.1 (bottom). The density profiles along the z axis for $R = 1$ are nearly constant up to the reference scale and then decrease with different slopes for different values of α, steeper for larger α.

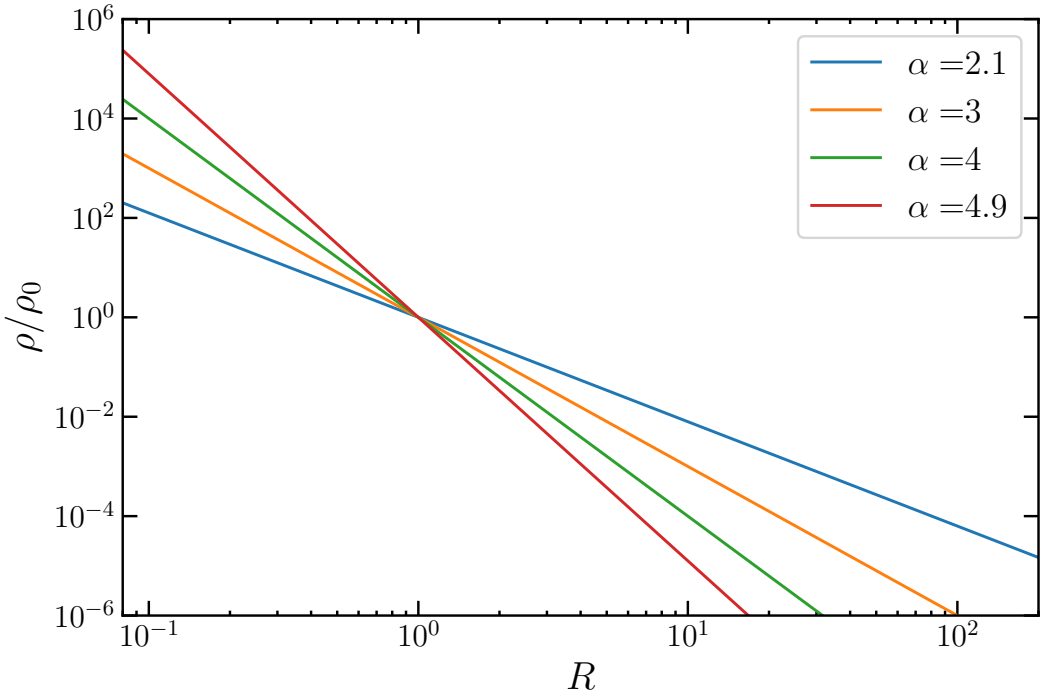

Figure 3.1: Density profiles in the equatorial plane for power-law tori with $\alpha = 2.1$, $\alpha = 3$, $\alpha = 4$ and $\alpha = 4.9$

3.3 Gravitational potential

In this section we analyze the characteristics of the gravitational potential of the power-law tori. First of all, we study the behavior of the potential at the limits, by considering the limit $r \to 0$ and $r \to \infty$. The expression of the potential for $\alpha \neq 4$ (eq. 3.2) can be rewritten as

$$\Phi(R, z) = -\Phi_0 \frac{(-\alpha^2 + 9\alpha - 16)R^2 + 4z^2}{(7-\alpha)(5-\alpha)(\alpha-4)(\alpha-2)r^{\alpha-2}} \qquad (\alpha \neq 4). \tag{3.9}$$

The numerator of eq. 3.9, $(-\alpha^2 + 9\alpha - 16)R^2 + 4z^2$, is proportional to r^2, so we obtain the asymptotic expression

$$\Phi \sim \frac{r^2}{r^{2-\alpha}} \sim \frac{1}{r^{\alpha-4}} \qquad (\alpha \neq 4). \tag{3.10}$$

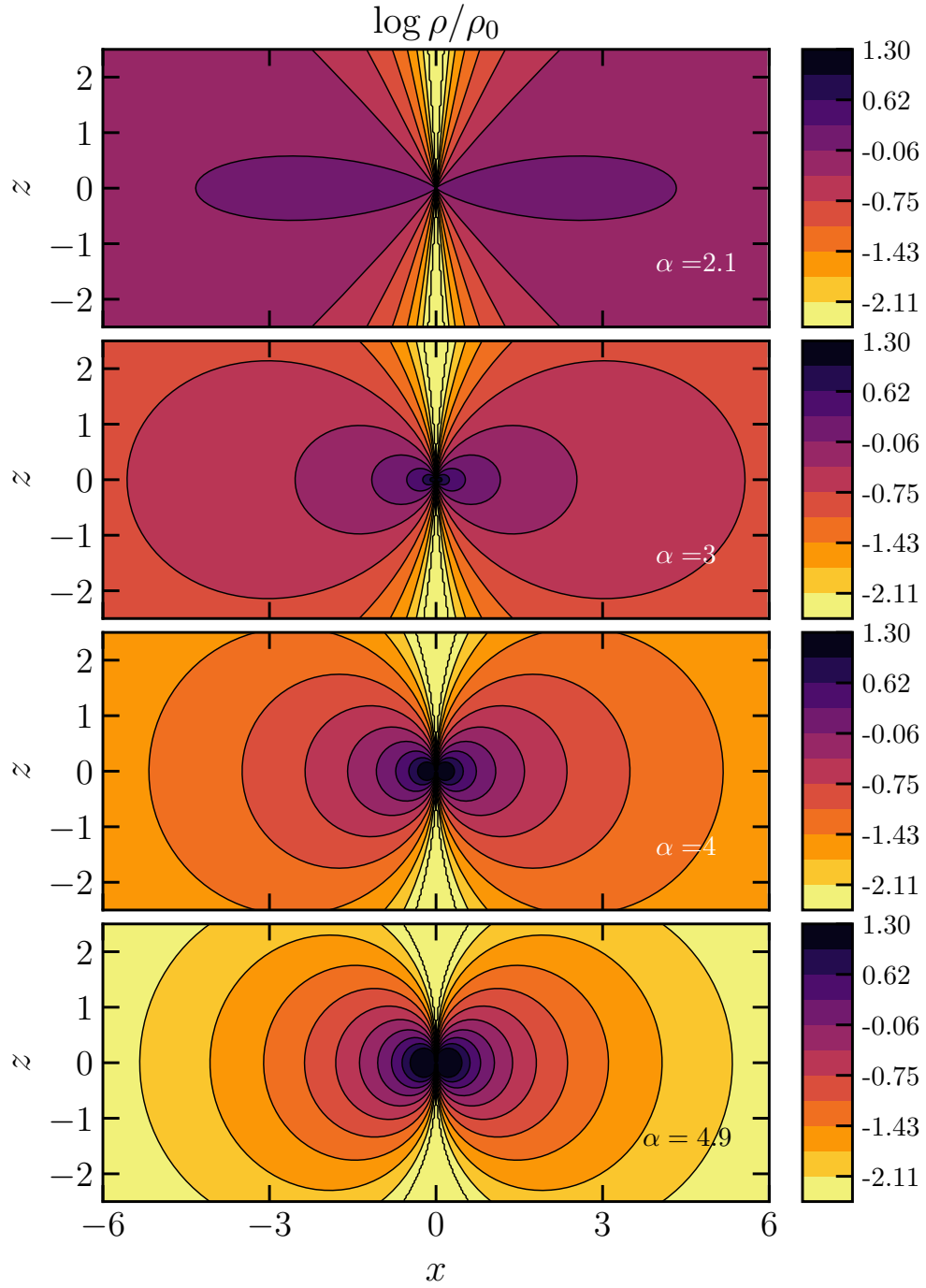

Figure 3.2: Isodensity contours in the meridional plane for power-law torus with $\alpha = 2.1$, $\alpha = 3$, $\alpha = 4$ and $\alpha = 4.9$ (from top to the bottom)

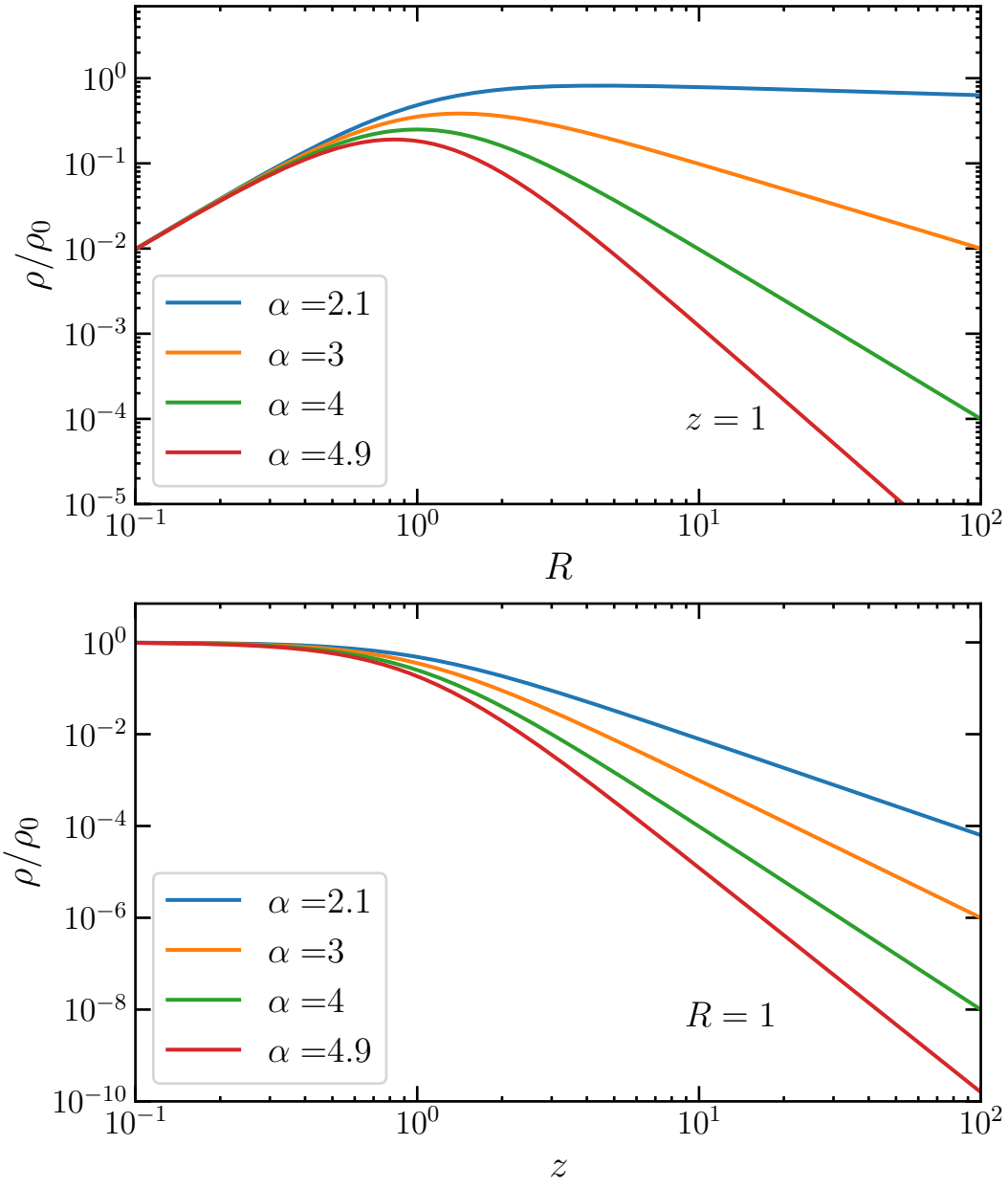

Figure 3.3: Density profiles of power-law tori with $\alpha = 2.1$, $\alpha = 3$, $\alpha = 4$ and $\alpha = 4.9$ as a function of R for $z = 1$ (top) and as a function of z for $R = 1$ (bottom).

In this way, we can compute easily the limits. In the range $4 < \alpha < 5$, for $r \to 0$ the potential diverges, instead, it vanishes for $r \to \infty$. In the range $2 < \alpha < 4$, the behavior is different, the potential vanishes at the origin and diverges at infinity. The potential for $\alpha = 4$ (eq. 3.3) behaves like the logarithm of the radial distance, because the second term in the parenthesis R^2/r^2 asymptotically is constant, thus

$$\Phi \sim \ln r \qquad (\alpha = 4).$$

Therefore the potential for $\alpha = 4$ diverges both at the origin and at infinity. The results are schematized below:

$$\begin{array}{ll} \Phi \to \infty & r \to 0 \\ \Phi \to 0 & r \to \infty \end{array} \qquad (4 < \alpha < 5),$$

$$\begin{array}{ll} \Phi \to -\infty & r \to 0 \\ \Phi \to \infty & r \to \infty \end{array} \qquad (\alpha = 4),$$

$$\begin{array}{ll} \Phi \to 0 & r \to 0 \\ \Phi \to \infty & r \to \infty \end{array} \qquad (2 < \alpha < 4).$$

We now analyze the coefficients of R and z in the equation 3.9. The coefficient of R^2 is $-\alpha^2 + 9\alpha - 16$. The equation $-\alpha^2 + 9\alpha - 16 = 0$ has roots: $\frac{9-\sqrt{17}}{2} \approx 2.44$ and $\frac{9+\sqrt{17}}{2} \approx 6.56$. Thus for $\alpha < 2.44$ and $\alpha > 6.56$ the coefficient of R^2 is negative. The values of α larger than 6.56 are not of interest because they are outer the range of α given by the mass. The sign of z^2 is always positive.

So for $\alpha \approx 2.44$, the isopotential contours change shape, in practice, in the equatorial plane the gravitational force pushes outwards for $\alpha < 2.44$. This topic is related to a change in the behaviour of the circular velocity in the equatorial plane, as we will see in sec. 3.4. The isopotential contours for $\alpha = 2.1$, $\alpha = 2.4$, and $\alpha = 2.5$ are plotted in fig. 3.4. We note the change in the shape between the latter two cases. The isopotential contours for $\alpha = 3$, $\alpha = 4$, and $\alpha = 4.9$ are plotted in fig 3.5. In general, comparing the isopotential (fig. 3.5) with the isodensity contours (fig. 3.2) for $\alpha > 2.44$, we note that the potential is more regular than the density distributions, in the sense that the contours are not toroidal. Looking at the two plot of the isopotential contours we note that, for $\alpha > 2.44$, for small values of α the contours are flattened along the equatorial plane, whereas for high values of α the contours are more spherical. This is due to the fact that the tori with higher values of α have more mass in the center, so the term of gravitational monopole, which produces a spherical potential like a point mass, is dominant at smaller distances from the center.

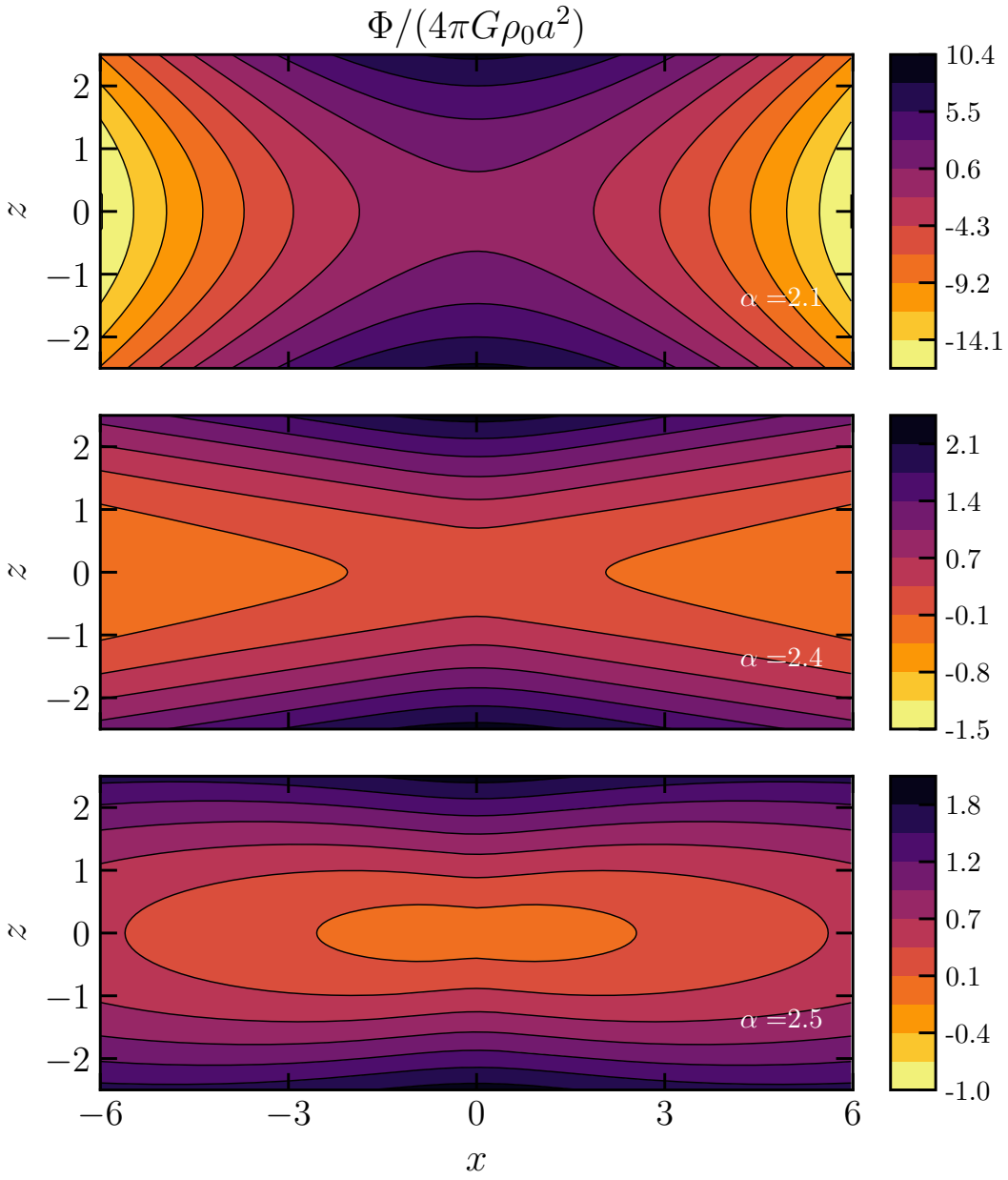

Figure 3.4: Isopotential contours in the meridional plane for power-law tori with $\alpha = 2.1$, $\alpha = 2.4$, and $\alpha = 2.5$ (from top to the bottom).

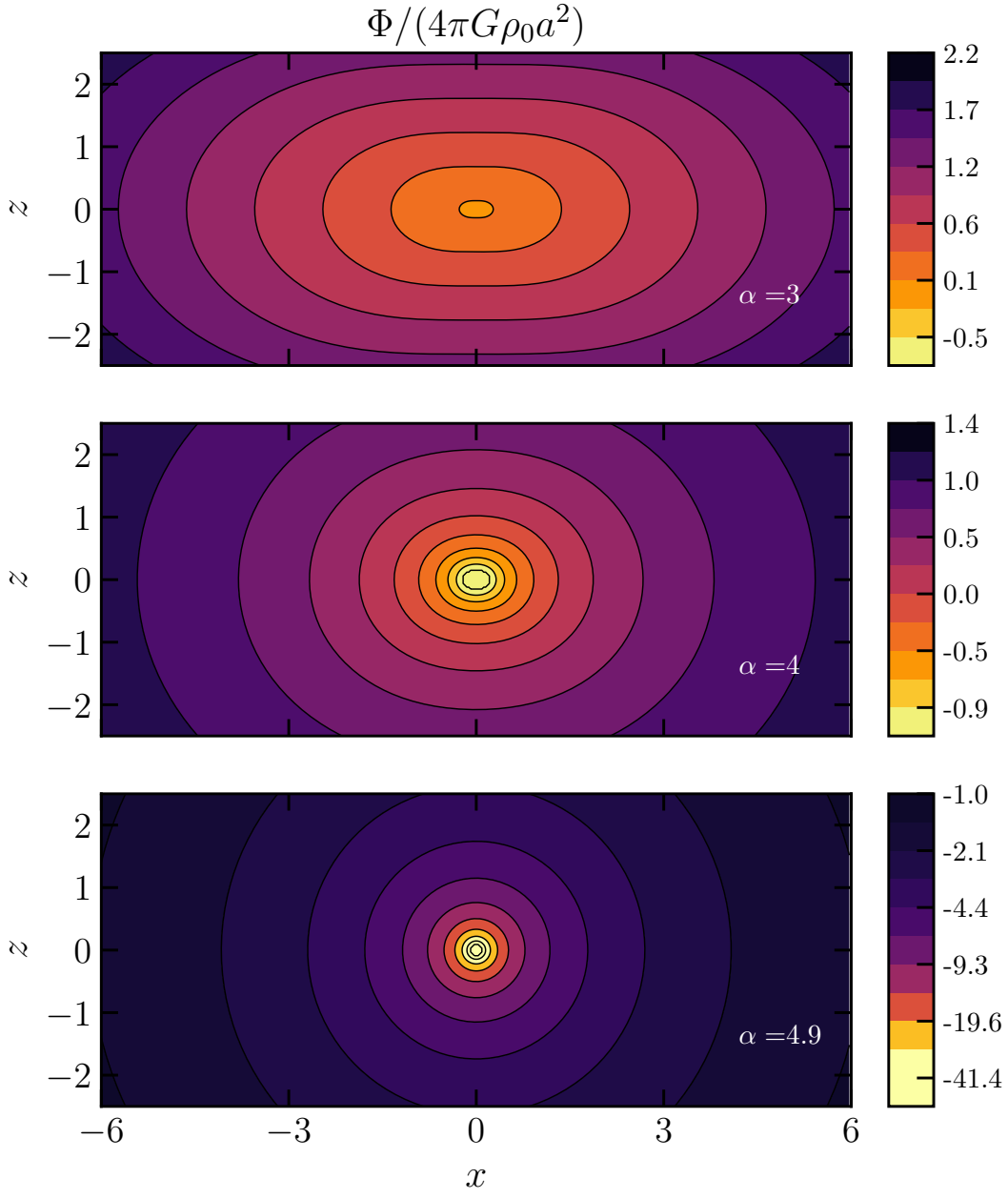

Figure 3.5: Isopotential contours in the meridional plane for power-law tori with $\alpha = 3$, $\alpha = 4$, and $\alpha = 4.9$ (from top to the bottom).

3.4 Circular velocity

Here we analyze the circular velocity in the equatorial plane of these systems. Considering the potential for $\alpha \neq 4$ (eq. 3.2), one gets

$$v_c^2 = R\frac{\partial \Phi}{\partial R}\bigg|_{z=0} = 4\pi G\rho_0 a^2 \frac{-\alpha^2+9\alpha-16}{(7-\alpha)(5-\alpha)(\alpha-2)} R^{4-\alpha}. \tag{3.11}$$

Instead, considering the potential for $\alpha = 4$ (eq. 3.3) the circular velocity is constant, with $v_c^2 = 2/3\Phi_0$. For $\alpha > 4$ the circular velocity decreases with R, whereas for $\alpha < 4$ the circular velocity increases with R. This is due, of course, by the mass distribution and the resulting potential. The tori with $\alpha > 4$ have more mass to the center, which it means that the radial force due to the inner mass distribution is dominant respect to that exerted from the outer parts. So the radial gravitational force increases approaching the center and an object in circular orbit in the equatorial plane has higher speed if it is at smaller radii.

The opposite happens for $\alpha < 4$, the mass is higher at large distances, thus the radial force exerted by the outer mass distribution is higher and an object placed in rotational equilibrium has higher speed if it is placed in the outer parts of the system. For even lower values of α, one expects that the mass in the outer parts is so high that the radial force is directed outwardly. Therefore no circular orbit exists and this means that the squared circular velocity value becomes negative. This happens for $\alpha \approx 2.44$, a characteristic value that we encountered when discussing the gravitational potential (sec. 3.3). Looking now at the isopotential contours of tori with $\alpha < 2.44$ in figure 3.4, wee note that in the equatorial plane the potential increases outwards and thus the resulting force is direct outwards.

The polynomial $-\alpha^2 + 9\alpha - 16$ that appears in the circular velocity equation (eq. 3.11) is the same that we analyzed in sec. 3.3 that determined the change of shape in Φ. Thus for $\alpha < 2.44$ the squared circular velocity is negative.

The circular velocity for $\alpha = 4.9$, $\alpha = 4.5$, $\alpha = 3$ and $\alpha = 2.5$ is plotted at the top and the middle of fig. 3.6. We note that for $\alpha > 4$ the circular velocity in the equatorial plane decreases with R and the decrease is stronger for larger values of α. For $\alpha < 4$ the circular velocity in the equatorial plane increases with R, and the increase is stronger for lower values of α. The radial derivative of the gravitational potential in the equatorial plane for $\alpha = 2.4$, $\alpha = 2.1$, plotted at the bottom of fig. (3.6), is everywhere negative. These negative values would correspond to negative v_c^2, however this does not mean that it is impossible to find a physical solution to Euler's equation (see chapter 4).

We conclude this section noting that the flat rotation curve in the equatorial plane is a characteristic that the power-law torus with $\alpha = 4$ shares with the Mestel disc (Mestel, 1963). In the next section we will see another analogy between these objects.

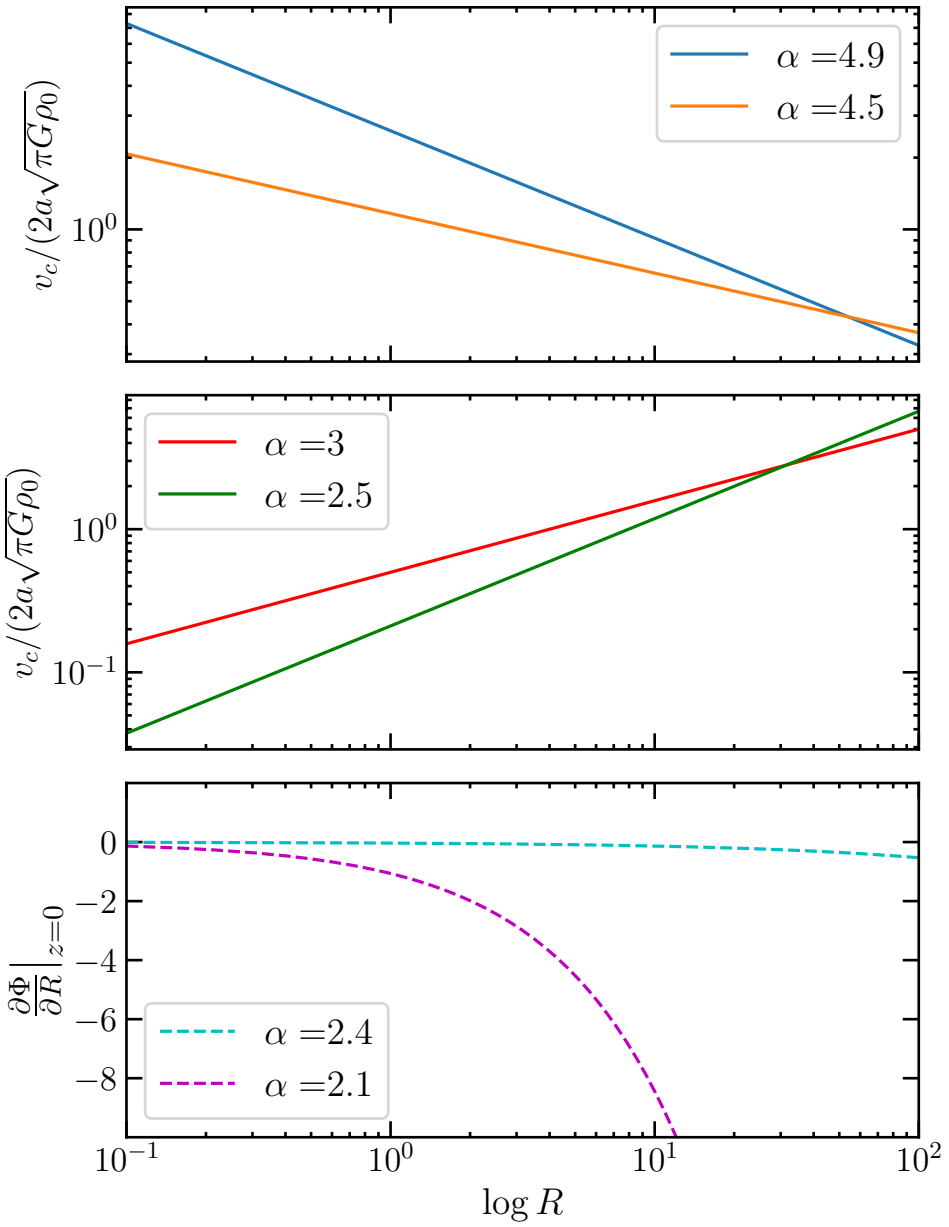

Figure 3.6: Top and center: circular velocity in the equatorial plane for power-law tori with $\alpha = 4.9$, $\alpha = 4.5$, $\alpha = 3$ and $\alpha = 2.5$. Bottom: radial derivative of gravitational potential in the equatorial plane computed for $\alpha = 2.4$ and $\alpha = 2.1$.

3.5 Surface density distributions

Here we compute the surface density distributions of the tori, assuming for simplicity that the system is seen either face-on or edge-on. The face-on surface density is

$$\Sigma(R) = 2a \int_0^\infty \rho(R,z)dz, \tag{3.12}$$

while the edge-on surface density is

$$\Sigma(R,z) = 2a \int_R^\infty \rho(R',z)\frac{R'dR'}{\sqrt{R'^2 - R^2}}. \tag{3.13}$$

We recall that all the distances are normalized to a, it means that the differential dz has to be dz/a, so we have an a out of the integral. Before solving these integrals, we prove a general result that will be useful in the following. For any A positive and $\delta > \frac{1}{2}$:

$$\int_0^\infty (A + x^2)^{-\delta} dx = \frac{\sqrt{\pi}}{2}\frac{\Gamma(\delta - \frac{1}{2})}{\Gamma(\delta)} A^{\frac{1}{2}-\delta}, \tag{3.14}$$

where Γ is the Euler's Γ function.

Proof
Using the variable change:

$$\frac{x^2}{A} = t, \qquad\qquad dx = \frac{A}{2\sqrt{t}}dt,$$

we obtain

$$\int_0^\infty \frac{1}{(A+x^2)^\delta}dx = \frac{1}{A^\delta}\int_0^\infty \frac{1}{\left(1+\frac{x^2}{A}\right)^\delta}dx = \frac{1}{2A^{\delta-\frac{1}{2}}}\int_0^\infty \frac{1}{(1+t)^\delta\sqrt{t}}dt.$$

Consider now another variable change:

$$\frac{1}{1+t} = y, \qquad\qquad dt = -\frac{1}{y^2}dy.$$

The integration extremes are $(1, 0)$, that we will invert changing the sign, thus we get

$$\frac{1}{2A^{\delta-\frac{1}{2}}}\int_0^\infty \frac{1}{(1+t)^\delta\sqrt{t}}dt = \frac{1}{2A^{\delta-\frac{1}{2}}}\int_0^1 \frac{y^{\delta-\frac{3}{2}}}{\sqrt{1-y}}.$$

Using the Euler's β function,

$$\beta(a,b) = \int_0^1 t^{a-1}(1-t)^{b-1}dt, \tag{3.15}$$

we have

$$\frac{1}{2A^{\delta-\frac{1}{2}}}\int_0^1 \frac{y^{\delta-\frac{3}{2}}}{\sqrt{1-y}} = \frac{1}{2A^{\delta-\frac{1}{2}}}\int_0^1 y^{\delta-\frac{1}{2}-1}(1-y)^{\frac{1}{2}-1} = \frac{\beta(\frac{1}{2},\delta-\frac{1}{2})}{2A^{\delta-\frac{1}{2}}},$$

where we have used equation 3.15 with $a = \delta - \frac{1}{2}$ and $b = \frac{1}{2}$. Given that

$$\beta(a,b) = \frac{\Gamma(a)\Gamma(b)}{\Gamma(a+b)} \tag{3.16}$$

and $\Gamma(\frac{1}{2}) = \sqrt{\pi}$, one obtains

$$\int_0^\infty (A+x^2)^{-\delta}dx = \frac{\beta(\frac{1}{2},\delta-\frac{1}{2})}{2A^{\delta-\frac{1}{2}}} = \frac{\sqrt{\pi}}{2}\frac{\Gamma(\delta-\frac{1}{2})}{\Gamma(\delta)}A^{\frac{1}{2}-\delta}.$$

We now can solve solve the integrals 3.12 and 3.13.

3.5.1 Face-on projected density

Let us consider the face-on projection. Substituting $\rho = \rho_0 R^2 r^{-\alpha}$ in eq. 3.12 we get

$$\Sigma(R) = 2\rho_0 a\int_0^\infty \frac{R^2}{r^\alpha}dz. \tag{3.17}$$

Using $r = (R^2+z^2)^{\frac{1}{2}}$, we get

$$\Sigma(R) = 2\rho_0 a R^2\int_0^\infty \frac{1}{(R^2+z^2)^{\frac{\alpha}{2}}}dz.$$

The integral converges for $\alpha > 1$ and thus for all the considered range of α in this work. The r.h.s. is in the same form as eq. 3.14, with $A = R^2$ and $\delta = \alpha/2$, thus we obtain

$$\Sigma(R) = \sqrt{\pi}\frac{\Gamma(\frac{\alpha-1}{2})}{\Gamma(\frac{\alpha}{2})}\frac{\rho_0 a}{R^{\alpha-3}}. \tag{3.18}$$

For $\alpha = 4$ the face-on density projection has the same functional form as the Mestel disk (Mestel, 1963) with $\Sigma(R) \propto 1/R$, another analogy in addition to the flat rotation curve, seen in sec. 3.4.

Fig. 3.7 shows the face-on projected surface density profile for different values of α. For $\alpha < 3$ the projected density increases with R and for lower values of α the profile is steeper. Otherwise for $\alpha > 3$ the projected surface density increases and for larger values of α the profile is steeper.

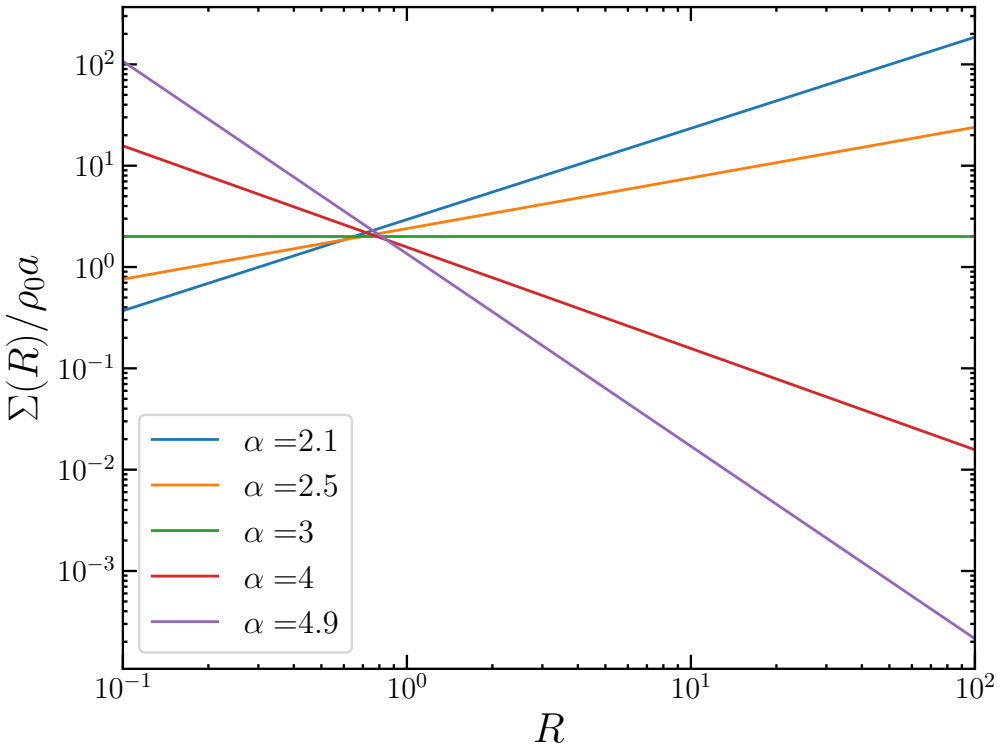

Figure 3.7: Face-on projected surface density, $\Sigma(R)$, as a function of radius R, for power-law tori with $\alpha = 2.1$, $\alpha = 2.5$, $\alpha = 3$, $\alpha = 4$, and $\alpha = 4.9$.

3.5.2 Edge-on projected density

Here we compute the edge-on projected surface density. Substituting $\rho = \rho_0 R^2 r^{-\alpha}$ in eq. 3.13 we get

$$\Sigma(R,z) = 2\rho_0 a \int_R^\infty \frac{R'^3 dR'}{(R'^2+z^2)^{\frac{\alpha}{2}}\sqrt{R'^2-R^2}}. \tag{3.19}$$

We rearrange this equation to get

$$\Sigma(R,z) = 2\rho_0 a \int_R^\infty \frac{(R'^3/R^3)R^3}{R^\alpha(\frac{R'^2+z^2}{R^2})^{\frac{\alpha}{2}}\sqrt{\frac{R'^2}{R^2}-1}}\frac{dR'}{R} =$$

$$= 2\frac{\rho_0 a}{R^{\alpha-3}} \int_R^\infty \frac{(R'^3/R^3)}{(\frac{R'^2+z^2}{R^2})^{\frac{\alpha}{2}}\sqrt{\frac{R'^2}{R^2}-1}}\frac{dR'}{R}.$$

Using the change of variables

$$y = \frac{R'}{R}, \qquad\qquad dy = \frac{dR'}{R},$$

we get

$$\Sigma(R,z) = 2\frac{\rho_0 a}{R^{\alpha-3}} \int_1^\infty \frac{y^3 dy}{(y^2+\frac{z^2}{R^2})^{\frac{\alpha}{2}}\sqrt{y^2-1}}.$$

Using

$$t = \sqrt{y^2-1}, \qquad\qquad dy = \frac{tdt}{\sqrt{t+1}},$$

we obtain

$$\Sigma(R,z) = 2\frac{\rho_0 a}{R^{\alpha-3}} \int_0^\infty \frac{t+1}{(t^2+1+\frac{z^2}{R^2})^{\frac{\alpha}{2}}}dt.$$

Adding and subtracting z^2/R^2 to the numerator of the integrand we have

$$\Sigma(R,z) = 2\frac{\rho_0 a}{R^{\alpha-3}} \int_0^\infty \frac{t+1+\frac{z^2}{R^2}-\frac{z^2}{R^2}}{(t^2+1+\frac{z^2}{R^2})^{\frac{\alpha}{2}}}dt =$$

$$= 2\frac{\rho_0 a}{R^{\alpha-3}}\left(\int_0^\infty \frac{t+1+\frac{z^2}{R^2}}{(t^2+1+\frac{z^2}{R^2})^{\frac{\alpha}{2}}}dt - \frac{z^2}{R^2}\int_0^\infty \frac{dt}{(t^2+1+\frac{z^2}{R^2})^{\frac{\alpha}{2}}}\right) =$$

$$= 2\frac{\rho_0 a}{R^{\alpha-3}}\left(\int_0^\infty \frac{dt}{(t^2+1+\frac{z^2}{R^2})^{\frac{\alpha-2}{2}}} - \frac{z^2}{R^2}\int_0^\infty \frac{dt}{(t^2+1+\frac{z^2}{R^2})^{\frac{\alpha}{2}}}\right). \tag{3.20}$$

Finally we have two integral in the form of equation 3.14. The former with $\delta = (\alpha - 2)/2$ and $A = 1 + z^2/X^2$ gives

$$\int_0^\infty \frac{dt}{(t^2 + 1 + \frac{z^2}{R^2})^{\frac{\alpha-2}{2}}} = \frac{\sqrt{\pi}}{2(1 + \frac{z^2}{R^2})^{\frac{\alpha-3}{2}}} \frac{\Gamma(\frac{\alpha-3}{2})}{\Gamma(\frac{\alpha-2}{2})}.$$

It converges for $\alpha > 3$, thus only tori with $\alpha > 3$ have a finite edge-on density projection. The latter integral with $\delta = \frac{\alpha}{2}$ and $A = 1 + \frac{z^2}{X^2}$ gives

$$\int_0^\infty \frac{dt}{(t^2 + 1 + \frac{z^2}{R^2})^{\frac{\alpha}{2}}} = \frac{\sqrt{\pi}}{2(1 + \frac{z^2}{R^2})^{\frac{\alpha-1}{2}}} \frac{\Gamma(\frac{\alpha-1}{2})}{\Gamma(\frac{\alpha}{2})}.$$

It converges for $\alpha > 1$ and thus for all α in the considered range. Substituting the solutions in equation 3.20, after some algebra, we get

$$\Sigma(R, z) = \sqrt{\pi}\rho_0 a \left(\frac{\Gamma(\frac{\alpha-3}{2})}{\Gamma(\frac{\alpha-2}{2})} \frac{1}{(R^2 + z^2)^{\frac{\alpha-3}{2}}} - \frac{\Gamma(\frac{\alpha-1}{2})}{\Gamma(\frac{\alpha}{2})} \frac{z^2}{(R^2 + z^2)^{\frac{\alpha-1}{2}}} \right). \tag{3.21}$$

Thanks to the property of Γ function, $\Gamma(z+1) = z\Gamma(z)$, we can rewrite the above Γ functions as

$$\Gamma\Big(\frac{\alpha-1}{2}\Big) = \Gamma\Big(\frac{\alpha-3}{2} + 1\Big) = \frac{\alpha-3}{2}\Gamma\Big(\frac{\alpha-3}{2}\Big)$$

and

$$\Gamma\Big(\frac{\alpha}{2}\Big) = \Gamma\Big(\frac{\alpha-2}{2} + 1\Big) = \frac{\alpha-2}{2}\Gamma\Big(\frac{\alpha-2}{2}\Big).$$

Thus the second term in the parenthesis of eq. 3.21 can be written as

$$-\frac{\Gamma(\frac{\alpha-1}{2})}{\Gamma(\frac{\alpha}{2})} \frac{z^2}{(R^2 + z^2)^{\frac{\alpha-1}{2}}} = -\frac{\Gamma(\frac{\alpha-3}{2})}{\Gamma(\frac{\alpha-2}{2})} \frac{(\alpha-3)}{(\alpha-2)} \frac{z^2}{(R^2 + z^2)^{\frac{\alpha-1}{2}}}.$$

Substituting this in eq. 3.21, we finally obtain

$$\Sigma(R, z) = \frac{\sqrt{\pi}\Gamma(\frac{\alpha-3}{2})\rho_0 a}{(\alpha-2)\Gamma(\frac{\alpha-2}{2})} \frac{\big[(\alpha-2)R^2 + z^2\big]}{r^{\alpha-1}}. \tag{3.22}$$

In fig. 3.8 are plotted the profiles of the edge-on projected surface density for $\alpha = 3.1$, $\alpha = 4$, and $\alpha = 4.9$ in the equatorial plane and along the z axis for $R = 0$. The profiles are power-law with slope $\alpha - 3$. The profile for $\alpha = 3.1$ is nearly flat, then the profiles have a steeper slope for larger values of α. Fig. 3.7 shows the edge-on projected surface density contours for $\alpha = 3.1$, $\alpha = 4$, and $\alpha = 4.9$ in the plane $x - z$, where x is a Cartesian coordinate orthogonal to z in the plane of the sky. For larger values of α the contours become rounder.

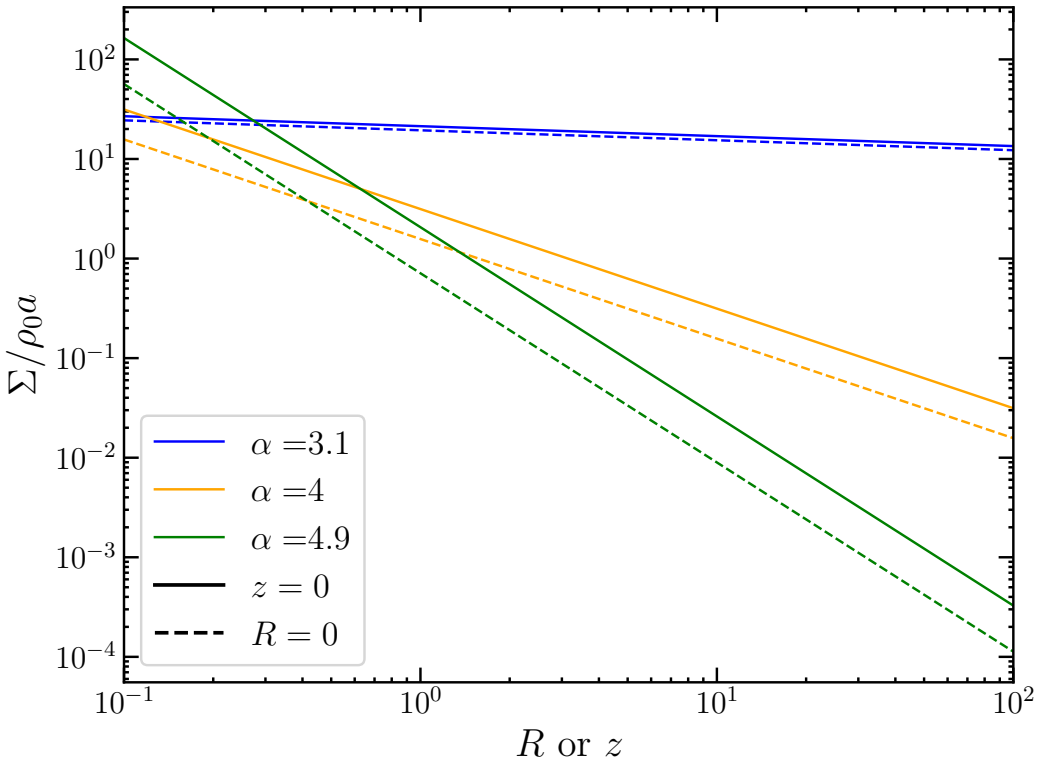

Figure 3.8: Edge-on projected surface density profiles for $z = 0$ and $R \neq 0$ (continuous line) and for $R = 0$ and $z \neq 0$ (dashed line) for power-law tori with $\alpha = 3.1$, $\alpha = 4$, and $\alpha = 4.9$.

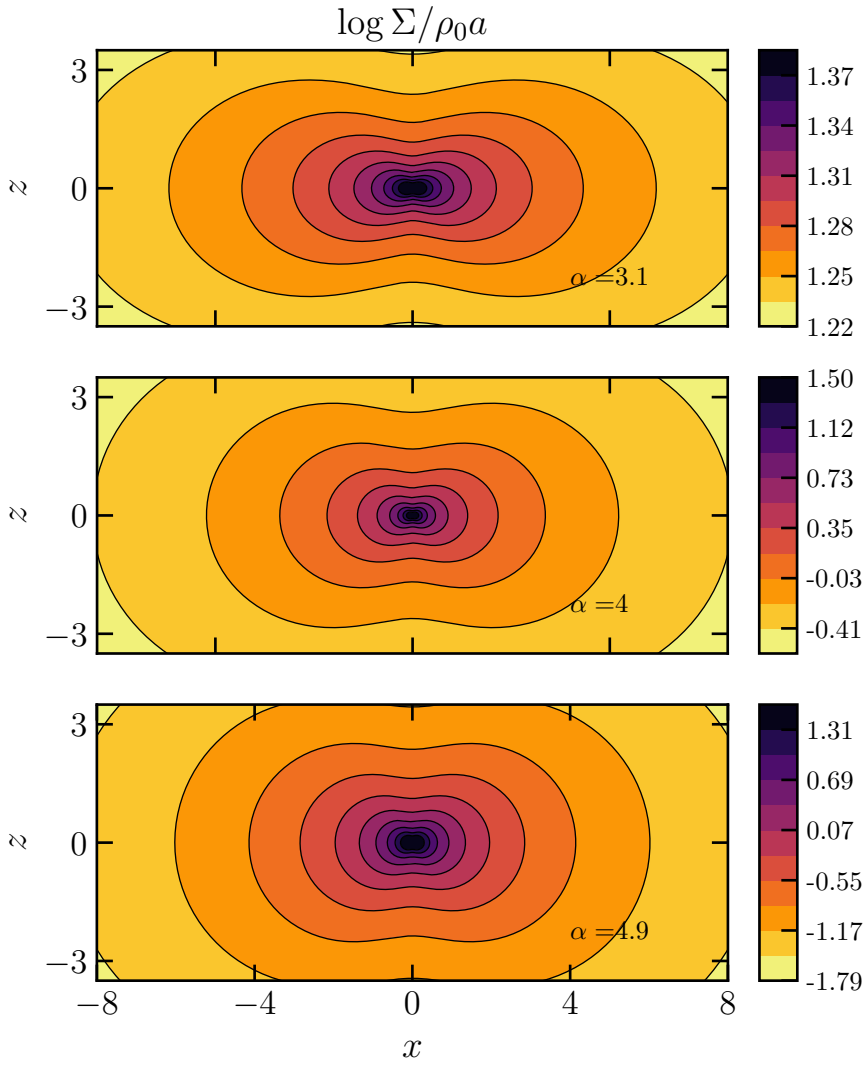

Figure 3.9: Edge-on projected surface density map for power-law tori with $\alpha = 3.1$, $\alpha = 4$, and $\alpha = 4.9$ (from top to the bottom).

3.6 Examples in physical units: molecular tori

In this section we present some examples in physical units of the surface density distributions of the power-law tori as seen face-on or edge-on. We take as reference the molecular tori obscuring the central parts of the AGNs, like those observed by Combes et al. (2019), and described briefly in sec. 1.1. Based on their observations, we chose a reference gas number density $n_0 = 10^4$ cm^{-3}. The reference mass density (in g cm^{-3}) is $\rho_0 = n_0 \mu m_{\rm p}$, where μ is the mean molecular weight and $m_{\rm p}$ is the proton mass. For a pure hydrogen molecular gas $\mu = 2$. The chosen reference scale is $a = 10$ pc. Substituting these reference values in eqs. 3.18 and 3.22 we obtain the surface number density $N \equiv \Sigma/(\mu m_{\rm p})$ in physical units. Figs. 3.10 and 3.11 show the face-on surface number density profiles and the edge-on surface number density maps[1], respectively, for different values of α. We note that the physical column densities of H_2 is in the range $10^{23} - 10^{25}$ cm^{-2}, comparable to the values measured by Combes et al. (2019) and described in sec. 1.1.

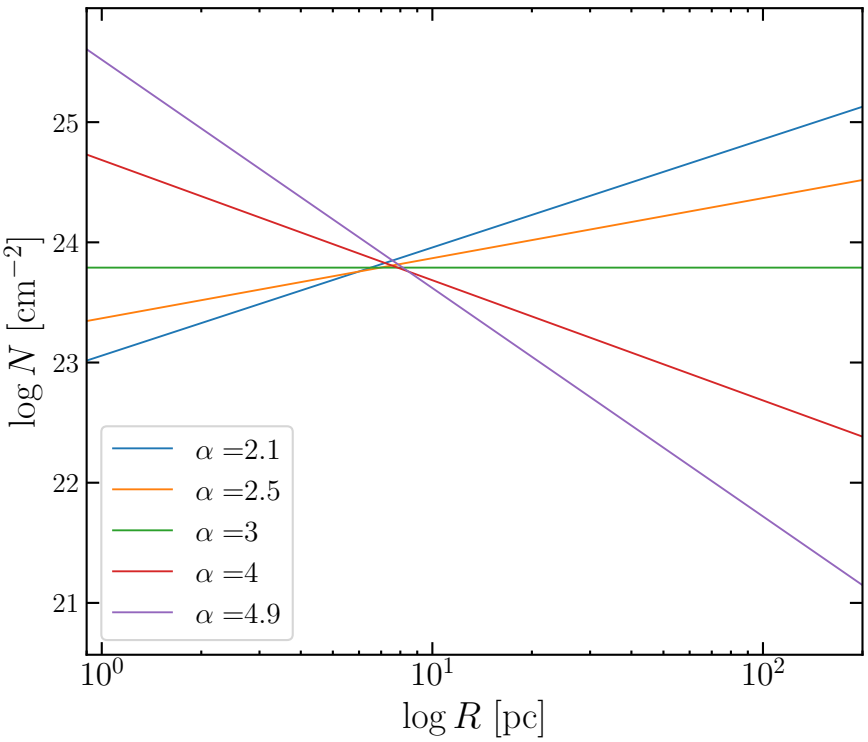

Figure 3.10: Face-on projected gas surface number density as a function of radius R, for power-law tori with $\alpha = 2.1$, $\alpha = 2.5$, $\alpha = 3$, $\alpha = 4$, and $\alpha = 4.9$, with a reference density $n_0 = 10^4$ cm^{-3} and a reference scale $a = 10$ pc.

[1]In the figures of this section, R, x, and z are not normalized to a, but are in physical units.

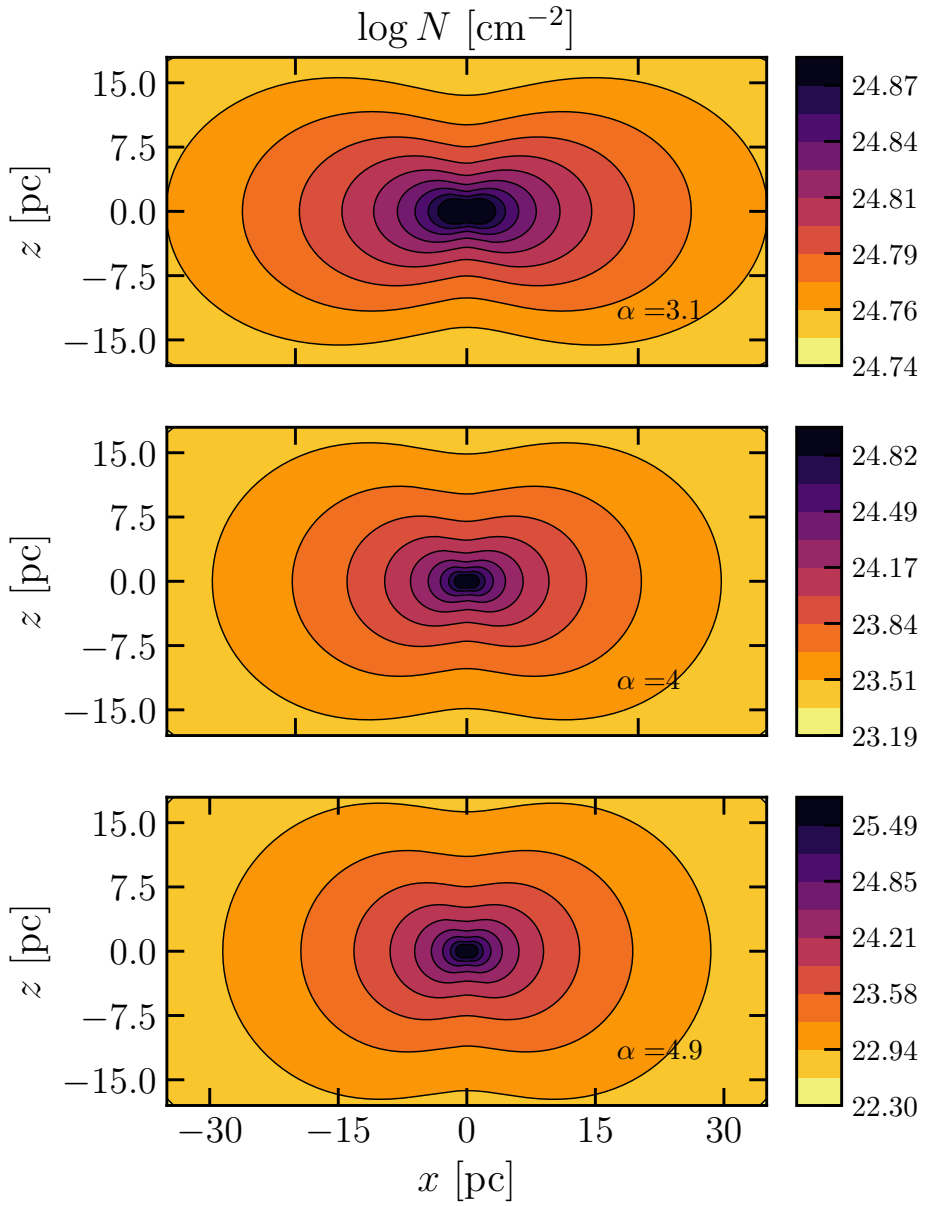

Figure 3.11: Edge-on projected gas surface number density maps for power-law tori with $\alpha = 3.1$, $\alpha = 4$, and $\alpha = 4.9$, with a reference density $n_0 = 10^4$ cm^{-3} and a reference scale $a = 10$ pc.

Chapter 4

Self-gravitating baroclinic power-law tori

In this chapter we consider stationary rotating self-gravitating fluid tori under the gravitational force of their potential. Hence we are in the self-gravitating case without external potentials, described in sec. 2.1. Starting from the integration of Euler equations we obtain the rotational velocity and temperature distributions (sec. 4.1). Then we will talk about the asymmetric drift (sec. 4.2) and finally, we present examples in physical units of AGN molecular tori based on the study by Combes et al. (2019) (sec. 4.3).

4.1 Stationary models

Given that the expression of the gravitational potential is different when $\alpha = 4$ and when $\alpha \neq 4$, it is convenient to treat separately the two cases.

Power-law tori with $\alpha = 4$

The potential-density pair obtained substituting $\alpha = 4$ is

$$\rho(R,z) = \rho_0 \frac{R^2}{r^4}, \tag{4.1}$$

$$\Phi(R,z) = \Phi_0 \frac{1}{3}\left[2\ln r - \frac{1}{2}\frac{R^2}{r^2}\right]. \tag{4.2}$$

The (R,z) components of the stationary Euler equation with $v_z = v_R = 0$, $v_\phi \neq 0$ are

$$\frac{1}{\rho}\frac{\partial P}{\partial R} = -\frac{\partial \Phi}{\partial R} + \Omega^2 R, \tag{4.3}$$

$$\frac{1}{\rho}\frac{\partial P}{\partial z} = -\frac{\partial \Phi}{\partial z}. \tag{4.4}$$

Integrating the z component of the Euler equation, one obtains

$$\int_z^\infty \frac{\partial P}{\partial z'} dz' = -\int_z^\infty \rho(R,z') \frac{\partial \Phi}{\partial z'} dz',$$

$$P(R,\infty) - P(R,z) = -\int_z^\infty \rho(R,z') \frac{\partial \Phi}{\partial z'} dz'. \tag{4.5}$$

Assuming that $P(R,\infty) = 0$, we get

$$P(R,z) = \int_z^\infty \rho(R,z') \frac{\partial \Phi}{\partial z'} dz'. \tag{4.6}$$

The partial derivative with respect to z of the potential is

$$\frac{\partial \Phi}{\partial z} = 4\pi G \rho_0 a z \frac{3R^2 + 2z^2}{3r^4}. \tag{4.7}$$

Substituting the expression of ρ and $\partial\Phi/\partial z$ and computing the integral we obtain the expression of the pressure for the $\alpha = 4$ torus

$$P(R,z) = 4\pi G \rho_0^2 a^2 R^2 \frac{4R^2 + 3z^2}{18r^6}. \tag{4.8}$$

The pressure is null along the z axis, where $R = 0$, according to the fact that $\rho(0,z) = 0$. Now, considering the R component of the Euler equation, we derive the angular velocity squared

$$\Omega^2 = \frac{1}{R\rho}\frac{\partial P}{\partial R} + \frac{1}{R}\frac{\partial \Phi}{\partial R}, \tag{4.9}$$

and then the rotational velocity squared $v_\phi^2 = \Omega^2 R^2$.

The partial derivatives of the pressure and the potential with respect to R are the following:

$$\frac{\partial P}{\partial R} = 4\pi G \rho_0^2 a R \frac{-4R^4 + 2R^2 z^2 + 3z^4}{9r^8}, \tag{4.10}$$

$$\frac{\partial \Phi}{\partial R} = 4\pi G \rho_0 a R \frac{2R^2 + z^2}{3r^4}. \tag{4.11}$$

Substituting equations 4.10 and 4.11 in eq. 4.9 we obtain

$$\Omega^2(R,z) = 4\pi G \rho_0 a^2 \frac{2R^2 + 3z^2}{9R^2 r^2}, \tag{4.12}$$

$$v_\phi^2(R,z) = 4\pi G \rho_0 a^2 \frac{2R^2 + 3z^2}{9r^2}. \tag{4.13}$$

The rotational velocity is constant in the equatorial plane; when $z = 0$ and $R \neq 0$, $v_\phi^2 = 2/9\Phi_0$. We recall that the circular velocity, in the equatorial plane is also constant (see sec. 3.4), but $v_c \neq v_\phi$ because of the asymmetric drift (see sec. 4.2).

Finally assuming that the system can be described by the ideal gas equation of state,

$$P = \frac{k_{\rm B}T}{\mu m_{\rm p}}\rho, \tag{4.14}$$

we can derive the temperature distribution. Hence we get

$$T = T_0\frac{4R^2+3z^2}{18r^2}, \tag{4.15}$$

with $T_0 = 4\pi G\rho_0 a^2 \mu m_{\rm p} k_B^{-1}$. As the velocity, the temperature is constant in the equatorial plane with value $T = \frac{2}{9}T_0$ for $z = 0$ and $R \neq 0$.

Power-law tori with $\alpha \neq 4$

We now analyze the case with $\alpha \neq 4$, recalling that α is in the range $2 < \alpha < 5$. The density potential pairs are

$$\rho(R,z) = \rho_0\frac{R^2}{r^\alpha}, \tag{4.16}$$

$$\Phi(R,z) = -\Phi_0\frac{r^{2-\alpha}}{(\alpha-2)(7-\alpha)}\left[\frac{4r^2}{(\alpha-4)(5-\alpha)}+R^2\right] \qquad (\alpha\neq 4). \tag{4.17}$$

or equivalently,

$$\Phi(R,z) = -\Phi_0\frac{(-\alpha^2+9\alpha-16)R^2+4z^2}{(7-\alpha)(5-\alpha)(\alpha-4)(\alpha-2)r^{\alpha-2}} \qquad (\alpha\neq 4),$$

Integrating the pressure from eq. (4.5), considering that the partial derivative of the potential w.r.t z is

$$\frac{\partial\Phi}{\partial z} = 4\pi G\rho_0 a z\frac{(-\alpha^2+7\alpha-6)R^2+4z^2}{(7-\alpha)(5-\alpha)(\alpha-2)r^\alpha}, \tag{4.18}$$

we obtain

$$P(R,z) = 4\pi G\rho_0^2 a^2\frac{R^2\left[(16-\alpha(\alpha-4)(\alpha-5))R^2+4(\alpha-1)z^2\right]}{2(7-\alpha)(5-\alpha)(\alpha-2)^2(\alpha-1)r^{2\alpha-2}}. \tag{4.19}$$

Similar to the case with $\alpha = 4$, the pressure vanishes along the z axis, consistent with the fact that ρ is null for $R = 0$. Computing the derivative w.r.t to R, we obtain

$$\frac{\partial P}{\partial R} = 4\pi G\rho_0^2 a^2 R\frac{-(\alpha-3)g(\alpha)R^4+2p(\alpha)R^2z^2+4(\alpha-1)z^4}{(7-\alpha)(5-\alpha)(\alpha-2)^2(\alpha-1)r^{2\alpha}}, \tag{4.20}$$

with $g(\alpha) \equiv 16 + \alpha(5-\alpha)(\alpha-4)$ and $p(\alpha) \equiv -a^3 + 7\alpha^2 - 14\alpha + 12$. Substituting in the R component of Euler equations (eq. 4.9), the eq. 4.20 and the partial derivative of Φ w.r.t R, which is

$$\frac{\partial \Phi}{\partial R} = 4\pi G\rho_0 aR \frac{(\alpha^2 - 9\alpha + 16)R^2 + 2(3-\alpha)z^2}{(7-\alpha)(5-\alpha)(\alpha-2)r^\alpha}, \tag{4.21}$$

we get

$$\Omega^2(R,z) = 4\pi G\rho_0 a^2 \frac{2\big[(\alpha^2 - 5\alpha + 8)R^2 + 2(\alpha-1)z^2\big]}{R^2(7-\alpha)(5-\alpha)(\alpha-2)^2(\alpha-1)r^{\alpha-2}}, \tag{4.22}$$

and

$$v_\phi^2(R,z) = 4\pi G\rho_0 a^2 \frac{2\big[(\alpha^2 - 5\alpha + 8)R^2 + 2(\alpha-1)z^2\big]}{(7-\alpha)(5-\alpha)(\alpha-2)^2(\alpha-1)r^{\alpha-2}}. \tag{4.23}$$

From the equation of state (eq. 4.14) we obtain the temperature distribution,

$$T(R,z) = T_0 \frac{(16 + \alpha(5-\alpha)(\alpha-4))R^2 + 4(\alpha-1)z^2}{2(7-\alpha)(5-\alpha)(\alpha-2)^2(\alpha-1)r^{\alpha-2}}, \tag{4.24}$$

with $T_0 = 4\pi G\rho_0 a^2 \mu m_\mathrm{p} k_B^{-1}$.

We note that equations 4.19 and 4.22-4.24 for $\alpha \neq 4$ reduce to those for $\alpha = 4$, substituting the value 4 on α, thus in the following we will use equations 4.19 and 4.22-4.24 that hold both for $\alpha \neq 4$ and $\alpha = 4$. We do not anymore have to split the two cases unless we deal with the potential expression.

Temperature and rotational velocity

To illustrate the proprieties of the family of tori we consider several particular cases of α in addition to the torus with $\alpha = 4$. We show the characteristics of the power-law tori with $\alpha = 2.1$ and $\alpha = 4.9$, i.e. the tori near the lower limit and the upper limit, respectively. Additionally, we show the power-law tori with $\alpha = 3$ and $\alpha = 4.5$, i.e. the tori with intermediate α between the limits and the case with $\alpha = 4$. Indeed, the torus temperature and rotational velocity distributions experience a change of trend between $\alpha < 4$ and $\alpha > 4$, and it is useful to see larger and lower α cases than the critical case with $\alpha = 4$.

The rotational velocity and temperature profiles in the equatorial plane and along the z axis for $R = 1$ and along the R axis for $z = 1$ for tori with $\alpha = 2.1$, $\alpha = 3$, $\alpha = 4.5$ and $\alpha = 4.9$ are plotted in figs. 4.1 and 4.2, respectively. We recall that the temperature and the rotational velocity for $\alpha = 4$ are constant on the equatorial plane. The tori with values of α lower than $\alpha = 4$ have velocity profiles which increase with R. In particular the lower it is the value of α, the stronger is the increase with R. Instead, for values of α larger than $\alpha = 4$, the velocity decreases with R, and the larger is the value of α the stronger is the decrease. The

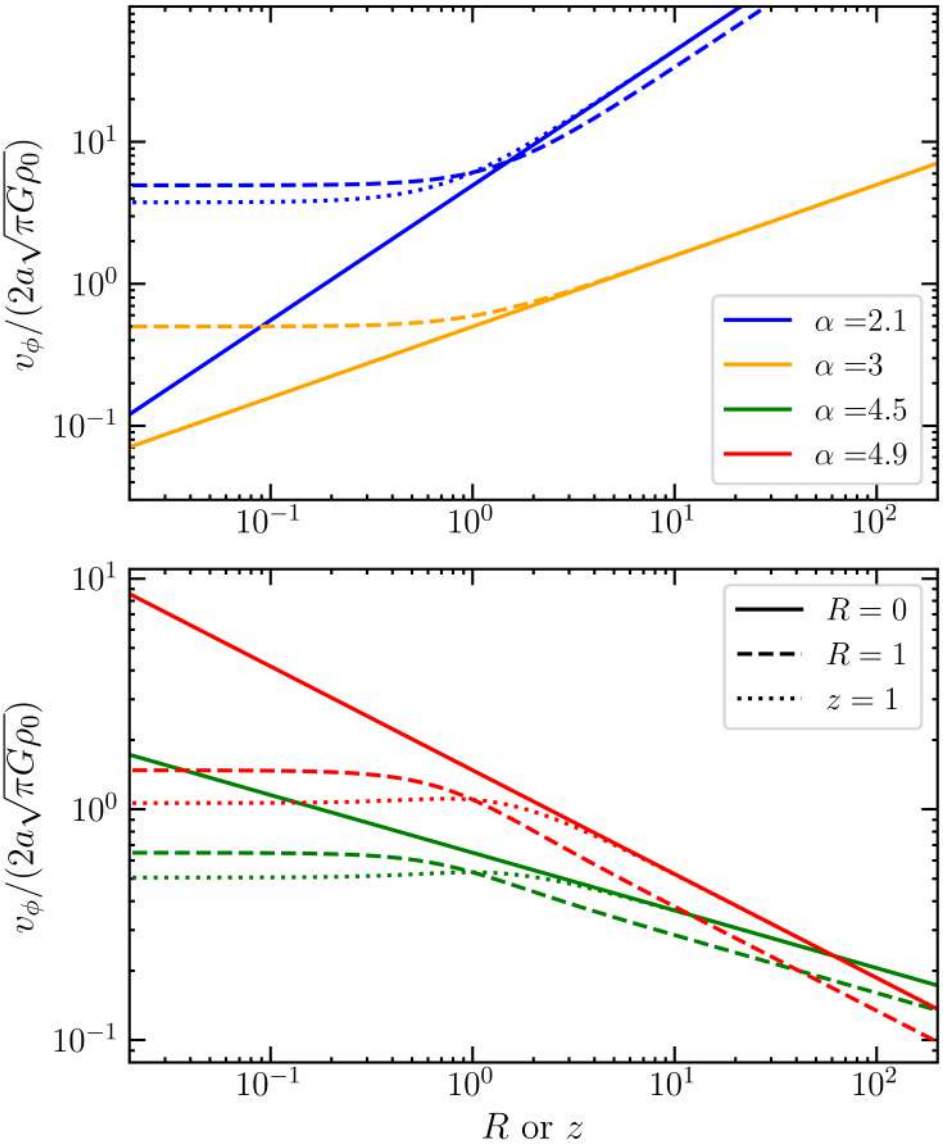

Figure 4.1: Rotation velocity profiles in the equatorial plane (solid line), along the z axis for $R = 1$ (dashed line), and along the R axis for $z = 1$ (dotted line) for power-law tori with $\alpha = 2.1$, $\alpha = 3$ (top), $\alpha = 4.5$ and $\alpha = 4.9$ (bottom). For the torus with $\alpha = 3$ the profiles along the R axis for $z = 1$ and along the z axis for $R = 1$ overlap.

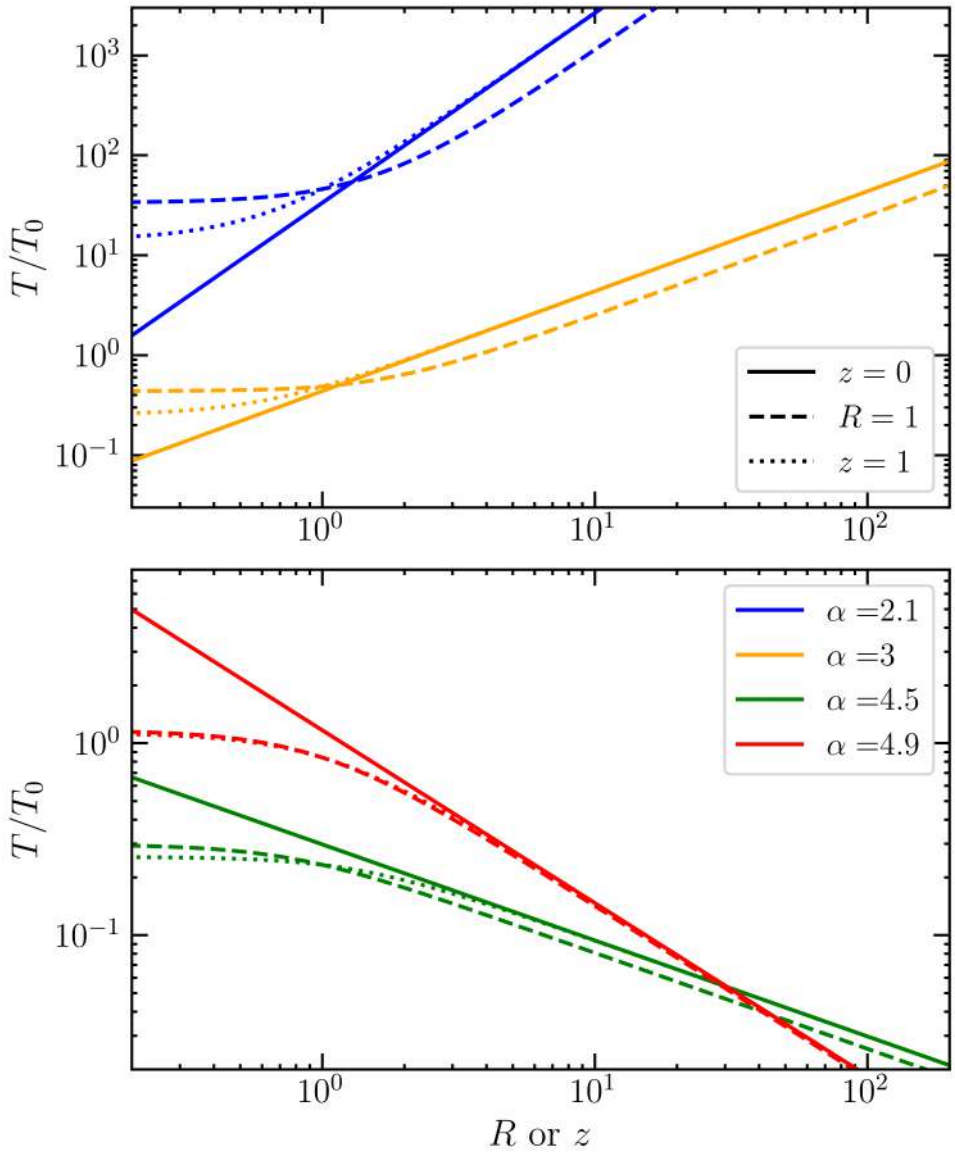

Figure 4.2: Temperature profiles in the equatorial plane (solid line), along the z axis for $R = 1$ (dashed line), and along the R axis for $z = 1$ (dotted line) for power-law tori with $\alpha = 2.1$, $\alpha = 3$ (top), $\alpha = 4.5$ and $\alpha = 4.9$ (bottom). For the torus with $\alpha = 4.5$ the profiles along the R axis for $z = 1$ and along the z axis for $R = 1$ overlap.

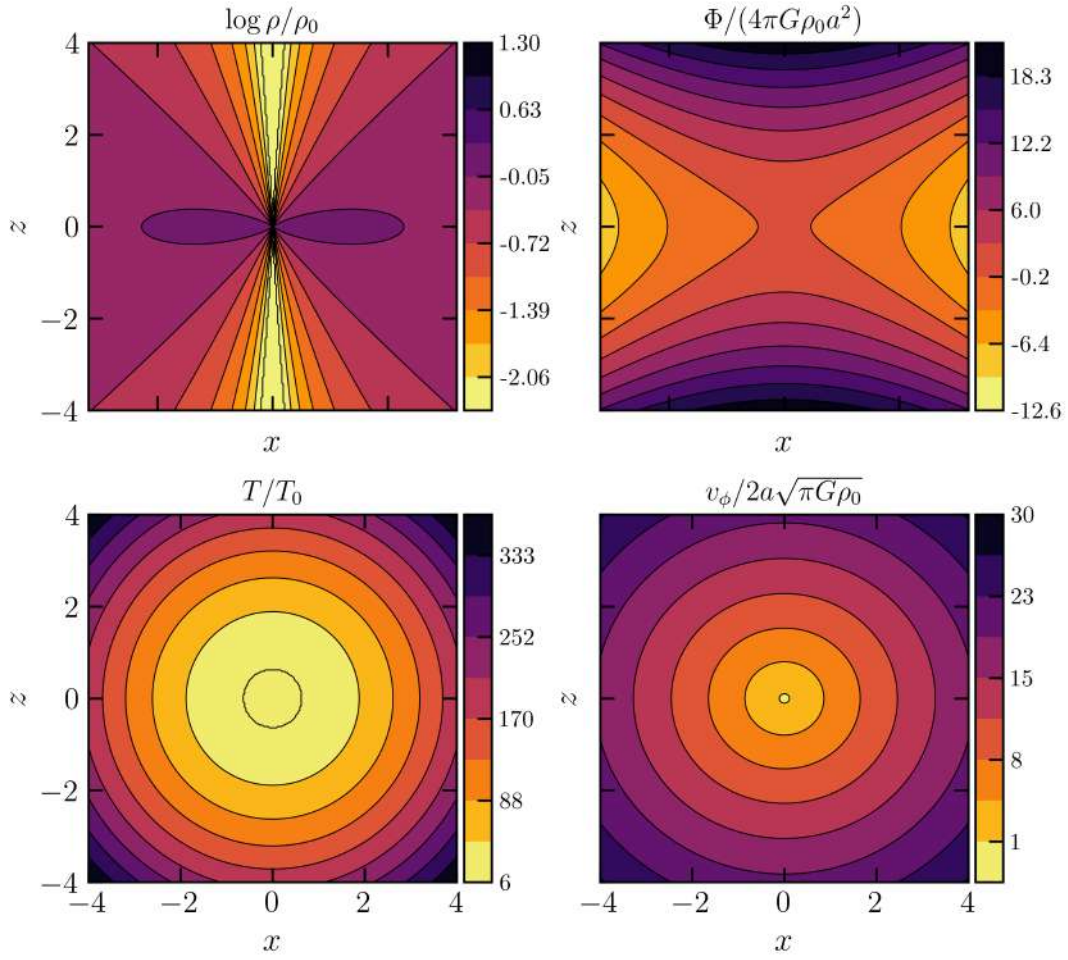

Figure 4.3: Top: density (left) and potential (right) maps for the self-gravitating power-law torus with $\alpha = 2.1$. Bottom: temperature (left) and rotational velocity (right) maps.

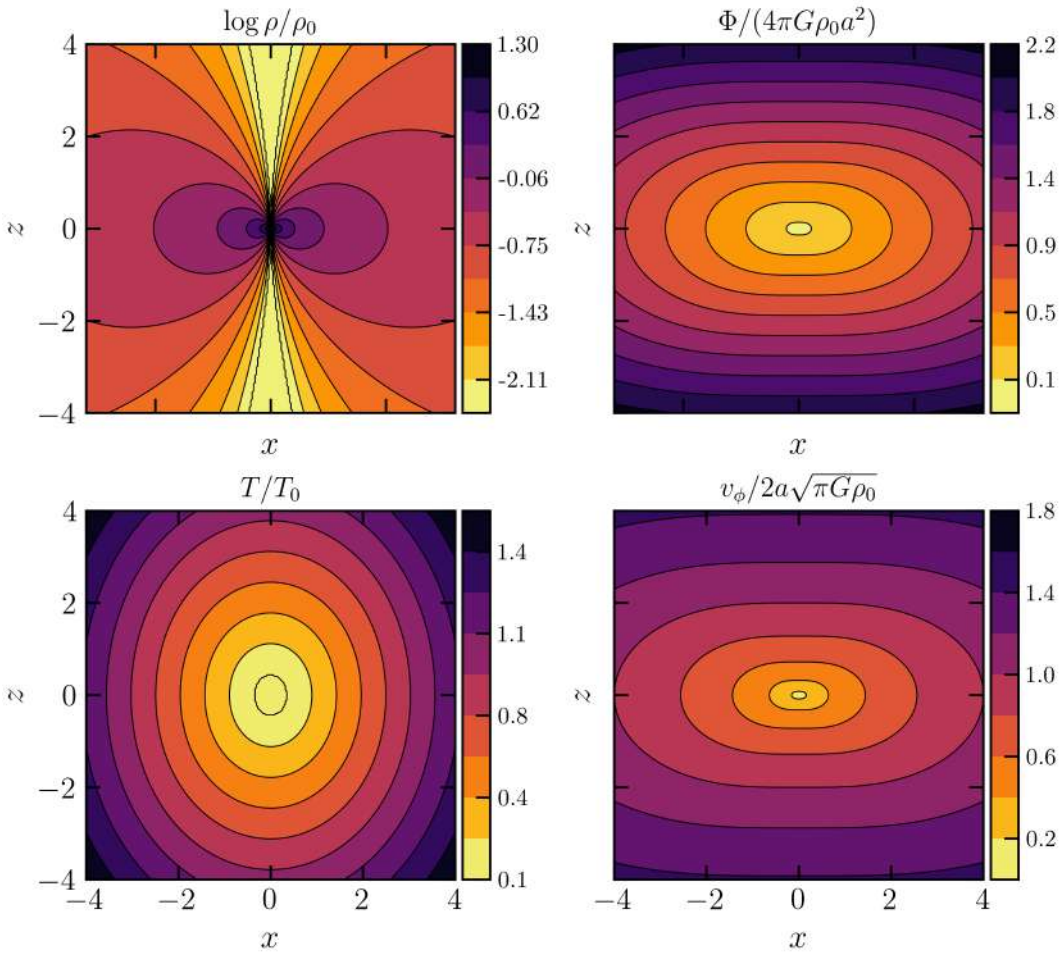

Figure 4.4: Top: density (left) and potential (right) maps for the self-gravitating power-law torus with $\alpha = 3$. Bottom: temperature (left) and rotational velocity (right) maps.

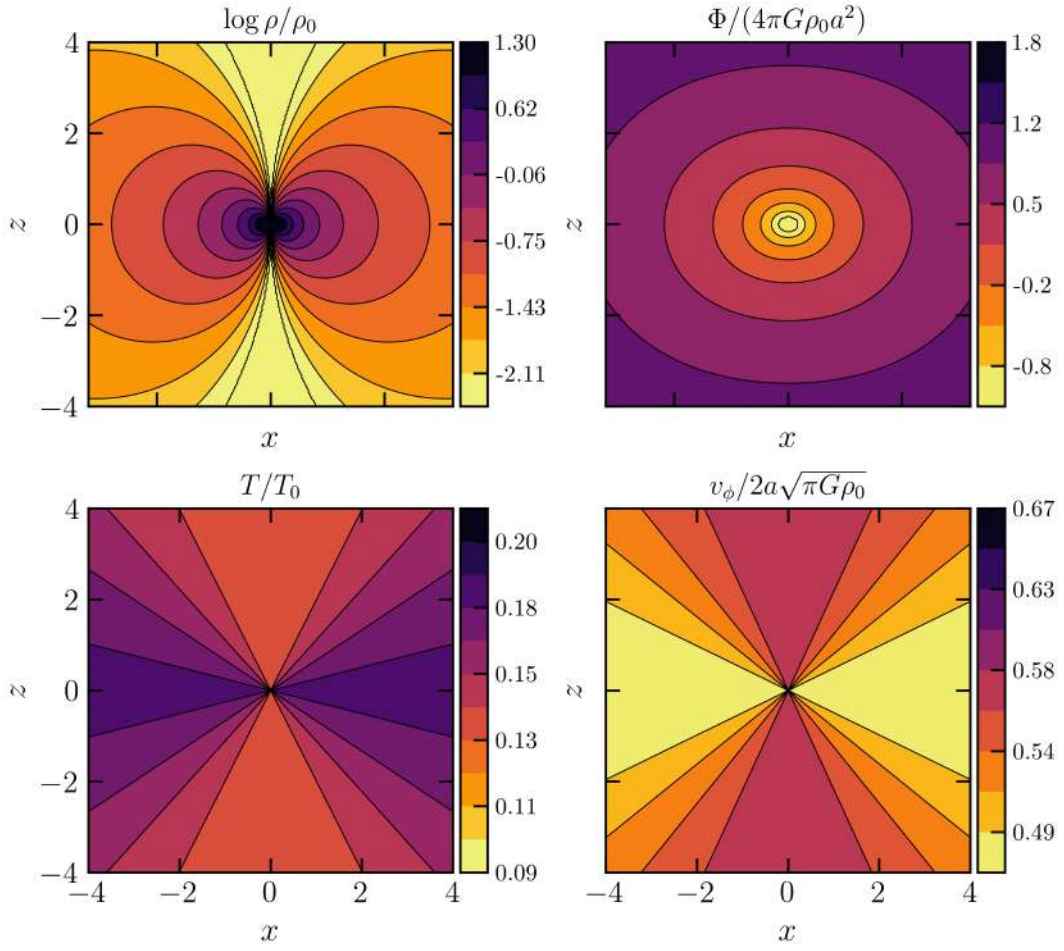

Figure 4.5: Top: density (left) and potential (right) maps for the self-gravitating power-law torus with $\alpha = 4$. Bottom: temperature (left) and rotational velocity (right) maps.

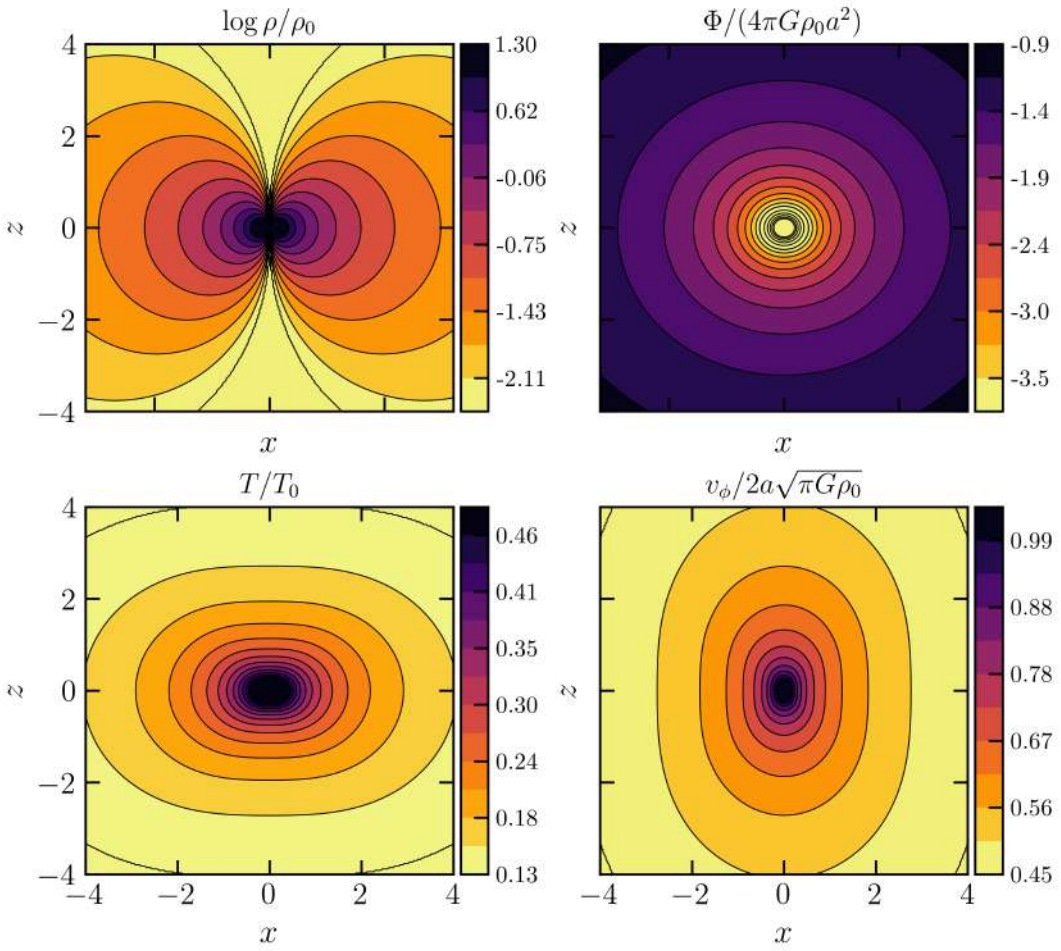

Figure 4.6: Top: density (left) and potential (right) maps for the self-gravitating power-law torus with $\alpha = 4.5$. Bottom: temperature (left) and rotational velocity (right) maps.

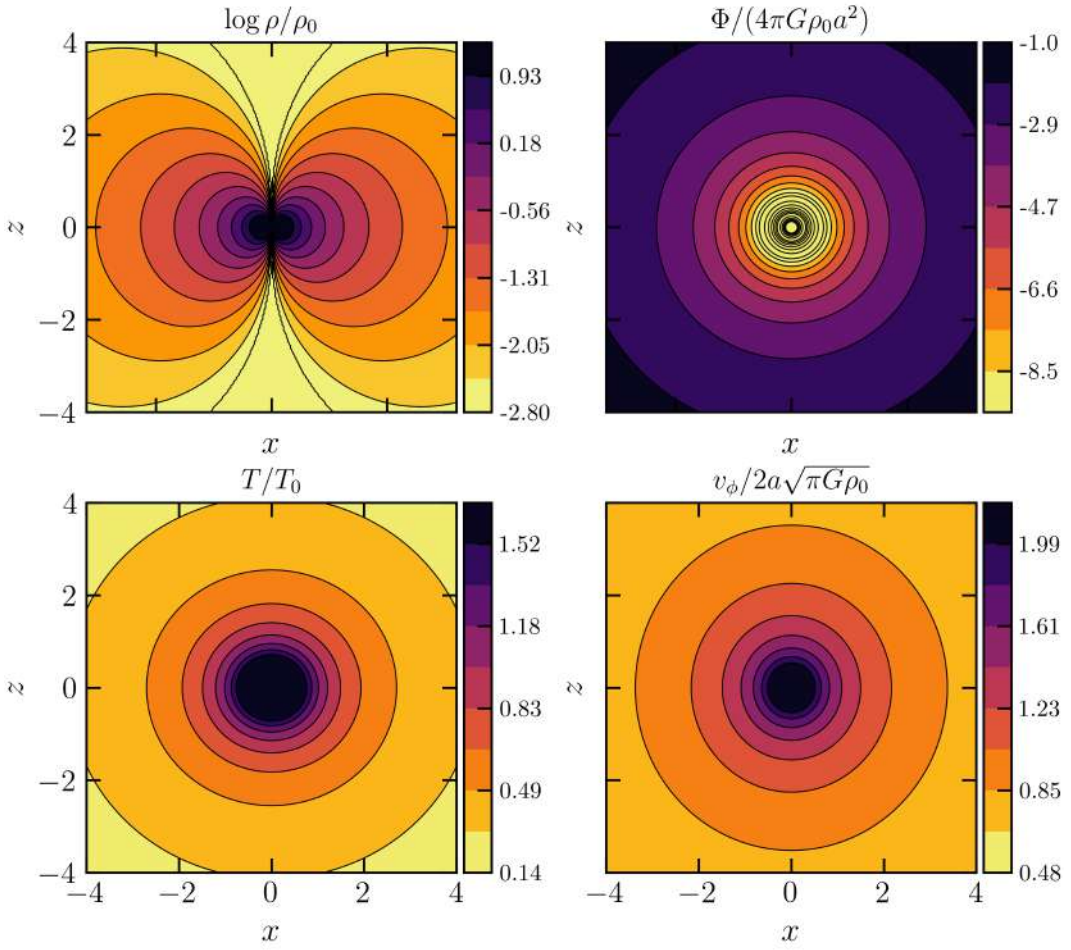

Figure 4.7: Top: density (left) and potential (right) maps for the self-gravitating power-law torus with $\alpha = 4.9$. Bottom: temperature (left) and rotational velocity (right) maps.

same behavior occurs to the temperature profiles but the temperature profiles are steeper than the velocity profiles, because $T \propto v^2$.

The distribution of density, gravitational potential, temperature and the velocity field of the power-law torus with $\alpha = 2.1$, $\alpha = 3$, $\alpha = 4$, $\alpha = 4.5$, and $\alpha = 4.9$ are plotted in figs. 4.3- 4.7. For $\alpha = 4$ (fig. 4.5) the temperature and velocity distributions are stratified on cones. The temperature is higher along the equatorial plane, where the rotational velocity is lower and vice versa. As already noted $\alpha = 4$ is a critical value. The change between $\alpha < 4$ and $\alpha > 4$ is not only in the gradient directions but also in the shape of the contours. For the torus with $\alpha = 3$ (fig. 4.4) the surfaces of equal temperature are like boxy ellipsoids elongated along the z axis, while those of equal velocity are elongated along the R axis. Both the temperature and the velocity increase outwardly. The torus with $\alpha = 4.5$ has the opposite trend (fig. 4.6). The surfaces of equal temperature and velocity are also boxy ellipsoids, but the isotemperature contours are elongated along the R axis and the isovelocity contours are elongated along the z axis. Both T and v_ϕ decrease for increasing distance from the center. The tori with α approaching the range limits , $\alpha = 2.1$ and $\alpha = 4.9$ (figs. 4.3 and 4.7) have the surfaces of equal temperature and equal velocity with nearly the same shape. The shape of the contours is nearly spherical for the two cases. The temperature and the rotational velocity increase for increasing distance from the center for the torus with $\alpha = 2.1$, instead T and v_ϕ decrease for increasing distance for the torus with $\alpha = 4.9$.

4.2 Asymmetric drift

The asymmetric drift is a measure of the difference between the circular velocity and the rotational velocity in the equatorial plane (Binney and Tremaine, 2008). Here we consider only models with $\alpha > 2.44$, because the circular velocity does not exists for lower α. We compute $v_c^2 - v_\phi^2$, $v_c - v_\phi$ and $\frac{v_c - v_\phi}{v_c}$. Starting from the first, we find that

$$v_\phi^2(R) - v_c^2(R) = \frac{R}{\rho}\frac{\partial P}{\partial R}\bigg|_{z=0}. \tag{4.25}$$

Considering the equations (4.20) and (4.17) we get

$$\frac{R}{\rho}\frac{\partial P}{\partial R}\bigg|_{z=0} = -4\pi G\rho_0 a^2 \frac{(16 + \alpha(5-\alpha)(\alpha-4))}{(7-\alpha)(5-\alpha)(\alpha-2)^2(\alpha-1)}(\alpha-3)R^{4-\alpha}. \tag{4.26}$$

The polynomial $(16 + \alpha(5-\alpha)(\alpha-4))$ is positive in the α range of interest. This equation experiences two changes of trend: for $\alpha = 3$ and for $\alpha = 4$. Indeed, the radial derivative of the pressure at $z = 0$ is positive for $\alpha < 3$, vanishes for $\alpha = 3$, and is negative for $\alpha > 3$. In practice, the pressure in the equatorial

plane increases with R for $\alpha < 3$, is constant for $\alpha = 3$, and decreases for $\alpha > 3$. This implies that $v_\phi^2 > v_c^2$ for $\alpha = 3$, $v_\phi^2 = v_c^2$ for $\alpha = 3$, and $v_\phi^2 < v_c^2$ for $\alpha > 3$. Moreover, the quantity $v_\phi^2 - v_c^2$ increases with R for $\alpha < 4$, is constant for $\alpha = 4$ and decreases with R for $\alpha > 4$. Thus we have three range of behavior $2.44 < \alpha < 3$, $3 < \alpha < 4$ and $4 < \alpha < 5$. Fig. 4.8 shows the quantity $v_c - v_\phi$ evaluated for $\alpha = 4.8$, $\alpha = 4.4$ (top), $\alpha = 3.8$, $\alpha = 3.2$ (middle), and $\alpha = 2.8$, $\alpha = 2.5$ (bottom). For $2.44 < \alpha < 3$ the rotational velocity is higher than the circular velocity, their difference increases with R and the lower is the value of α the stronger is the increase. For $3 < \alpha < 4$, the circular velocity is higher than the rotational one, their difference increases with R and the lower is the value of α the stronger is the increase. For $4 < \alpha < 5$ the circular velocity is higher than the rotational one, their difference decreases with R and the larger is the value of α the stronger is the decrease. $v_c - v_\phi$ for $\alpha = 3.8$ and $\alpha = 4.2$ is nearly constant, as expected because these values are close to $\alpha = 4$, for which $v_c - v_\phi$ is constant in the equatorial plane.

The normalized asymmetric drift $(v_c - v_\phi)/v_c$ is constant along R since the factors that appear in it have the same dependence with R. Therefore it is a function only of α:

$$\frac{v_c - v_\phi}{v_c} = 1 - \sqrt{\frac{2(\alpha^2 - 5\alpha + 8)}{(\alpha - 1)(\alpha - 2)(-\alpha^2 + 9\alpha - 16)}} \tag{4.27}$$

In the limit of $\alpha \to \frac{9-\sqrt{17}}{2} \approx 2.44$, $(v_c - v_\phi)/v_c \to -\infty$. Fig. 4.9 shows the normalized asymmetric drift for different values of α. We note the divergence for α approaching 2.44, then $(v_c - v_\phi)/v_c$ increase with α and for larger values of α is quite the same.

4.3 Examples in physical units: self-gravitating molecular tori

In this section, we show examples in physical units of the self-gravitating tori presented in this chapter. For this purpose, in the expressions of the density, potential, temperature and velocity distributions we substitute, in addition to the physical constants, specific values of the reference scale and density to obtain characteristic quantities of the astrophysical objects. As seen in section 3.6, we take as reference the molecular tori observed by Combes et al. (2019) and described in sec. 1.1. In equations 3.1 and 4.23, we substitute a reference scale of $a = 10$ pc and a reference density of $n_0 = 10^4$ cm^{-3}. Given that the observed molecular tori are expected to be turbulent (with turbulent pressure dominating over thermal

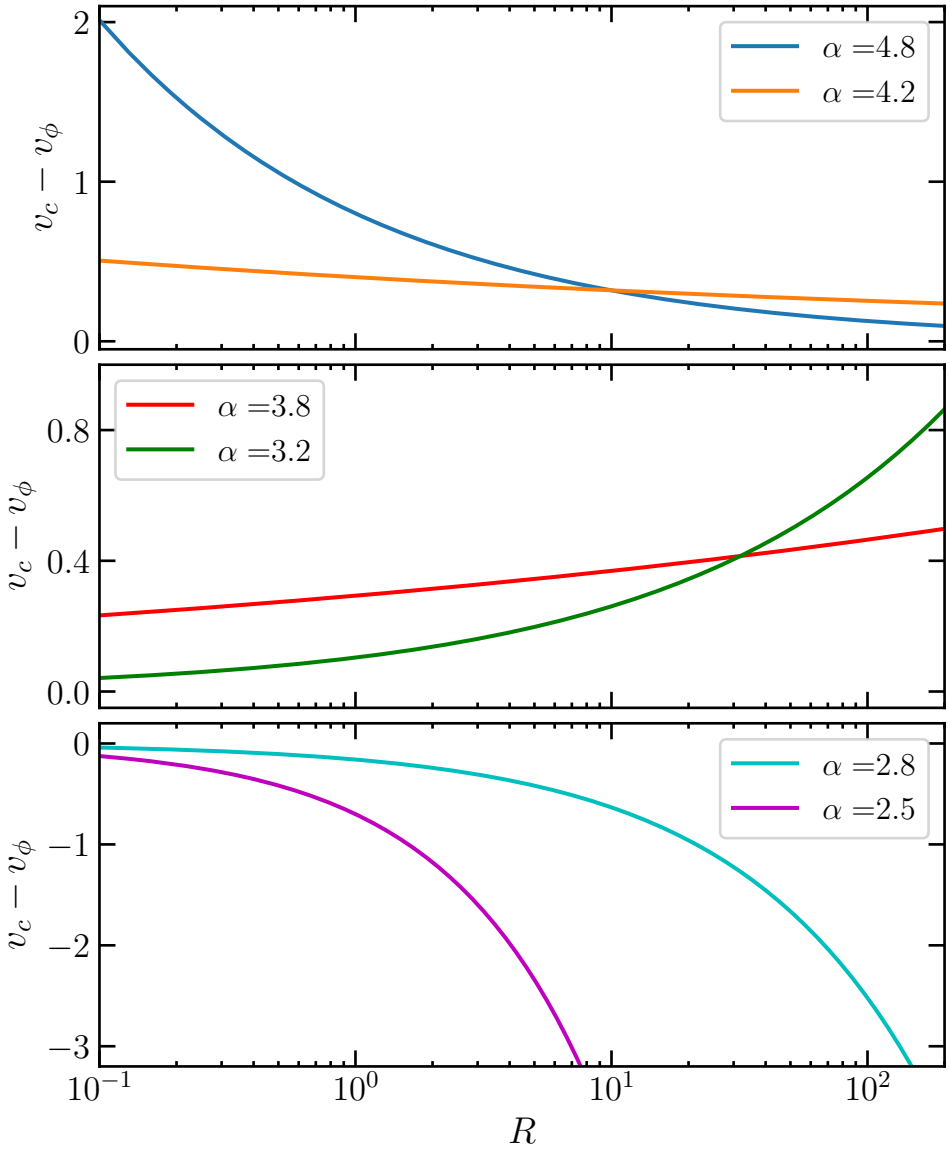

Figure 4.8: The asymmetric drift $v_c - v_\phi$ in the equatorial plane for power-law tori with $\alpha = 4.8$, 4.2 (top), 3.8, 3.2 (middle), 2.8, and 2.5 (bottom). v_c and v_ϕ are normalized to $2a\sqrt{\pi G\rho_0}$.

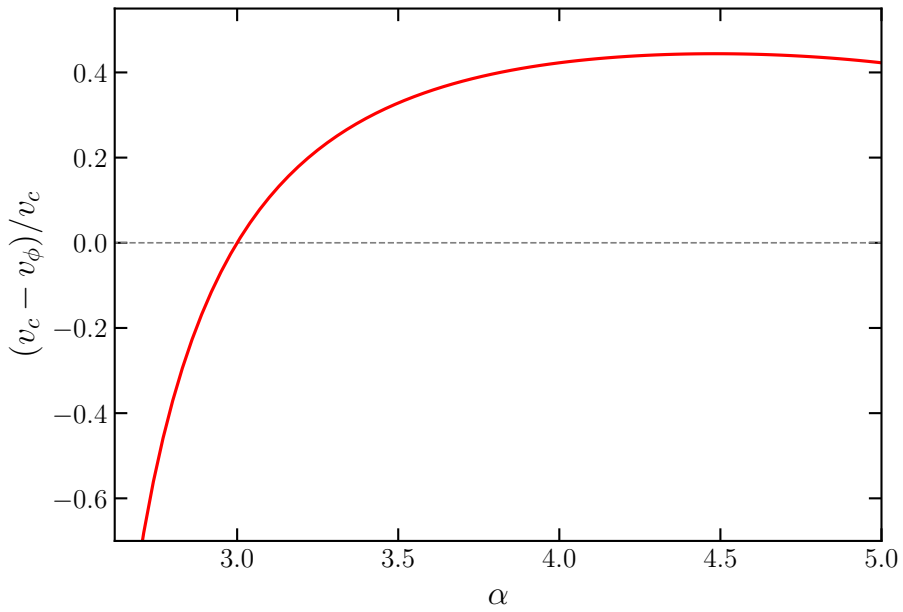

Figure 4.9: The normalized asymmetric drift $(v_c - v_\phi)/v_c$ in the equatorial plane for power-law tori for different values of α.

pressure), we compute the gas velocity dispersion as

$$\sigma_{\rm g} \equiv \sqrt{\frac{P}{\rho}}. \tag{4.28}$$

Figs.[1] 4.10-4.12 show the density, the gravitational potential, the velocity dispersion and the rotational velocity of the self-gravitating power-law tori without external potential, for $\alpha = 3$, $\alpha = 4$ and $\alpha = 4.5$. We chose these three values to illustrate the main different behaviours of the quantities for different α, as largely seen in this chapter. We note that velocity dispersion and rotational velocity have the same orders of magnitude of those observed by Combes et al. (2019) and described in sec. 1.1.

[1]In the figures of this section, R, x and z are not normalized to a, but are in physical units.

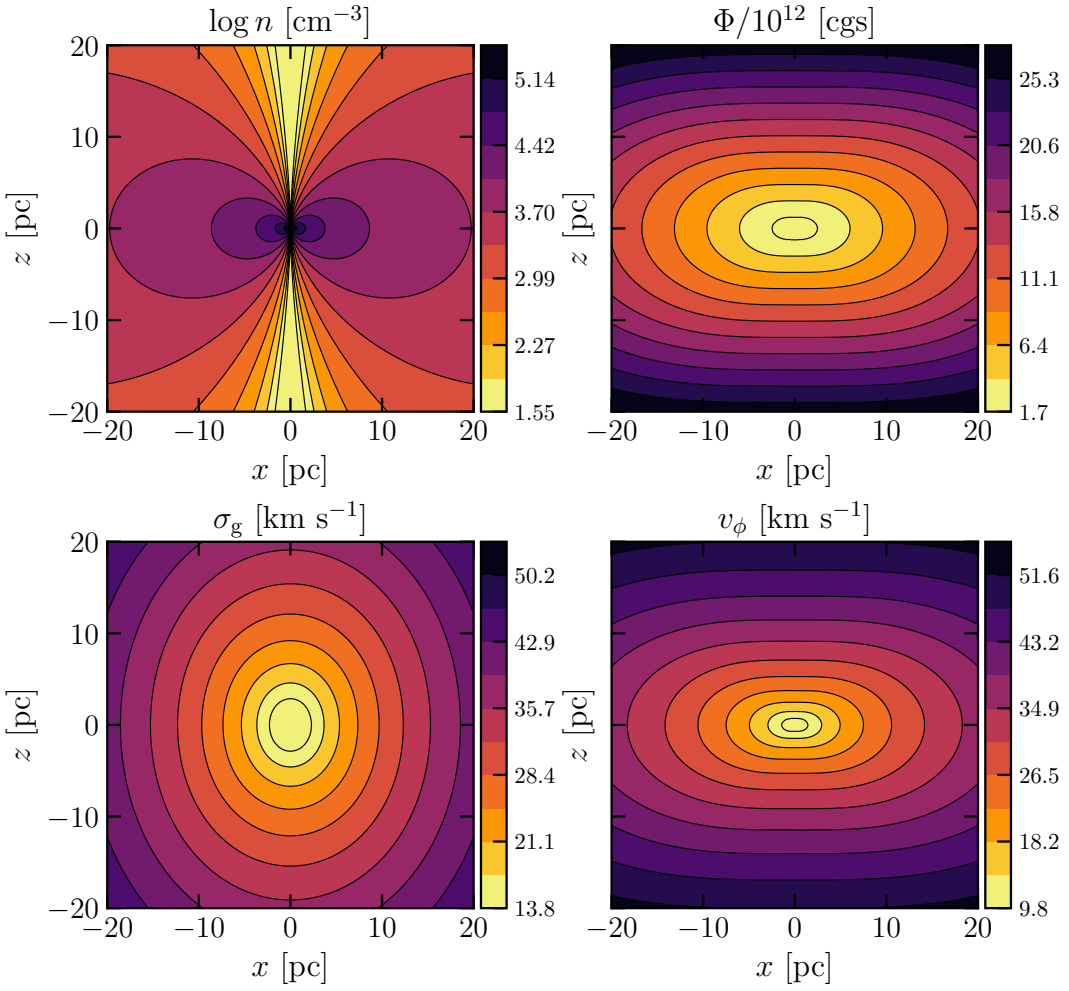

Figure 4.10: Top: density (left) and potential (right) maps for the self-gravitating power-law torus with $\alpha = 3$. Bottom: velocity dispersion (left) and rotational velocity (right) maps. The reference scale and density are $a = 10$ pc and $n_0 = 10^4$ cm^{-3}, respectively.

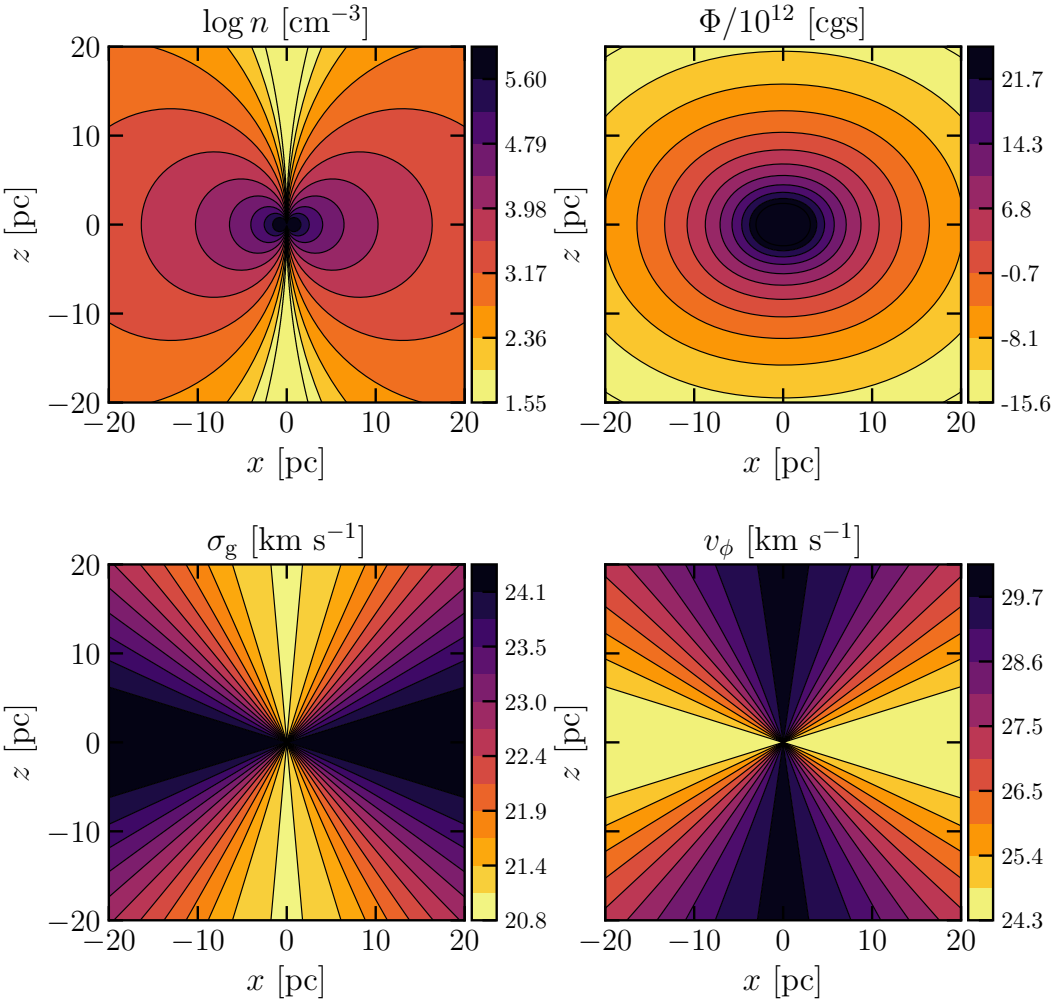

Figure 4.11: Top: density (left) and potential (right) maps for the self-gravitating power-law torus with $\alpha = 4$. Bottom: velocity dispersion (left) and rotational velocity (right) maps. The reference scale and density are $a = 10$ pc and $n_0 = 10^4$ cm^{-3}, respectively.

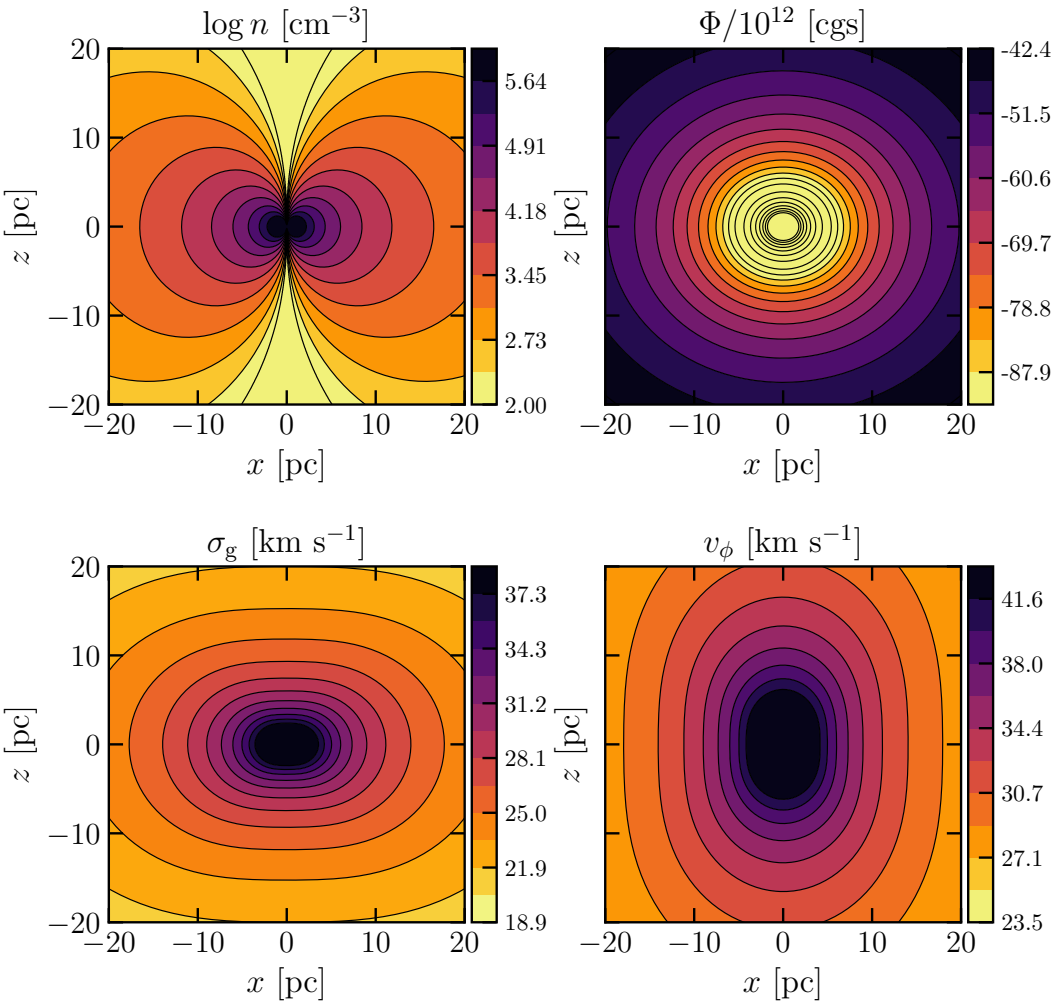

Figure 4.12: Top: density (left) and potential (right) maps for the self-gravitating power-law torus with $\alpha = 4.5$. Bottom: velocity dispersion (left) and rotational velocity (right) maps. The reference scale and density are $a = 10$ pc and $n_0 = 10^4$ cm^{-3}, respectively.

Chapter 5

Power-law tori with central black hole

In this chapter we analyze the power-law tori with a point mass placed in their center. This point mass represents the central black hole that could be present in the astrophysical systems at which these models can be applied. The black hole addition makes the models more complete and, depending to the black hole mass, can affect strongly the physical properties of the system.

5.1 The black hole gravitational potential

A black hole with mass M_{BH} is placed at the origin of the system. We consider Newtonian models, i.e. not relativistic, thus we assume that the black hole potential is Keplerian $\propto 1/r$. Therefore the black hole produces a gravitational potential

$$\Phi_{BH} = -\frac{GM_{BH}}{ar}, \tag{5.1}$$

where we recall that r is in unit of the reference length scale a. We define the normalized black hole mass

$$\mu_{\rm BH} \equiv \frac{M_{BH}}{4\pi\rho_0 a^3}, \tag{5.2}$$

where ρ_0 is the reference density. The black hole gravitational potential can be rewritten in terms of $\mu_{\rm BH}$ as

$$\Phi_{BH} = -4\pi G\rho_0 a^2 \frac{\mu_{\rm BH}}{r}. \tag{5.3}$$

As well known the gravitational force produced by a point mass is stronger for increasing mass and for decreasing distance. Thus the black hole effects get stronger for massive black holes and/or near the center. The isopotential surfaces are spheres. Fig. 5.1 shows the maps, in the meridional plane, of the total gravitational potential $\Phi_{\rm tot} = \Phi_{\rm BH} + \Phi$ due to the sum of the black hole potential $\Phi_{\rm BH}$

and the torus potential Φ, for $\alpha = 2.1$, $\alpha = 2.5$, $\alpha = 3$, and $\alpha = 4$. The presence of the gravitational field of the black hole makes the contours nearly circular close to the center. In particular, at the distances considered in the figure all the contours for the system with $\alpha = 4$ are nearly circular and this holds also for the cases with $\alpha = 4.5$ and $\alpha = 4.9$ not shown in the figure.

We, finally, note that, in the presence of both the torus self-gravity and of the black hole potential, the squared circular velocity is

$$v_c^2 = \left.\frac{\partial \Phi_{\rm tot}}{\partial R}\right|_{z=0} = 4\pi G \rho_0 a^2 \left(\frac{\mu_{\rm BH}}{r} + \frac{-\alpha^2 + 9\alpha - 16}{(7-\alpha)(5-\alpha)(\alpha-2)} R^{4-\alpha} \right). \tag{5.4}$$

In the absence of the black hole ($\mu_{\rm BH} = 0$), we have found that the squared circular velocity is negative, and thus circular orbits do not exist, for $\alpha < 2.44$ (sec. 3.4). Since the term $\mu_{\rm BH}/r$ is always positive, we note that v_c^2 in the presence of the black hole (eq. 5.4) can be positive also for $\alpha < 2.44$ as long as

$$\frac{\mu_{\rm BH}}{r} > \left| \frac{-\alpha^2 + 9\alpha - 16}{(7-\alpha)(5-\alpha)(\alpha-2)} R^{4-\alpha} \right|.$$

5.2 Linearity of stationary fluid dynamics equation and superposition principle

The stationary fluid dynamics equations are linear, thus we can apply the superposition principle. In equations 4.3 and 4.4, we replace the self-gravitating potential Φ, with the total gravitational potential due to the sum of the gas gravitational potential and the black hole gravitational potential $\Phi_{\rm tot} = \Phi + \Phi_{\rm BH}$.

The R and z components of Euler equations that we have to solve are

$$\frac{1}{\rho}\frac{\partial P}{\partial R} = -\frac{\partial \Phi_{\rm tot}}{\partial R} + \Omega^2 R, \tag{5.5}$$

$$\frac{1}{\rho}\frac{\partial P}{\partial z} = -\frac{\partial \Phi_{\rm tot}}{\partial z}. \tag{5.6}$$

Using the linearity of the equations we can write $P = P_{\rm BH} + P_{\rm self}$ and $\Omega = \Omega_{\rm BH} + \Omega_{\rm self}$, where the subscript *self* refers to the quantities due to the self-gravity of the torus Φ, and the subscript *BH* refers to the ones due to the gravitational potential of the black hole $\Phi_{\rm BH}$. This holds also for the system temperature, $T = T_{\rm BH} + T_{\rm self}$.

In principle, there is no problem to derive straightly the physical properties due to the total gravitational potential by solving the Euler equations 5.5 and 5.6, but it is convenient to obtain the properties separately and then to add them. Moreover, we have already obtained the physical properties for the self-gravitating

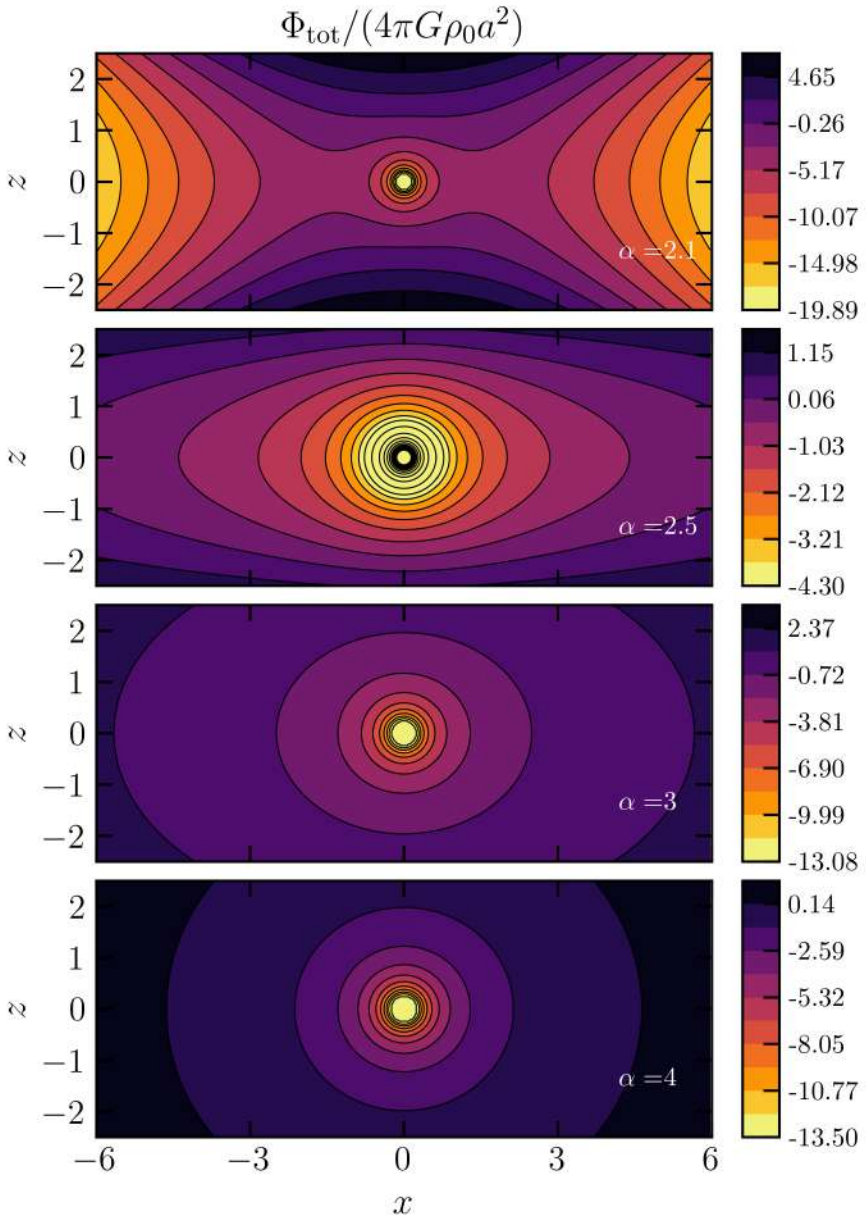

Figure 5.1: Maps, in the meridional plane, of the total gravitational potential due to the sum of the tori and the black hole gravitational potential for power-law tori with $\alpha = 2.1$, $\alpha = 2.5$, $\alpha = 3$ and $\alpha = 4$ (from top to the bottom) with $\mu_{\rm BH} = 10$.

case in absence of the black hole. Therefore we will compute the characteristics of the systems under the gravitational force due only to the black hole and then we will obtain the physical properties due to the total gravitational potential simply by adding the two components.

We recall that the density distribution of the torus remains unchanged. The model is composed of two separate systems: a fixed density distribution, i.e. the power-law torus, plus a central black hole. Apart from the density, the other physical properties depend on both gravitational fields.

5.3 Power-law tori in equilibrium in the black hole gravitational potential, $\Phi_{\rm tot} = \Phi_{\rm BH}$

We now consider the power-law tori density distribution under the influence of the black hole only. Since the tori potential (eqs. 3.2, 3.3) is not considered, we do not have to split the $\alpha = 4$ and $\alpha \neq 4$ cases.

The stationary fluid-dynamics equations that we have to solve are

$$\frac{1}{\rho}\frac{\partial P_{BH}}{\partial R} = -\frac{\partial \Phi_{\rm BH}}{\partial R} + \Omega_{BH}^2 R, \tag{5.7}$$

$$\frac{1}{\rho}\frac{\partial P_{BH}}{\partial z} = -\frac{\partial \Phi_{\rm BH}}{\partial z}. \tag{5.8}$$

Integrating the Euler equations z component, following the steps of sec. 4.1, we have to solve

$$P_{BH}(R,z) = \int_z^\infty \rho(R,z')\frac{\partial \Phi_{BH}}{\partial z'}dz', \tag{5.9}$$

where ρ is that of eq. 3.1, and the partial derivative w.r.t. z of the black hole gravitational potential is

$$\frac{\partial \Phi_{\rm BH}}{\partial z} = 4\pi G\rho_0 a\frac{\mu_{\rm BH} z}{r^3}. \tag{5.10}$$

Solving the integral, we obtain

$$P_{BH}(R,z) = \frac{4\pi G\rho_0^2 a^2}{(\alpha+1)}\frac{\mu_{\rm BH} R^2}{r^{\alpha+1}}. \tag{5.11}$$

Substituting the partial derivative of P_{BH} w.r.t. R,

$$\frac{\partial P_{BH}}{\partial R} = -4\pi G\rho_0^2 a\mu_{\rm BH}\frac{(\alpha-1)R^2 + 2z^2}{(\alpha+1)r^{\alpha+3}}R, \tag{5.12}$$

and the partial derivative of the black hole potential w.r.t R,

$$\frac{\partial \Phi_{\rm BH}}{\partial R} = 4\pi G\rho_0 a\frac{\mu_{\rm BH} R}{r^3}, \tag{5.13}$$

in eq. 5.7 we obtain the angular velocity squared of the torus due to the gravitational force of the black hole

$$\Omega^2_{BH}(R,z) = \frac{8\pi G\rho_0 a^2}{(\alpha+1)}\frac{\mu_{\rm BH}}{R^2 r}, \tag{5.14}$$

and thus the azimuthal velocity squared

$$v^2_{\phi,BH}(r) = \frac{8\pi G\rho_0 a^2}{(\alpha+1)}\frac{\mu_{\rm BH}}{r}. \tag{5.15}$$

The rotation velocity field of the system is Keplerian, $v^2_\phi \propto 1/r$, for every value of α.

Finally we compute the contribute to the temperature given by the black hole using the equation of state (eq. 4.14). Replacing P with P_{BH}, we obtain

$$T_{BH}(r) = 4\pi G\rho_0 a^2 \mu m_{\rm p} k_B^{-1}\frac{\mu_{\rm BH}}{(\alpha+1)r}. \tag{5.16}$$

The temperature and rotational velocity distributions are spherically symmetric, thus the surfaces of equal velocity and temperature are spheres.

5.4 Power-law tori in equilibrium in the gravitational potential of both gas and black hole, $\Phi_{\rm tot} = \Phi_{\rm BH} + \Phi$

We are ready to consider the systems under the influence of the total gravitational potential composed of the sum of the torus potential Φ, and the black hole potential $\Phi_{\rm BH}$,

$$\Phi_{\rm tot} = \Phi_{\rm BH} + \Phi. \tag{5.17}$$

The physical properties are obtained by adding the terms obtained for $\Phi_{\rm tot} = \Phi_{\rm BH}$ and $\Phi_{\rm tot} = \Phi$. We can do this for the linearity of the fluid-dynamics stationary equations (see sec. 5.2).

As we noted above, despite the expression of the gravitational potential is different for $\alpha = 4$ and $\alpha \neq 4$, the physical properties obtained for $\alpha \neq 4$ reduce to those with $\alpha = 4$ substituting the value 4 on α. Therefore, we use equations 4.19 and 4.22-4.24 both for $\alpha \neq 4$ and for $\alpha = 4$ because they hold for the two cases. Thus, for α in the range $2 < \alpha < 5$, the pressure, angular velocity, rotation velocity and temperature fields in the total gravitational potential are given, respectively, by

$$P(R,z) = \Phi_0\rho_0 R^2\frac{2\mu_{\rm BH}r^{\alpha-3} + f(\alpha)^{-1}\left[g(\alpha)R^2 + 4(\alpha-1)z^2\right]}{2(\alpha+1)r^{2(\alpha-1)}}, \tag{5.18}$$

$$\Omega^2(R,z) = 2\Phi_0 \frac{\mu_{\rm BH} r^{\alpha-3} + f(\alpha)^{-1}\big[(8-\alpha(5-\alpha))R^2 + 4(\alpha-1)z^2\big]}{(\alpha+1)R^2 r^{\alpha-2}}, \tag{5.19}$$

$$v_\phi^2(R,z) = 2\Phi_0 \frac{\mu_{\rm BH} r^{\alpha-3} + f(\alpha)^{-1}\big[(8-\alpha(5-\alpha))R^2 + 4(\alpha-1)z^2\big]}{(\alpha+1) r^{\alpha-2}}, \tag{5.20}$$

and

$$T(R,z) = \Phi_0 \rho_0 \mu m_{\rm p} k_{\rm B}^{-1} \frac{2\mu_{\rm BH} r^{\alpha-3} + f(\alpha)^{-1}\big[g(\alpha)R^2 + 4(\alpha-1)z^2\big]}{2(\alpha+1) r^{\alpha-2}}, \tag{5.21}$$

where we have defined $f(\alpha) \equiv (7-\alpha)(5-\alpha)(\alpha-2)^2$ and $g(\alpha) \equiv 16+\alpha(5-\alpha)(\alpha-4)$.

The effects of the black hole are tuned by its mass, thus by the parameter $\mu_{\rm BH}$. We can see it by studying the limit cases of these equations. At fixed distance, if $\mu_{\rm BH} \ll 1$, the equations become the same for the self-gravitating case (chapter 3), whereas if $\mu_{\rm BH} \gg 1$ the effect of the black hole is dominant and the equations become those of sec. 5.3, where only the black hole potential is present. This is expected, because considering the total potential $\Phi_{\rm tot} = \Phi + \Phi_{\rm BH}$, in the former case we have $|\Phi| \gg |\Phi_{\rm BH}|$, whereas in the latter $|\Phi_{\rm BH}| \ll |\Phi|$.

Consider now the radial distance from the center and thus from the black hole. A generic quantity q, such as the squared rotational velocity and the temperature, is due to the sum of the two contributes $q = q_{\rm BH} + q_{\rm self}$. The two terms depend on the radial distance with these trends:

$$q_{\rm BH} \propto \frac{1}{r},$$
$$q_{\rm self} \propto \frac{AR^2 + Bz^2}{r^{\alpha-2}} \propto \frac{1}{r^{\alpha-4}}.$$

For every value of α in the range $2 < \alpha < 5$, in the limit $r \ll 1$, $q_{\rm BH}$ is dominant and the equations reduce to those of sec. 5.3, where there are only the effects of the black hole potential. Whereas for high distances from the center $r \gg 1$, the term $q_{\rm BH}$ due to the black hole is negligible and the equations reduce to those of the self-gravitating case only.

Figs. 5.2 and 5.3 show the rotational velocity and temperature profiles in the equatorial plane for power-law tori with $\alpha = 2.1$, $\alpha = 3$, $\alpha = 4$, $\alpha = 4.5$, and $\alpha = 4.9$ without a black hole ($\mu_{\rm BH} = 0$), and for different values of black hole masses, $\mu_{\rm BH} = 1$, $\mu_{\rm BH} = 10$, and $\mu_{\rm BH} = 100$. For the cases with $\alpha < 4$, where in absence of the black hole the rotational velocity and the temperature increase with the distance, the black hole reverses this trend near the center and the effects are stronger with the increase of the black hole mass. The squared rotational velocity and the temperature decrease with the distance with a Keplerian slope $\propto 1/r$. The region with the Keplerian slope is larger and its normalization is higher for larger values of $\mu_{\rm BH}$. This holds also for $\alpha = 4$, where the rotational velocity and the temperature profiles in the equatorial plane in absence of the black hole

and outside the black hole influence (for $\mu_{\rm BH} > 0$) are constant. For $\alpha > 4$ the rotational velocity and temperature decrease with R both without and with a central black hole. The normalizations of the profiles are higher for larger values of $\mu_{\rm BH}$. The rotational velocity and the temperature distributions of the torus with $\alpha = 4.9$ near the upper limit are little affected for $\mu_{\rm BH} \lesssim 1$. The temperature distribution of the torus with $\alpha = 2.1$ near the lower limit of the range of α is little affected for $\mu_{\rm BH} \lesssim 1$.

Figs. 5.4-5.7 show the rotational velocity and the temperature maps for power-law tori with $\alpha = 2.1$, $\alpha = 3$, $\alpha = 4$ and $\alpha = 4.5$ for different values of $\mu_{\rm BH}$. For small values of black hole masses we note that at large distances from the center, the contours tend to those of the self-gravitating case. Close to the center the contours are modified and are rounder as those due to the black hole gravitational force only. For the torus with $\alpha = 2.1$, the influence of the black hole is apparent only for $\mu_{\rm BH} \gtrsim 10^2$ (fig. 5.4). The torus with $\alpha = 3$ (fig. 5.5) shows the presence of spots horizontally symmetric and rounder in the rotational velocity map (middle left panels) and vertical and more irregular in the temperature distribution (middle right panels). In this case with $\mu_{\rm BH} = 100$ the black hole is almost dominant in the region considered in the figure (bottom panels). The contours of the torus with $\alpha = 4$ (fig. 5.6) are already modified close to the center for small values of black hole masses (upper panels). The contours transform from a conical to a peanut shape (middle panels). In this case for $\mu_{\rm BH} = 10$ (lower panels) the black hole is already dominant in the region considered in figure, the contours are ellipsoid near circular, flattened horizontally in the rotational velocity maps and vertically in the temperature map. The contours of equal temperature and rotational velocity of the tori with $\alpha = 4.5$ (fig. 5.7) are rounder with the presence of the black hole with $\mu_{\rm BH} = 1$ (middle panels) and are nearly circular for $\mu_{\rm BH} = 10$ (lower panels), for larger values of $\mu_{\rm BH}$ are circular (not shown in the figure). The contours of equal temperature and rotational velocity of the torus with $\alpha = 4.9$, not shown in the figure, are circular both in the absence and in the presence of a central black hole.

5.5 Examples in physical units: molecular tori with central black hole

In this section we present examples in physical units of power-law tori in the presence of a central black hole. As in sections 3.6 and 4.3 we take as reference the AGN molecular tori, with the characteristics observed by Combes et al. (2019) and described in sec. 1.1. First, we note that substituting the reference scale and density, $a = 10$ pc and $n_0 = 10^4$ cm^{-3} (used also in sec. 3.6 and 4.3) in the expression of the parameter $\mu_{\rm BH}$, and considering, for example, a black hole of mass $M_{\rm BH} = 2 \times 10^7\ M_\odot$, we obtain $\mu_{\rm BH} = 3.26$. Therefore the gas self-gravity

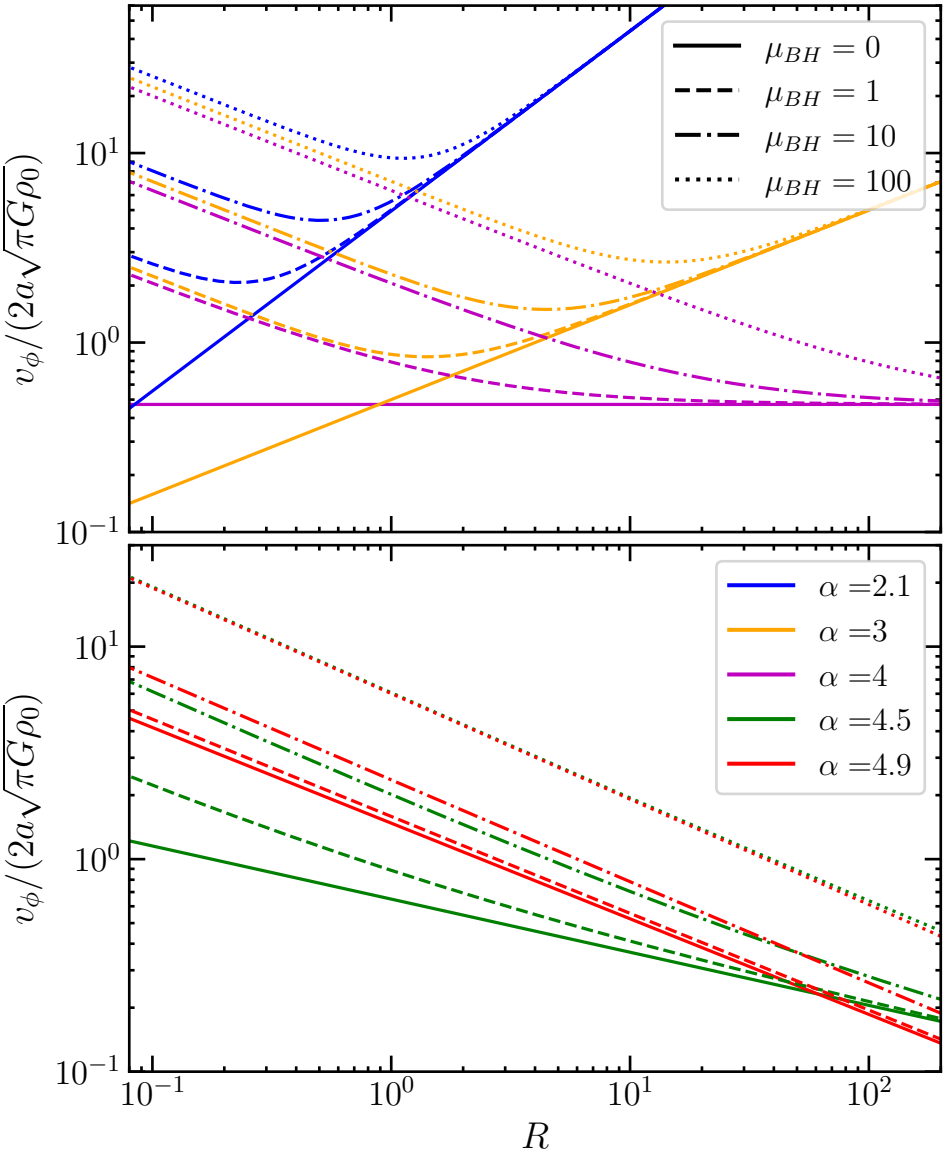

Figure 5.2: Rotational velocity profiles in the equatorial plane for power-law tori with $\alpha = 2.1$, $\alpha = 3$, $\alpha = 4$ (top), $\alpha = 4.5$ and $\alpha = 4.9$ (bottom) with $\mu_{\rm BH} = 0$ (solid line), $\mu_{\rm BH} = 1$ (dashed line), $\mu_{\rm BH} = 10$ (dash-dotted line) and $\mu_{\rm BH} = 100$ (dotted line). The profiles with $\mu_{\rm BH} = 100$ for the tori with $\alpha = 4.5$ and $\alpha = 4.9$ overlap.

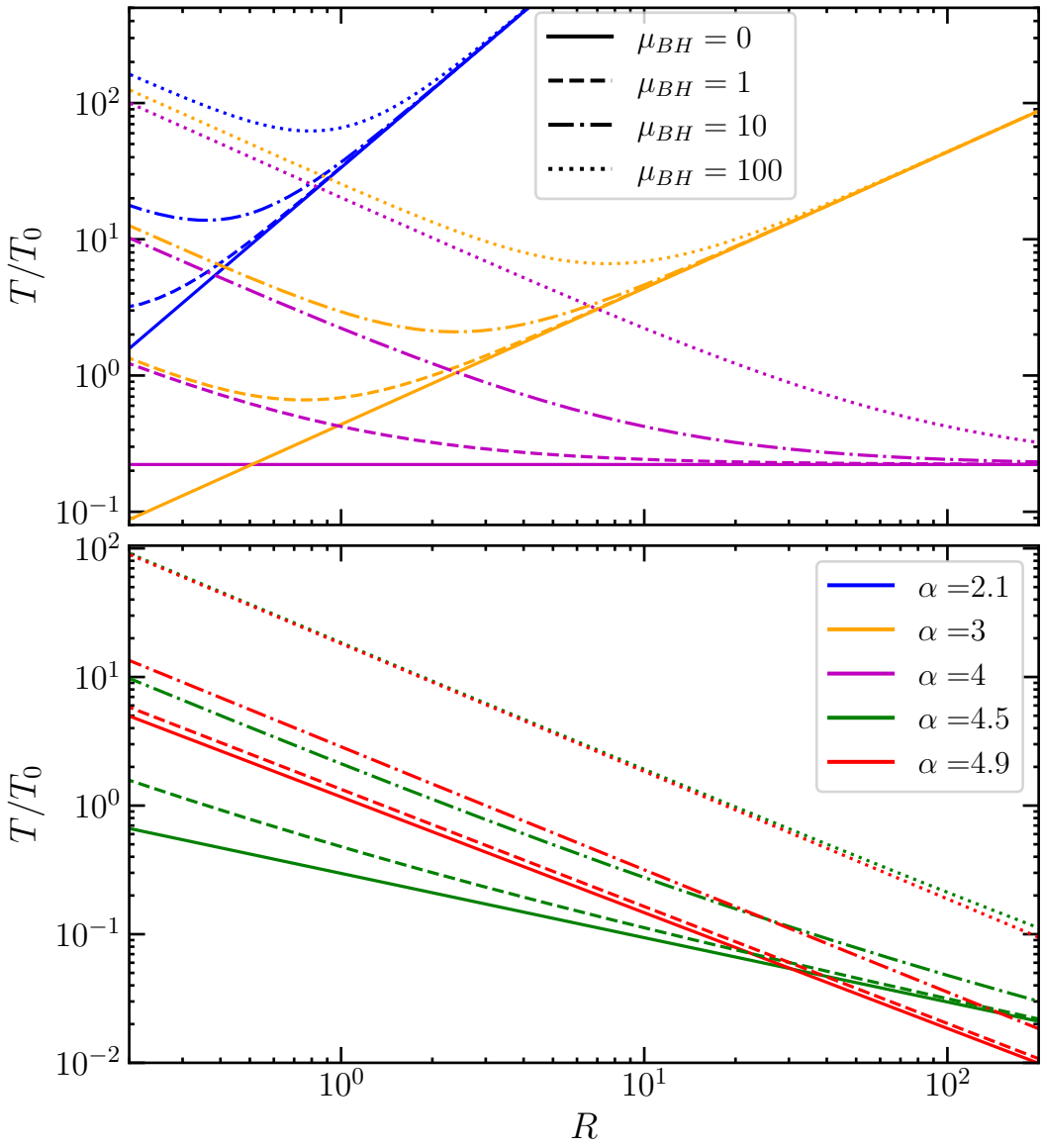

Figure 5.3: Temperature profiles in the equatorial plane for power-law tori with $\alpha = 2.1$, $\alpha = 3$, $\alpha = 4$ (top), $\alpha = 4.5$ and $\alpha = 4.9$ (bottom) with $\mu_{\rm BH} = 0$ (solid line), $\mu_{\rm BH} = 1$ (dashed line), $\mu_{\rm BH} = 10$ (dash-dotted line) and $\mu_{\rm BH} = 100$ (dotted line). The profiles with $\mu_{\rm BH} = 100$ for the tori with $\alpha = 4.5$ and $\alpha = 4.9$ overlap.

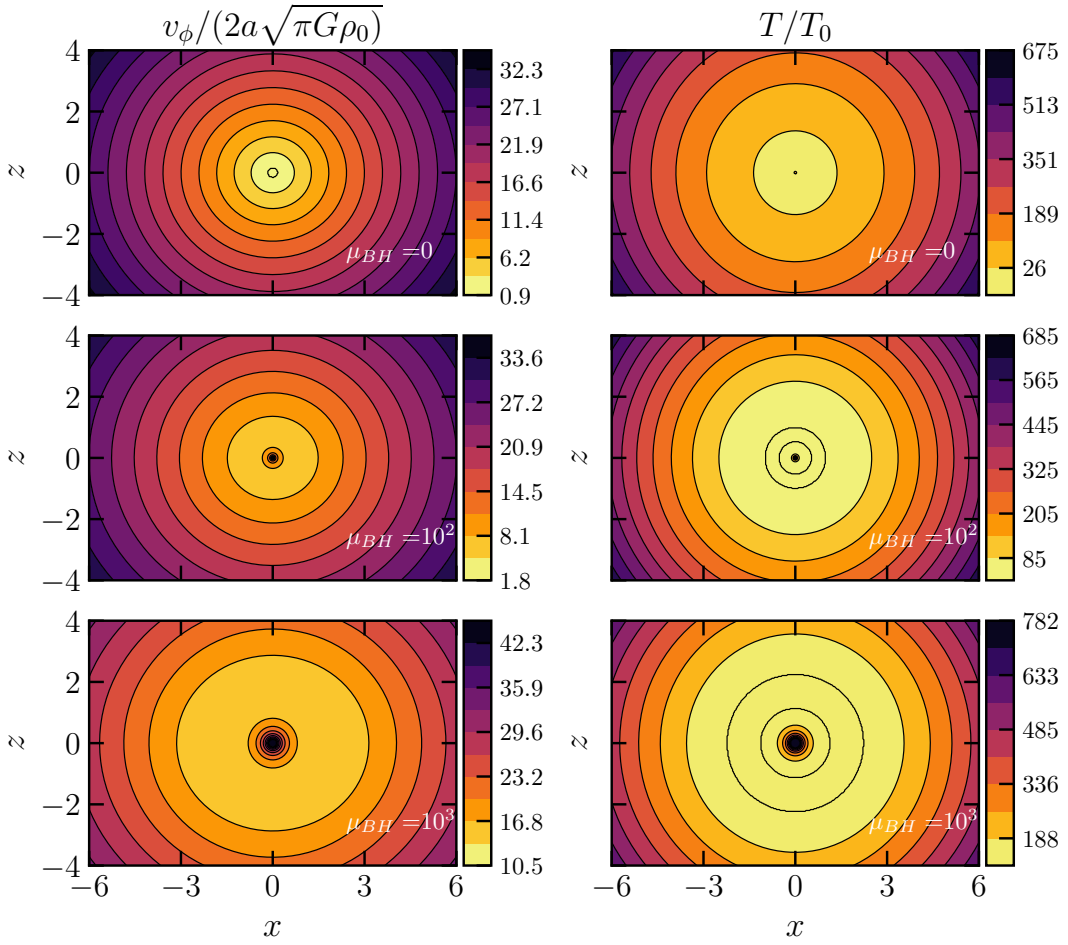

Figure 5.4: Rotational velocity maps (left panels) and temperature maps (right panels) for power-law torus with $\alpha = 2.1$, in a total potential $\Phi_{\rm tot} = \Phi + \Phi_{\rm BH}$ with $\mu_{\rm BH} = 0$ (top), $\mu_{\rm BH} = 100$ (middle), and $\mu_{\rm BH} = 1000$ (bottom).

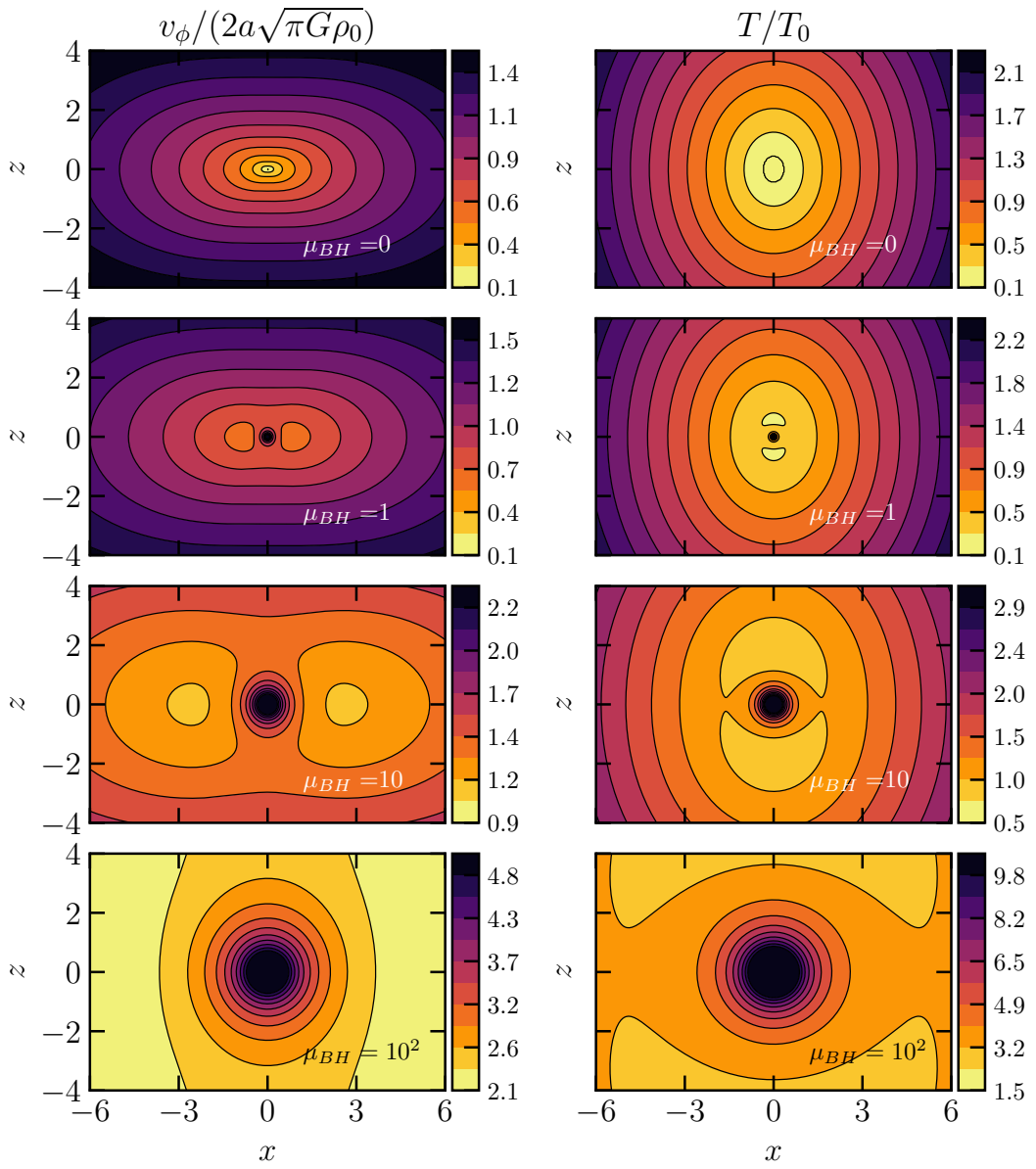

Figure 5.5: Rotational velocity maps (left panels) and temperature maps (right panels) for power-law torus with $\alpha = 3$, in a total potential $\Phi_{\rm tot} = \Phi + \Phi_{\rm BH}$ with $\mu_{\rm BH} = 0$, $\mu_{\rm BH} = 1$, $\mu_{\rm BH} = 10$, and $\mu_{\rm BH} = 100$ (from top to bottom).

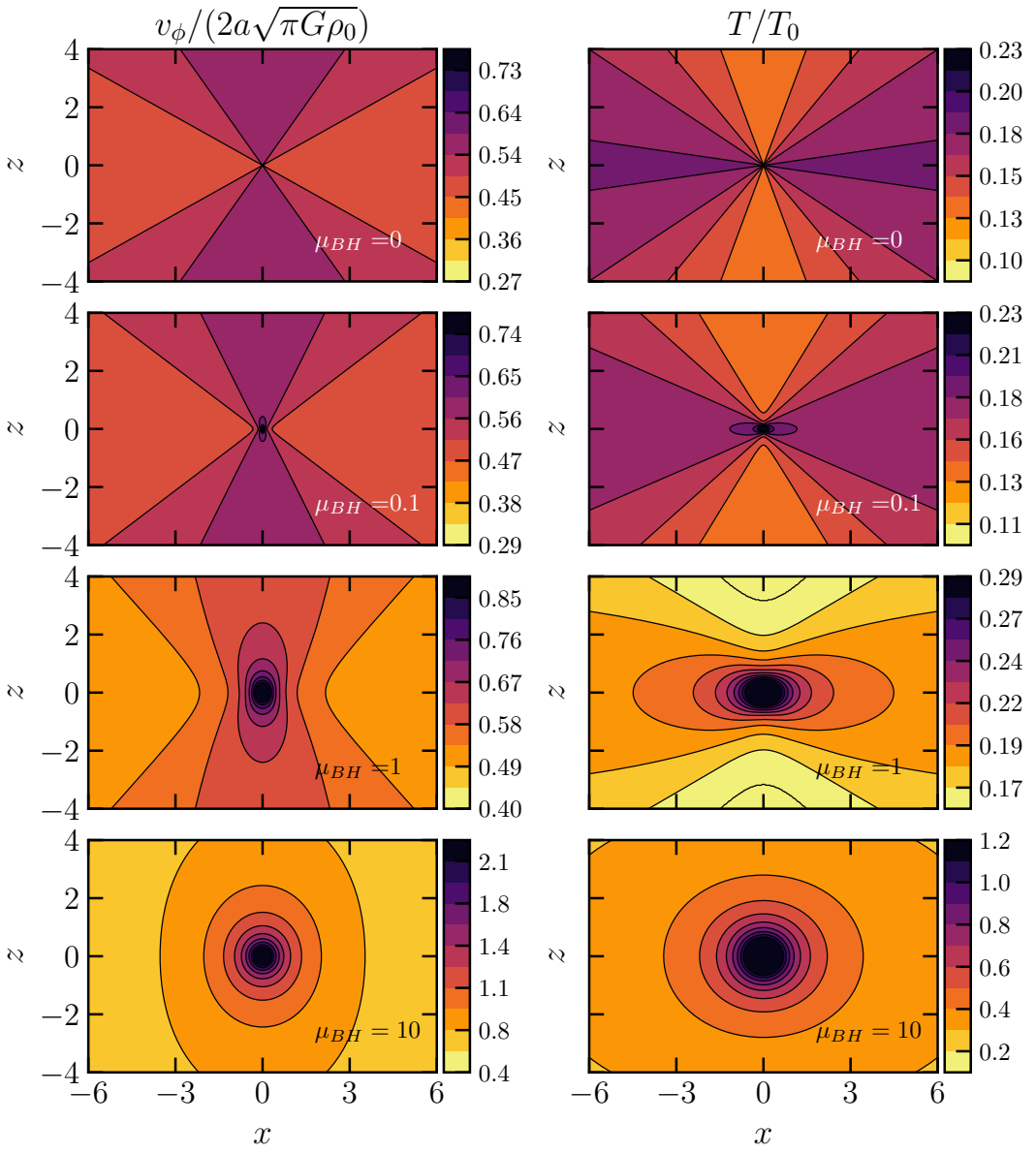

Figure 5.6: Rotational velocity maps (left panels) and temperature maps (right panels) maps for power-law torus with $\alpha = 4$, in a total potential $\Phi_{\rm tot} = \Phi + \Phi_{\rm BH}$ with $\mu_{\rm BH} = 0$, $\mu_{\rm BH} = 0.1$, $\mu_{\rm BH} = 1$, and $\mu_{\rm BH} = 10$ (from top to bottom).

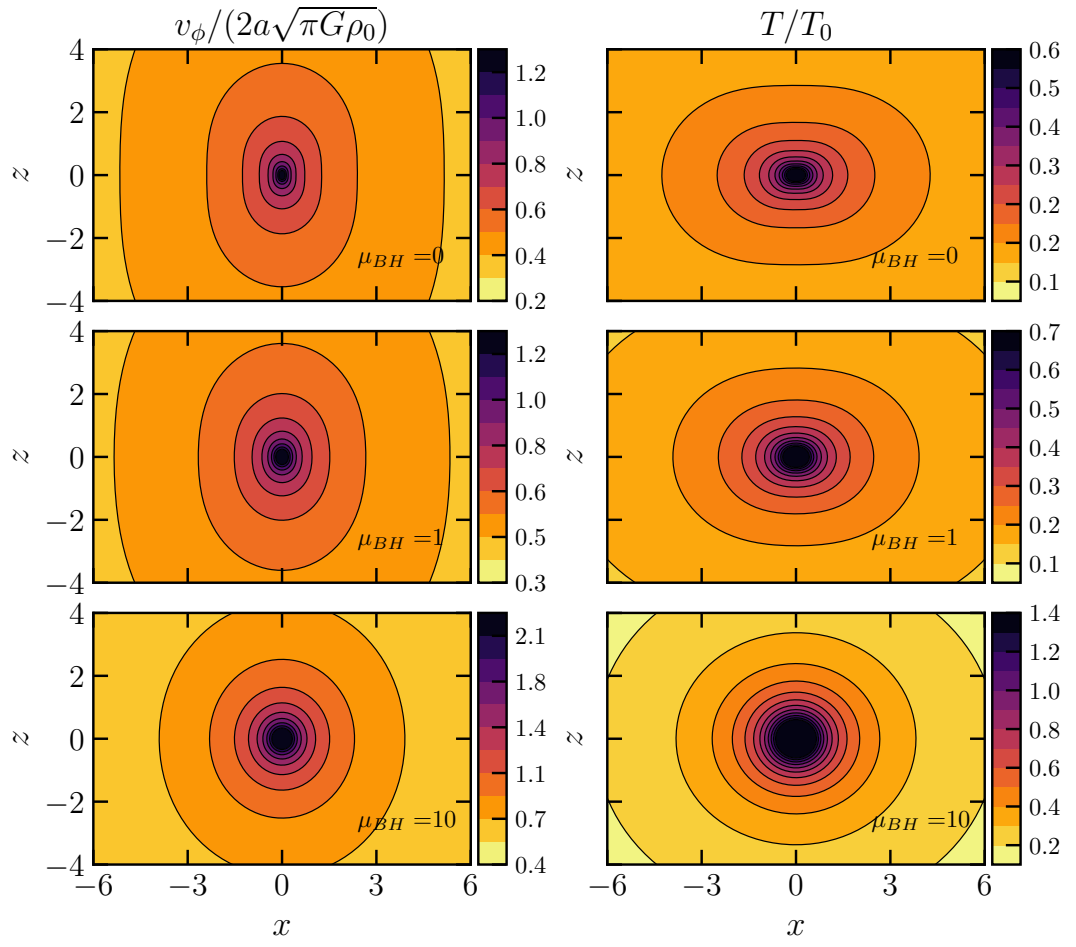

Figure 5.7: Rotational velocity maps (left panels) and temperature maps (right panels) maps for power-law torus with $\alpha = 4.5$, in a total potential $\Phi_{\rm tot} = \Phi + \Phi_{\rm BH}$ with $\mu_{\rm BH} = 0$ (top), $\mu_{\rm BH} = 1$ (middle), and $\mu_{\rm BH} = 10$ (bottom).

and the black hole gravitational field are comparable.

In equations 3.1 and 5.20 we substitute a reference scale of $a = 10$ pc and a reference density of $n_0 = 10^4$ cm^{-3} and consider $M_{\rm BH} = 2 \times 10^7\ M_\odot$. As done in section 4.3, we define the gas velocity dispersion as $\sigma_g = \sqrt{P/\rho}$. Figs.[1] 4.10-4.12 show the density, the gravitational potential, the velocity dispersion and the rotational velocity of the self-gravitating power-law tori without external potential, for $\alpha = 3$, $\alpha = 4$ and $\alpha = 4.5$, with a black hole of mass $2 \times 10^7\ M_\odot$. We note that velocity dispersion and rotational velocity are, as found also in sec. 4.3, of the same order of magnitude as those observed by Combes et al. (2019) and described in sec. 1.1. Considering the figures of sec. 4.3, we note that in general the effect of adding the black hole with $\mu_{\rm BH} = 3.26$ is to increase slightly σ_g and v_ϕ at given position. The morphology of the velocity maps are significantly different with and without the black hole.

[1] In the figures of this section, R, x, and z are not normalized to a, but are in physical units.

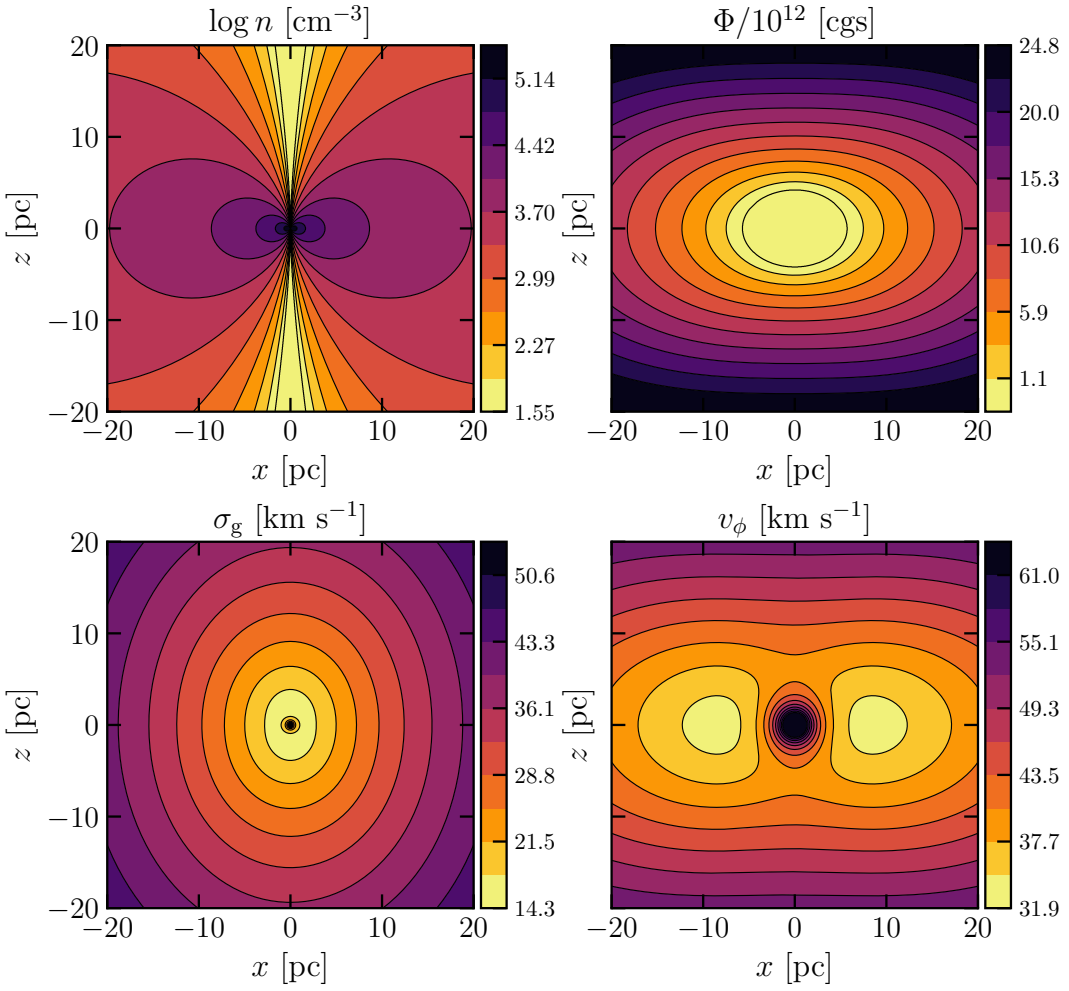

Figure 5.8: Top: density (left) and potential (right) maps for the self-gravitating power-law torus with $\alpha = 3$. Bottom: velocity dispersion (left) and rotational velocity (right) maps. The reference scale and density are $a = 10$ pc and $n_0 = 10^4$ cm^{-3}, respectively. The black hole has a mass $M_{\rm BH} = 2 \times 10^7\ M_\odot$.

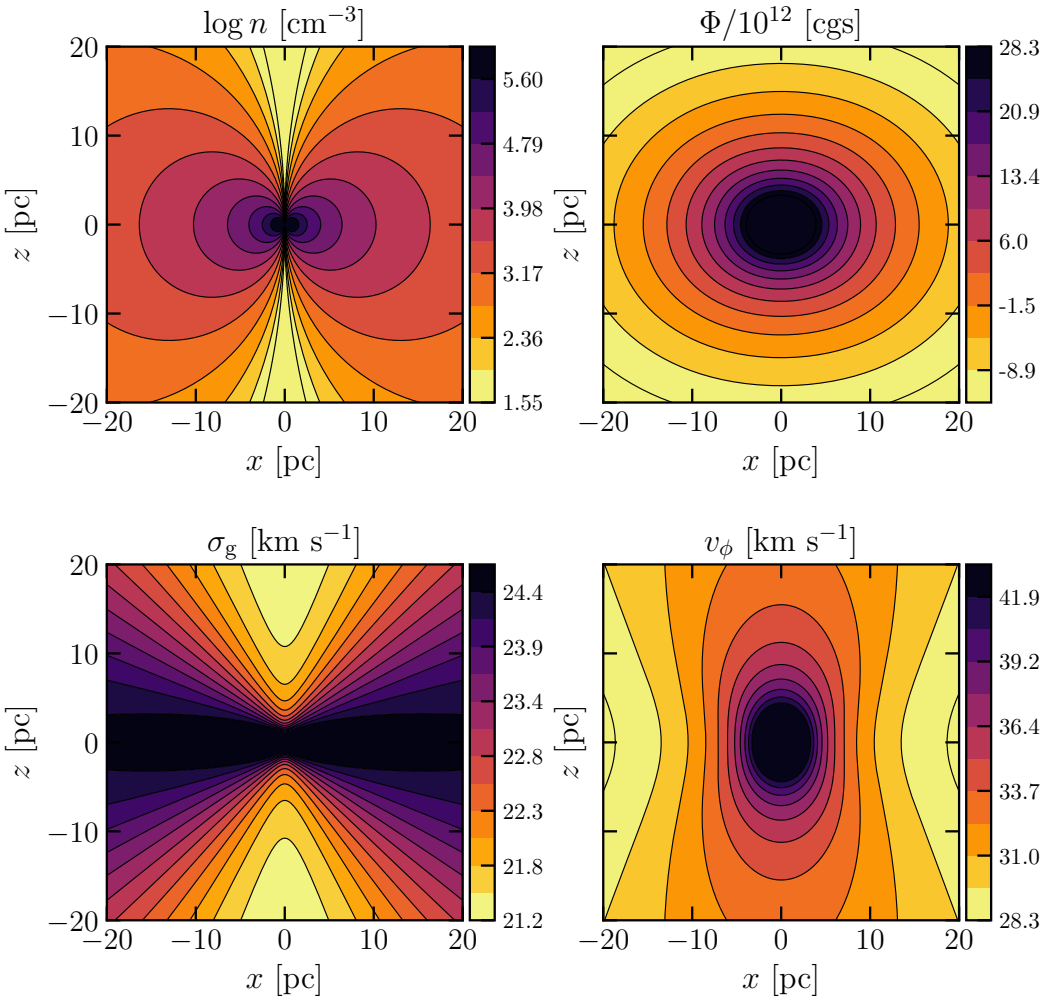

Figure 5.9: Top: density (left) and potential (right) maps for the self-gravitating power-law torus with $\alpha = 4$. Bottom: velocity dispersion (left) and rotational velocity (right) maps. The reference scale and density are $a = 10$ pc and $n_0 = 10^4$ cm^{-3}, respectively. The black hole has a mass $M_{\rm BH} = 2 \times 10^7$ $M_\odot$.

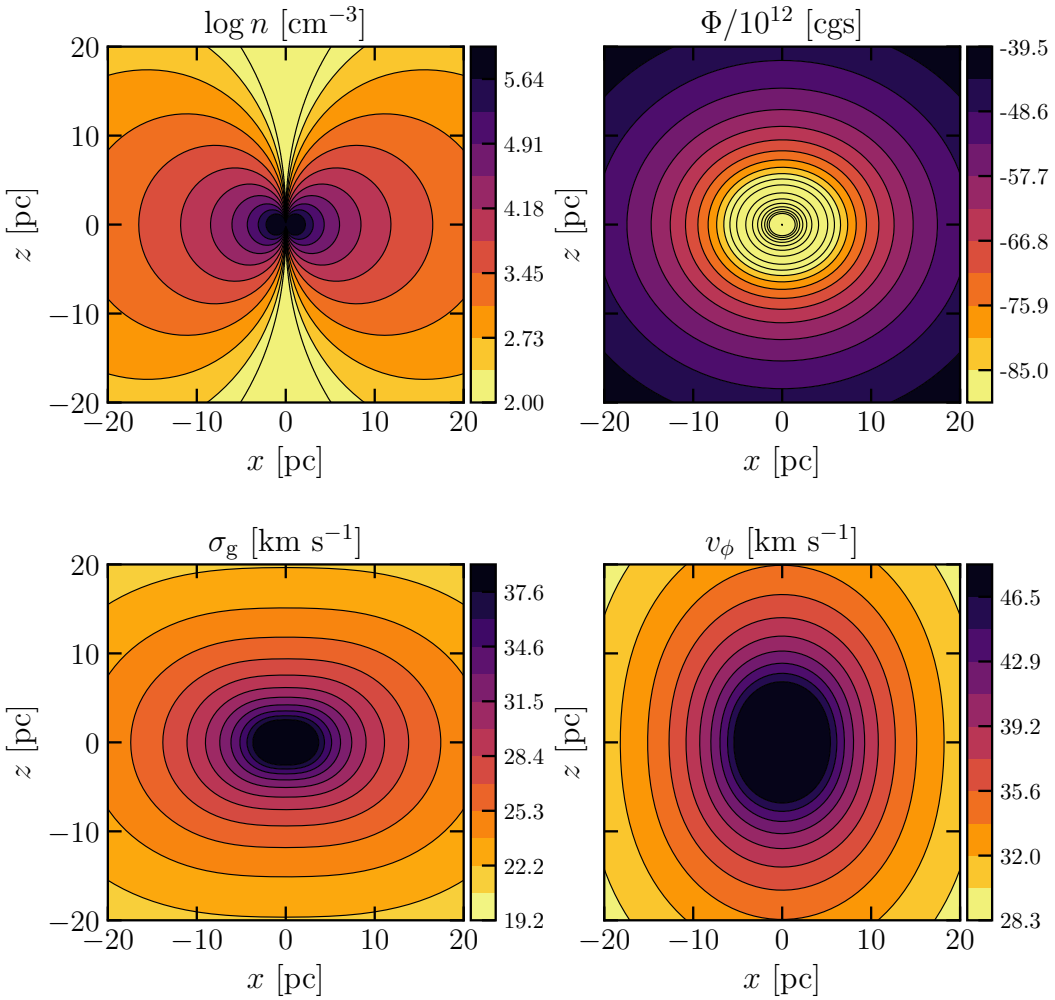

Figure 5.10: Top: density (left) and potential (right) maps for the self-gravitating power-law torus with $\alpha = 4.5$. Bottom: velocity dispersion (left) and rotational velocity (right) maps. The reference scale and density are $a = 10$ pc and $n_0 = 10^4$ cm^{-3}, respectively. The black hole has a mass $M_{\rm BH} = 2 \times 10^7\ M_\odot$.

Chapter 6

Stability

In this chapter we study the stability of the models for different equilibrium configurations. First, we study the stability of the power-law tori in equilibrium in their self-gravity (sec. 6.1), then when the power-law tori are in equilibrium with only the gravitational force of the central black hole (sec. 6.2) and, finally, in the case that the power-law tori are under the force of their self-gravity and the black hole potential (sec. 6.3).

Here we consider the case in which the fluid consists of an ideal gas with adiabatic index γ. We study the stability trough the application of the Solberg-Høiland criterion (see sec. 2.4). From the requirement that $\omega^2 > 0$ (eq. 2.44), one obtains the conditions for stability

$$\frac{1}{\gamma\rho}\left(\frac{\partial P}{\partial R}\frac{\partial \sigma}{\partial R}+\frac{\partial P}{\partial z}\frac{\partial \sigma}{\partial z}\right)-\frac{1}{R^3}\frac{\partial \Omega^2 R^4}{\partial R}<0 \tag{6.1}$$

and

$$\frac{\partial P}{\partial z}\left[\frac{\partial \Omega^2 R^4}{\partial R}\frac{\partial \sigma}{\partial z}-\frac{\partial \Omega^2 R^4}{\partial z}\frac{\partial \sigma}{\partial R}\right]<0. \tag{6.2}$$

In the stability conditions the pressure P, squared angular momentum $\Omega^2 R^4$, and the entropy σ gradients are present. We have already obtained the pressure P and the angular velocity Ω for all the systems, thus we have to evaluate the normalized entropy σ, which depends on the adiabatic index of the gas γ (see eq. 2.25). We focus on the biatomic $\gamma = 7/5 = 1.4$ and monoatomic adiabatic index $\gamma = 5/3 \simeq 1.67$.

With A_i we denote polynomials of α, which appear in the inequalities 6.1 and 6.2. The coefficients of the polynomials depend on γ, so A_i are functions of α and γ. The polynomials A_i for $i = 1, ..., 29$ are listed in Appendix A and, except for those for which we can analytically check the sign, are plotted for α in the range $2 < \alpha < 5$, and for $\gamma = 7/5$ and $\gamma = 5/3$, to study graphically the sign (figs. A.1-A.4). All these polynomials are positive in the range of α and for the values of γ considered. Once the values of α and γ are fixed, i.e. the model is specified, the polynomials A_i are just numerical constants.

6.1 Stability of self-gravitating power-law tori in the absence of the central black hole

The normalized entropy distribution of the systems, defined as

$$\sigma \equiv \ln \frac{P}{\rho^{\gamma}}, \tag{6.3}$$

for $2 < \alpha < 5$, is

$$\sigma = \ln \left[\frac{g(\alpha) R^2 + 4(\alpha - 1) z^2}{2(\alpha - 1) f(\alpha) R^{2(\gamma - 1)} r^{\alpha(2-\gamma)-2}} \right]. \tag{6.4}$$

The constants have been included in the additive constant of the entropy. Fig. 6.1 shows the radial profiles of the entropy for the monoatomic and biatomic adiabatic index. The profiles increase outward for all the α, the increase is stronger for lower values of α. The increase of the adiabatic index, passing from a biatomic to a monoatomic gas, makes the increase of the profiles stronger, especially for larger value of α. As seen in sec. 2.4, the Solberg-Høiland criterion are a generalization of the Schwarzschild convective instability criterion and the Rayleigh rotational instability criterion. For the convective instability criterion, in a system where the pressure decreases outward, the outward increase of the entropy is required for the stability. The figure 6.2 shows the isoentropy contours of the tori with $\alpha = 2.1$, $\alpha = 3$, $\alpha = 4$ and $\alpha = 4.9$. The contours are elongated along the z axis for small values of α, and they are elongated along the R axis for high values of α. The entropy increases faster vertically than radially. Considering that the pressure decreases moving away from the equatorial plane, so $\partial P / \partial z$ is negative when $z > 0$, this entropy gradient helps the stability of the system, looking at eq. 6.2.

Fig. 6.3 shows the angular momentum squared profiles in the equatorial plane for different values of α. For every value of α, the angular momentum squared increases with R in the equatorial plane, with a slope steeper for lower values of α. The Rayleigh instability criterion requires that the angular momentum squared has to increase outward for the stability.

Now we apply the Solberg-Høiland criterion to the self-gravitating case without the presence of the central black hole. Substituting the radial (eq. 4.20) and the vertical partial derivatives of the pressure, of the entropy, and the radial partial derivative of the angular momentum, in the first inequality of the Solberg-Høiland criterion (eq. 6.1), we obtain, after some algebra, the condition for stability

$$\frac{A_1 R^6 + A_2 R^4 z^2 + A_3 R^2 z^4 + A_4 z^6}{\gamma R^2 (\alpha - 1) f(\alpha) \left[g(\alpha) R^2 + 4(\alpha - 1) z^2 \right] r^{\alpha}} > 0, \tag{6.5}$$

The functions $f(\alpha) = (\alpha - 2)^2 (7 - \alpha)(5 - \alpha)$ and $g(\alpha) = 16 + \alpha(5 - \alpha)(\alpha - 4)$, at the denominator of eq. 6.5, are positive in the range $2 < \alpha < 5$: for the former

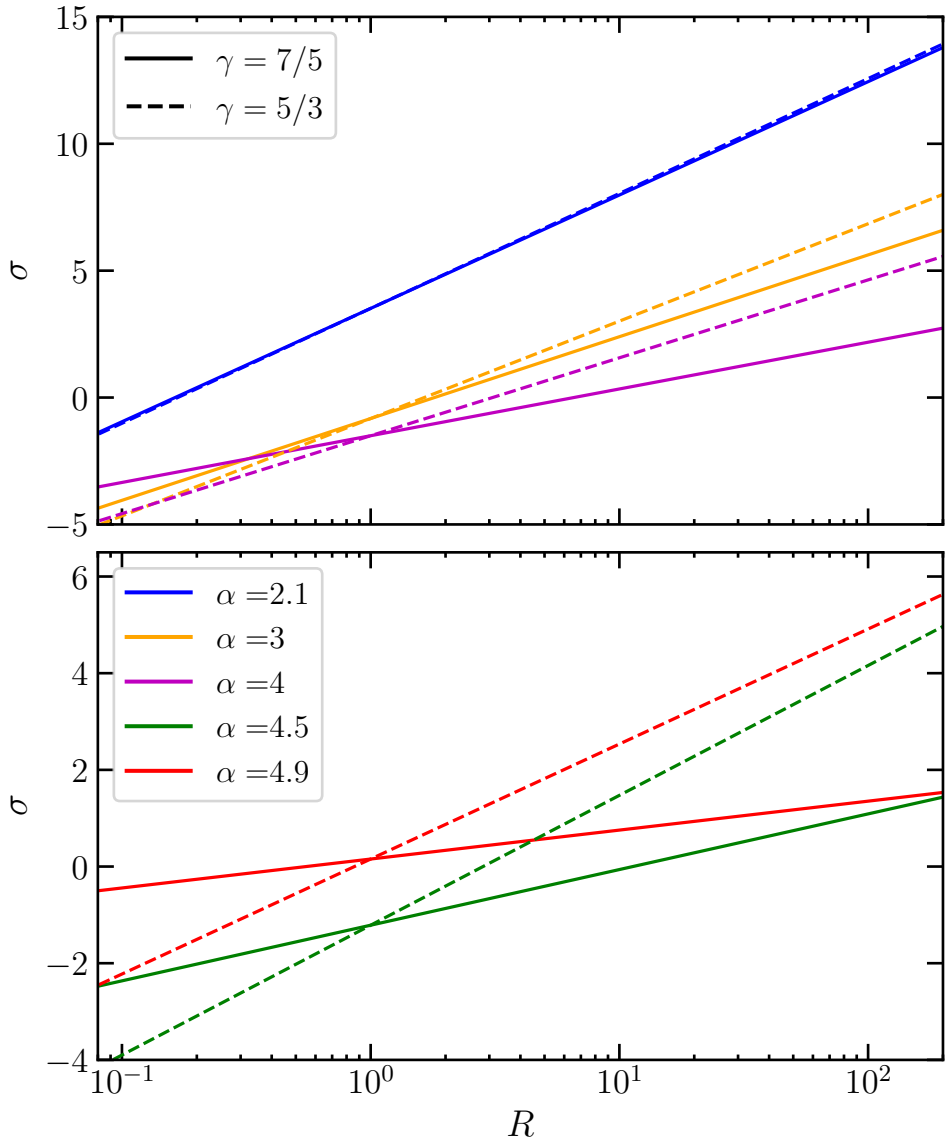

Figure 6.1: Radial entropy profiles for self-gravitating power-law tori without central black hole with $\alpha = 2.1$, $\alpha = 3$, $\alpha = 4$ (top) , $\alpha = 4.5$ and $\alpha = 4.9$ (bottom), for the monoatomic $\gamma = 5/3$ (solid line) and the biatomic adiabatic index $\gamma = 7/5$ (dashed line). The $\alpha = 2.1$ entropy profiles overlap for $\gamma = 7/5$ and $\gamma = 5/3$.

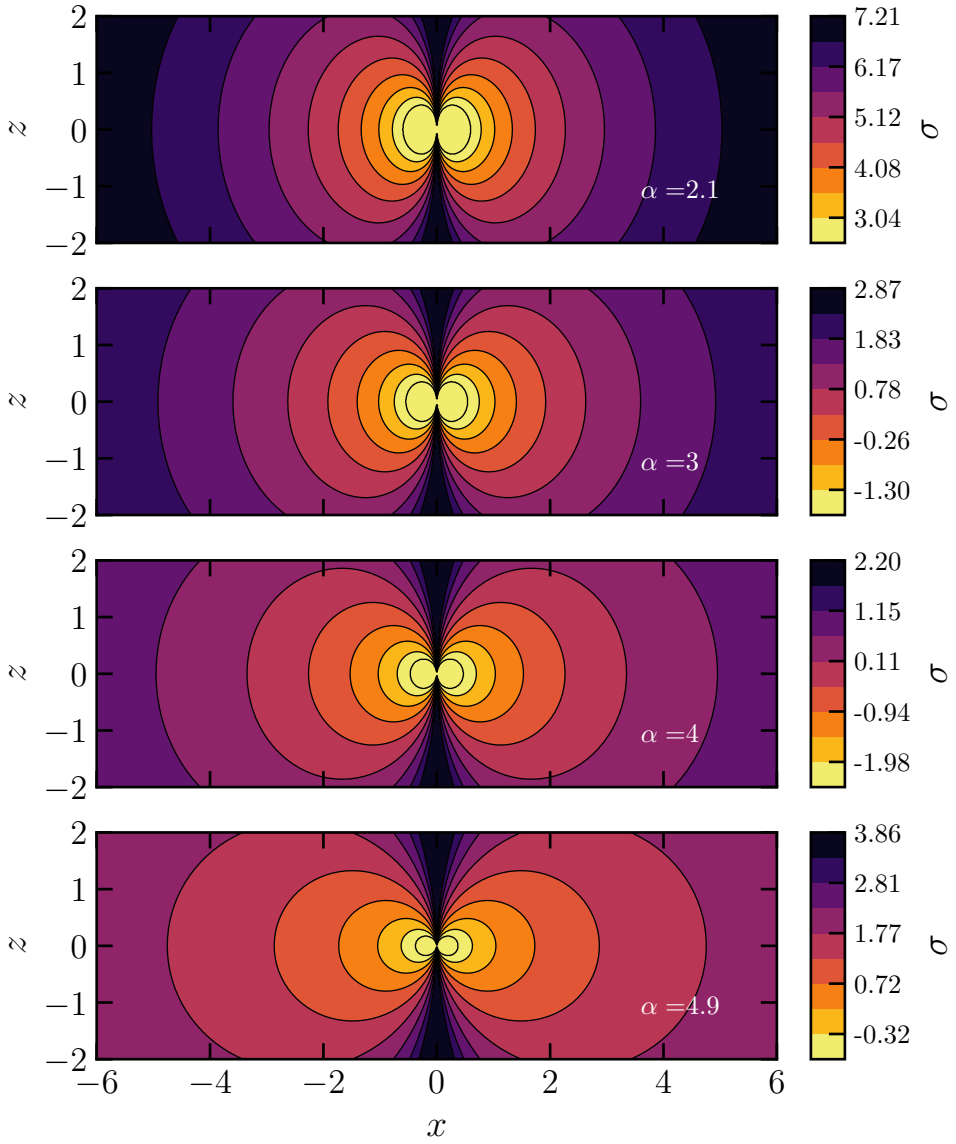

Figure 6.2: Entropy map in the meridional plane for self-gravitating power-law tori without the central black hole with $\alpha = 2.1$, $\alpha = 3$, $\alpha = 4$ and $\alpha = 4.9$ (from top to bottom), for a monoatomic adiabatic index $\gamma = 5/3$.

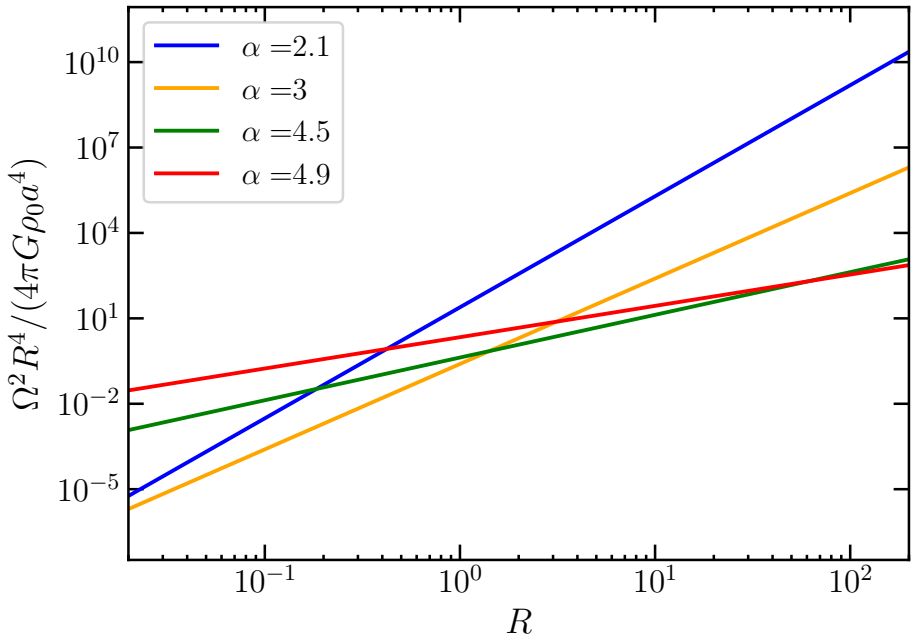

Figure 6.3: Radial angular momentum squared profiles for self-gravitating power-law tori without central black hole with $\alpha = 2.1$, $\alpha = 3$, $\alpha = 4$, $\alpha = 4.5$ and $\alpha = 4.9$.

is easily checked, the latter is shown graphically in fig. A.1 (left upper panel) in the Appendix A. The R and r coordinates are positive defined and z is squared at the denominator, thus the denominator of eq. 6.5 is positive. The coefficients A_1-A_4 of the coordinates that appear at the numerator of eq. 6.5, functions of α and γ, are positive for the (α,γ) of interest as shown in the appendix A. Since all the coefficients A_i for $i = 1, .., 4$ are positive for every value of α in the range $2 < \alpha < 5$ and the γ considered, and the powers of z are all even, the numerator is also positive. Therefore the first inequality is verified everywhere, for every value of α in the range $2 < \alpha < 5$, both for monoatomic and biatomic gas.

Substituting the vertical partial derivative of the pressure, the radial and vertical partial derivative of the entropy, and of the angular momentum, in the second inequality of the criterion (eq. 6.2), we obtain the other condition for stability

$$4R^3z^2\frac{\big(h(\alpha)R^2+4z^2\big)\big(A_5R^4+A_6R^2z^2+A_7z^4\big)}{(\alpha-1)(\alpha-2)f(\alpha)^2\big[g(\alpha)R^2+4(\alpha-1)z^2\big]r^{3\alpha}}>0 \tag{6.6}$$

with $h(\alpha) = -\alpha^2+7\alpha-6$. For the considerations reported above, the denominator of eq. 6.6 is positive. The term in the first parenthesis at the numerator of eq. 6.6 is positive since $h(\alpha)$ is positive for α in the range $2 < \alpha < 5$, as plotted in fig. A.1 (right upper panel) and z is squared. The coefficients A_5-A_7 in the term

in the second parenthesis at the numerator of eq. 6.6, which are functions of α and γ, are positive for the (α,γ) of interest, as shown in Appendix A. Since the powers of z are all even, the numerator is positive.

The second inequality of the criterion is verified everywhere except for $R = 0$ and $z = 0$, where it is not well defined. Along the z axis the density is null, so we do not care about the sign of eq. 6.6 for $R = 0$. To evaluate the stability criterion for $z = 0$ it is opportune to start directly from the relation dispersion (eq. 2.44). The squared angular frequency must be positive, so we obtain the condition for the stability

$$\frac{1}{\gamma\rho}\frac{\partial P}{\partial z}\frac{\partial \sigma}{\partial z}x^2+\left(\frac{1}{R^3}\frac{\partial \Omega^2 R^4}{\partial z}-\frac{1}{\gamma\rho}\left(\frac{\partial P}{\partial R}\frac{\partial \sigma}{\partial z}-\frac{\partial P}{\partial z}\frac{\partial \sigma}{\partial R}\right)\right)x+\frac{1}{\gamma\rho}\frac{\partial P}{\partial R}\frac{\partial \sigma}{\partial R}-\frac{1}{R^3}\frac{\partial \Omega^2 R^4}{\partial R}<0 \tag{6.7}$$

Because every vertical partial derivative evaluated at $z = 0$ is null, eq. 6.7 along the R axis is

$$\frac{1}{\gamma\rho}\left(\frac{\partial P}{\partial R}\frac{\partial \sigma}{\partial R}\right)\bigg|_{z=0}-\frac{1}{R^3}\frac{\partial \Omega^2 R^4}{\partial R}\bigg|_{z=0}<0. \tag{6.8}$$

Substituting the radial partial derivative of the pressure, of the entropy and of the squared angular momentum evaluated at $z = 0$ in eq. 6.8 we obtain the condition for stability

$$\frac{A_8}{\gamma(\alpha-1)f(\alpha)R^{\alpha-2}}>0. \tag{6.9}$$

This inequality is verified since the denominator is positive and the term A_8 is positive.

Therefore we have proved that the power-law tori in equilibrium in their gas self-gravity are linearly stable everywhere, for every value of α in the range $2 < \alpha < 5$, for the biatomic and monoatomic adiabatic index $\gamma = 7/5$ and $\gamma = 5/3$.

6.2 Stability of power-law tori in equilibrium in the black hole gravitational potential

In this section we apply the Solberg-Høiland criterion to the system composed by the power-law tori and the central black hole in equilibrium in the gravitational potential of the black hole only.

The normalized entropy for this is system is

$$\sigma_{\mathrm{BH}}=\ln\left(\mu_{\mathrm{BH}}\frac{r^{\alpha(\gamma-1)-1}R^{2(1-\gamma)}}{\alpha+1}\right). \tag{6.10}$$

The other constants are included in the additive constant of the entropy. Fig. 6.4 shows the radial profiles of the entropy for different values of α, for a monoatomic

and biatomic gas, for a black hole with $\mu_{\rm BH} = 1$. For lower values of α the entropy decreases with R, which, as we will see, causes instability. For larger values of α the entropy increases very slowly with α for a biatomic adiabatic index, while for a monoatomic gas the entropy increases stronger radially. In particular cases, e.g. for $\alpha = 4$ in figure, the increase of the adiabatic index changes the slope of the profile: the entropy for $\alpha = 4$ decreases with R for $\gamma = 7/5$ and increases with R for $\gamma = 5/3$.

Fig. 6.5 shows the entropy maps for different values of α, for $\gamma = 5/3$, for a black hole with $\mu_{\rm BH} = 1$. For larger values of α the contours remain almost the same compared to the systems entropy with self-gravity only, the shape is more flattened horizontally. For lower values of α the contours of equal entropy change the shape, which contributes to the instability for lower values of α. Since the velocity field in this case is Keplerian $v_\phi^2 \propto 1/r$, the angular momentum squared increases outward for every value of α.

Substituting the radial and vertical partial derivatives of the pressure

$$\frac{\partial P_{\rm BH}}{\partial R} = -4\pi G\rho_0^2 a\mu_{\rm BH} R\frac{(\alpha-1)R^2 - 2z^2}{(\alpha+1)r^{\alpha+3}}, \tag{6.11}$$

$$\frac{\partial P_{\rm BH}}{\partial z} = -4\pi G\rho_0^2 a\frac{\mu_{\rm BH} R^2 z}{r^{\alpha+3}}, \tag{6.12}$$

the radial and vertical partial derivatives of the normalized entropy

$$\frac{\partial \sigma_{\rm BH}}{\partial R} = -\frac{2(\gamma-1)}{R} - \frac{R((1-\gamma)\alpha+1)}{r^2}, \tag{6.13}$$

$$\frac{\partial \sigma_{\rm BH}}{\partial z} = -z\frac{(1-\gamma)\alpha+1}{r^2}, \tag{6.14}$$

and the radial partial derivative of the angular momentum squared

$$\frac{\partial \Omega_{\rm BH}^2 R^4}{\partial R} = 2\mu_{\rm BH} R\frac{R^2+2z^2}{(\alpha+1)r^3}, \tag{6.15}$$

in the first inequality of the Solberg-Høiland criterion (eq. 6.1), we obtain the first condition for stability

$$\mu_{\rm BH}\frac{A_9 R^2 + 4(2\gamma-1)z^2}{\gamma(\alpha+1)R^2 r^3} > 0. \tag{6.16}$$

The denominator of the fraction of eq. 6.16 is positive, the numerator is positive since the coefficient of z^2 is positive for the γ considered, and A_9 is positive for the values (α, γ) of interest as shown in Appendix A. Therefore, the inequality 6.16 is satisfied everywhere for every values of α in the range $2 < \alpha < 5$, for $\gamma = 7/5$ and $\gamma = 5/3$.

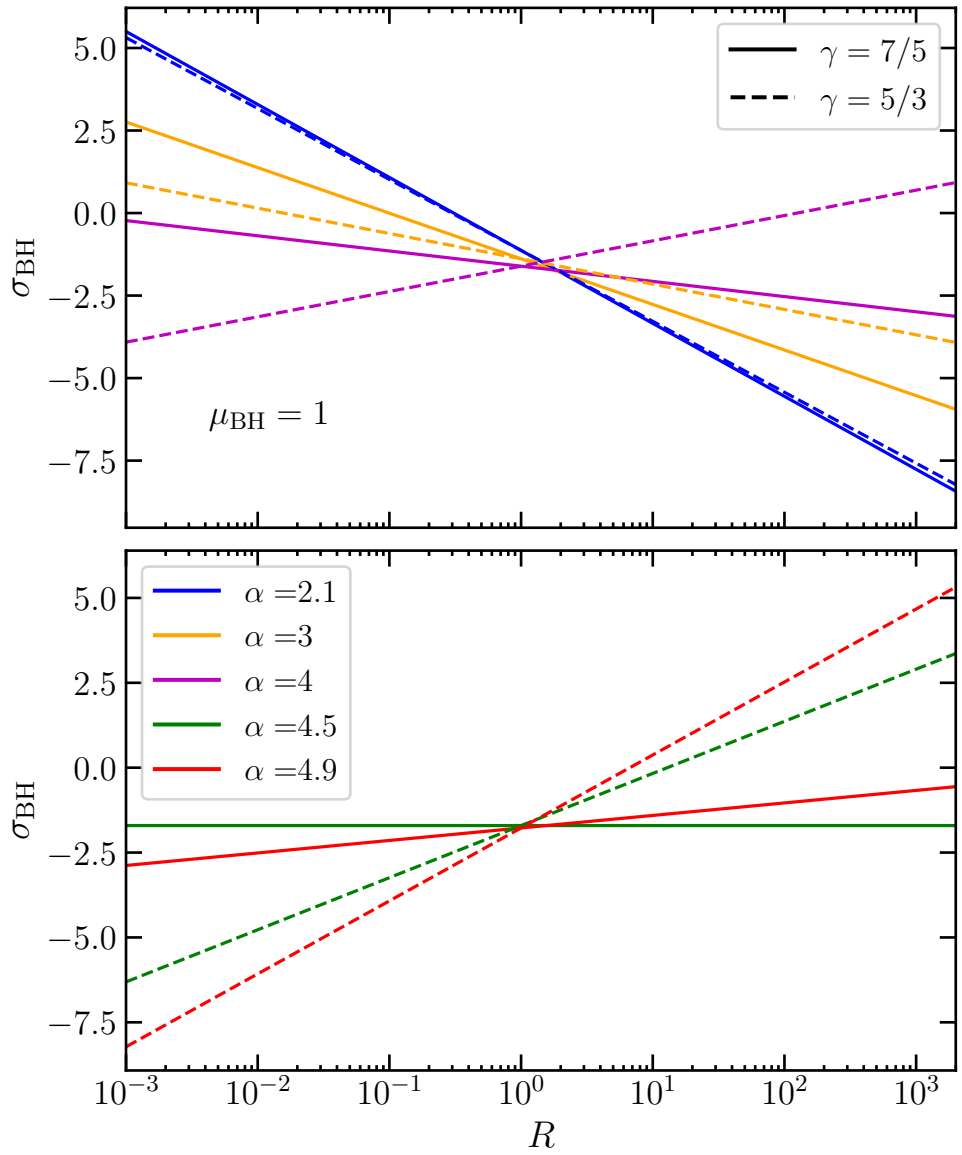

Figure 6.4: Radial entropy profiles for power-law tori in equilibrium in the black hole gravitational potential only, with $\alpha = 2.1$, $\alpha = 3$, $\alpha = 4$ (top) , $\alpha = 4.5$ and $\alpha = 4.9$ (bottom), for the monoatomic $\gamma = 5/3$ (solid line) and the biatomic adiabatic index $\gamma = 7/5$ (dashed line), with $\mu_{\rm BH} = 1$.

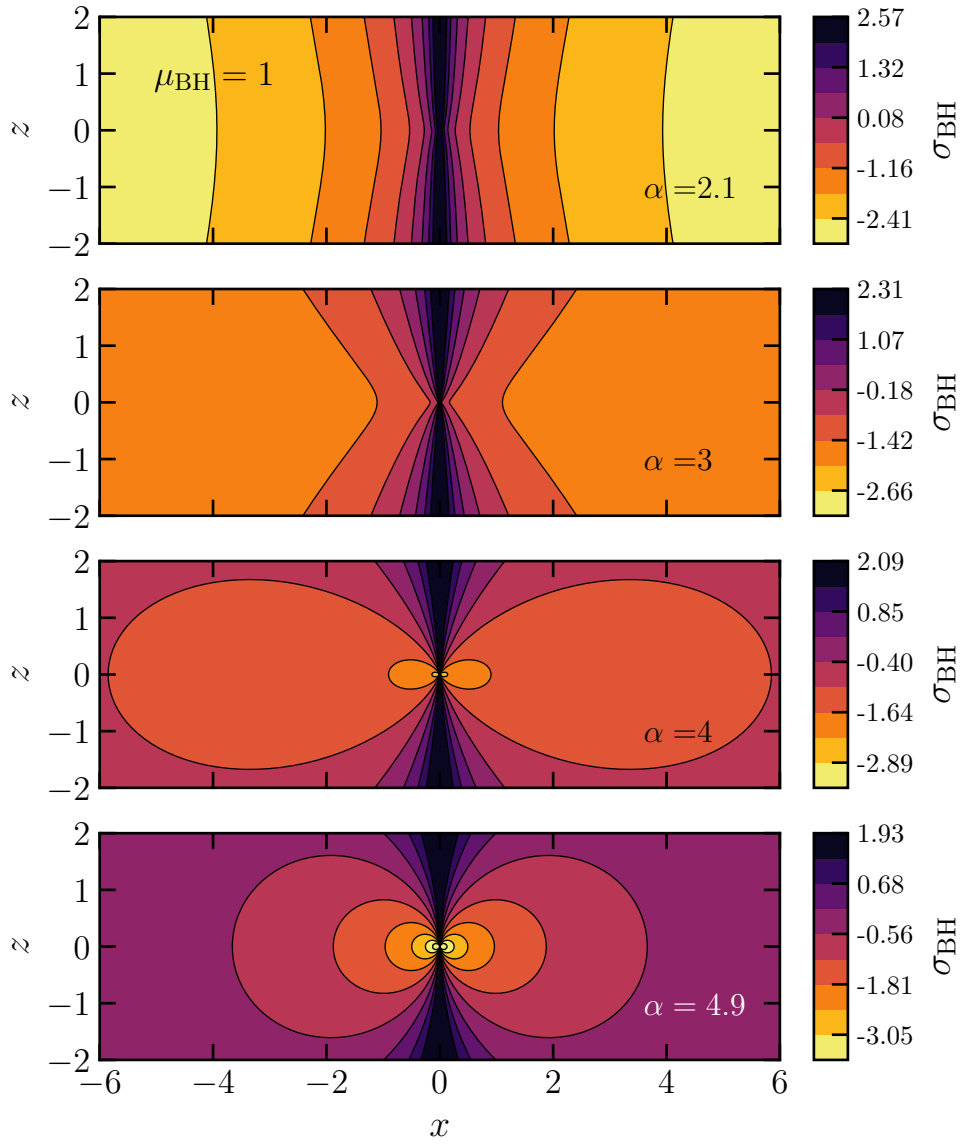

Figure 6.5: Entropy maps in the meridional plane for power-law tori in equilibrium in the black hole gravitational potential only with $\alpha = 2.1$, $\alpha = 3$, $\alpha = 4$ (from top to bottom) and $\alpha = 4.9$, for the monoatomic adiabatic index $\gamma = 5/3$, with $\mu_{\rm BH} = 1$.

Substituting eqs. 6.12-6.15 and the vertical partial derivative of the angular momentum squared

$$\frac{\partial \Omega_{\rm BH}^2 R^4}{\partial z} = -2\mu_{\rm BH}\frac{R^2 z}{(\alpha+1)r^3}, \tag{6.17}$$

in the second inequality of the Solberg-Høiland criterion (eq. 6.2), we obtain the second condition for stability

$$4\mu_{\rm BH} R^3 z^2 \frac{(\gamma-1)\alpha-\gamma}{(\alpha+1)r^{\alpha+6}} > 0. \tag{6.18}$$

The denominator in eq. 6.18 is positive, the numerator is positive for

$$\alpha > \frac{\gamma}{\gamma-1}. \tag{6.19}$$

Thus, for the power-law tori in equilibrium in the black hole gravitational potential the stability is not guaranteed for every value of α in the range $2 < \alpha < 5$, but only for α that satisfies the condition 6.19 dependent on γ. Substituting $\gamma = 7/5$ in 6.19 we find that the molecular biatomic gas tori are stable for $\alpha > 3.5$, whereas the tori composed of monoatomic gas are stable for $\alpha > 2.5$. The increase of the adiabatic index helps the stability of the systems.

Eq. 6.18 is not well defined at $z = 0$ and $R = 0$. As seen in Section 6.1, we need to care only of the behaviour along the radial axis. Starting from the dispersion relation, we have found the condition to check the stability along the R axis (eq. 6.8). Substituting eqs. 6.11, 6.13 and 6.15 evaluated in $z = 0$ in eq. 6.8, we obtain the condition for stability

$$\mu_{\rm BH}\frac{A_9}{\gamma(\alpha+1)R^3} > 0. \tag{6.20}$$

The fraction of eq. 6.20 is positive, thus along the R axis the systems are stable.

In conclusion, we proved in this section that the tori in equilibrium in the gravitational potential of the black hole are everywhere stable for α that satisfies the condition 6.19 on the adiabatic index γ. When α does not satisfied the condition 6.19 the tori are everywhere unstable, except on the R axis. The instability arises for $\alpha < 2.5$ for monoatomic gaseous tori and for $\alpha < 3.5$ for biatomic gaseous tori.

6.3 Stability of power-law tori in equilibrium in the gravitational potential of both black hole and gas

In this section we study the stability of the systems composed by the power-law tori and the central black hole, in equilibrium in the gravitational field due to the gas self-gravity and the black hole gravitational potential.

In the previous sections, we found that the self-gravitating power-law tori are everywhere stable and for every α in the range $2 < \alpha < 5$, whereas when they are in equilibrium only in the black hole gravitational potential the tori can be unstable for lower values of α dependent on γ. Therefore we could expect that this instability will be present in the systems that we are going to study and it will depend on the black holes properties.

As before we start studying the entropy of the systems. The normalized entropy for the power-law tori in equilibrium in the gas self-gravity and the black hole gravitational potential, in the range $2 < \alpha < 5$, is

$$\sigma = \ln\left(\frac{2(\alpha-1)\mu_{\rm BH} r^{\alpha+3} + (\alpha+1) f(\alpha)^{-1}\big[g(\alpha)R^2 + 4(\alpha-1)z^2\big]}{2(\alpha^2-1)R^{2(\gamma-1)} r^{\alpha(2-\gamma)-2}}\right). \tag{6.21}$$

The other constants are included in the additive constant of the entropy. Fig. 6.6 shows the entropy radial profiles for different values of α for the monoatomic and biatomic γ, for a black hole with $\mu_{\rm BH} = 10$. The entropy profiles for lower values of α increase outward for large distances, while close to the center the entropy profiles change their slope, i.e. they decrease with R. The value of γ modifies the slope close to the center, the entropy for $\alpha = 4$ decreases with R for $\gamma = 7/5$ and increases with R for $\gamma = 5/3$ (see also fig. 6.4). The stronger is the gravitational field of the black hole, i.e. larger $\mu_{\rm BH}$, the steeper is the slope close to the center (not shown in figure). For larger values of α the increase with R of the entropy holds also close to the center, but the slope is flatter. Looking at these profiles we expect that for lower values of α and close to the center, the systems might be unstable. Fig. 6.7 shows the entropy maps in the meridional plane, the contours of equal entropy remain almost the same compared to the self-gravitating tori for larger values of α. For lower values of α there is a change in the shape of the contours close to the center.

Fig. 6.8 shows the angular momentum squared profiles in the equatorial plane for different values of α, for $\mu_{\rm BH} = 1$. For every value of α, the angular momentum squared increases with R in the equatorial plane, with nearly the same slope close to the black hole and then with a slope steeper for lower values of α.

Substituting the radial and vertical partial derivatives of the pressure and the entropy, and the radial partial derivative of the angular momentum squared in eq. 6.1, we obtain the first condition for stability

$$\frac{c_1(R,z)\mu_{\rm BH}^2 + c_2(R,z)\mu_{\rm BH} + c_3(R,z)}{\gamma(\alpha^2-1)\Big[2(\alpha-1)f(\alpha)\mu_{\rm BH} r^{\alpha-3} + (\alpha+1)\big[g(\alpha)R^2 + 4(\alpha-1)z^2\big]\Big] R^2 r^{\alpha+2}} > 0, \tag{6.22}$$

with

$$c_1(R,z) = 2(\alpha-1)^2 f(\alpha) r^{2(\alpha-3)}\big[A_9 R^4 + A_{11} R^2 z^2 + 4(2\gamma-1)z^4 + A_{12} r^{2\alpha+3} R^2 z^2\big],$$

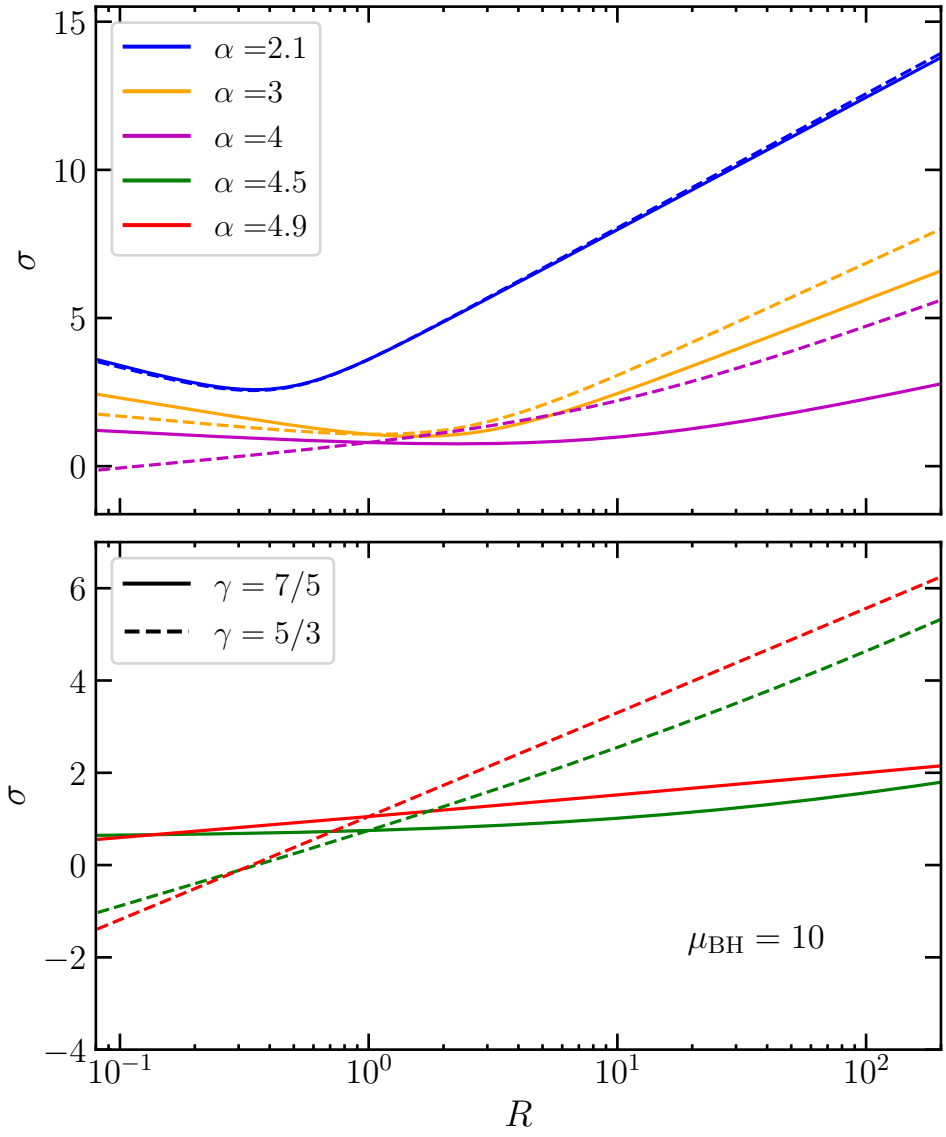

Figure 6.6: Radial entropy profiles for power-law tori in equilibrium in the gas self-gravity and the central black hole gravitational potential, with $\alpha = 2.1$, $\alpha = 3$, $\alpha = 4$ (top) , $\alpha = 4.5$ and $\alpha = 4.9$ (bottom), for the monoatomic $\gamma = 5/3$ (solid line) and biatomic adiabatic index $\gamma = 7/5$ (dashed line), for a black hole with $\mu_{\rm BH} = 10$. The profiles for the tori with $\alpha = 2.1$, with $\gamma = 5/3$ and $\gamma = 7/5$ overlap.

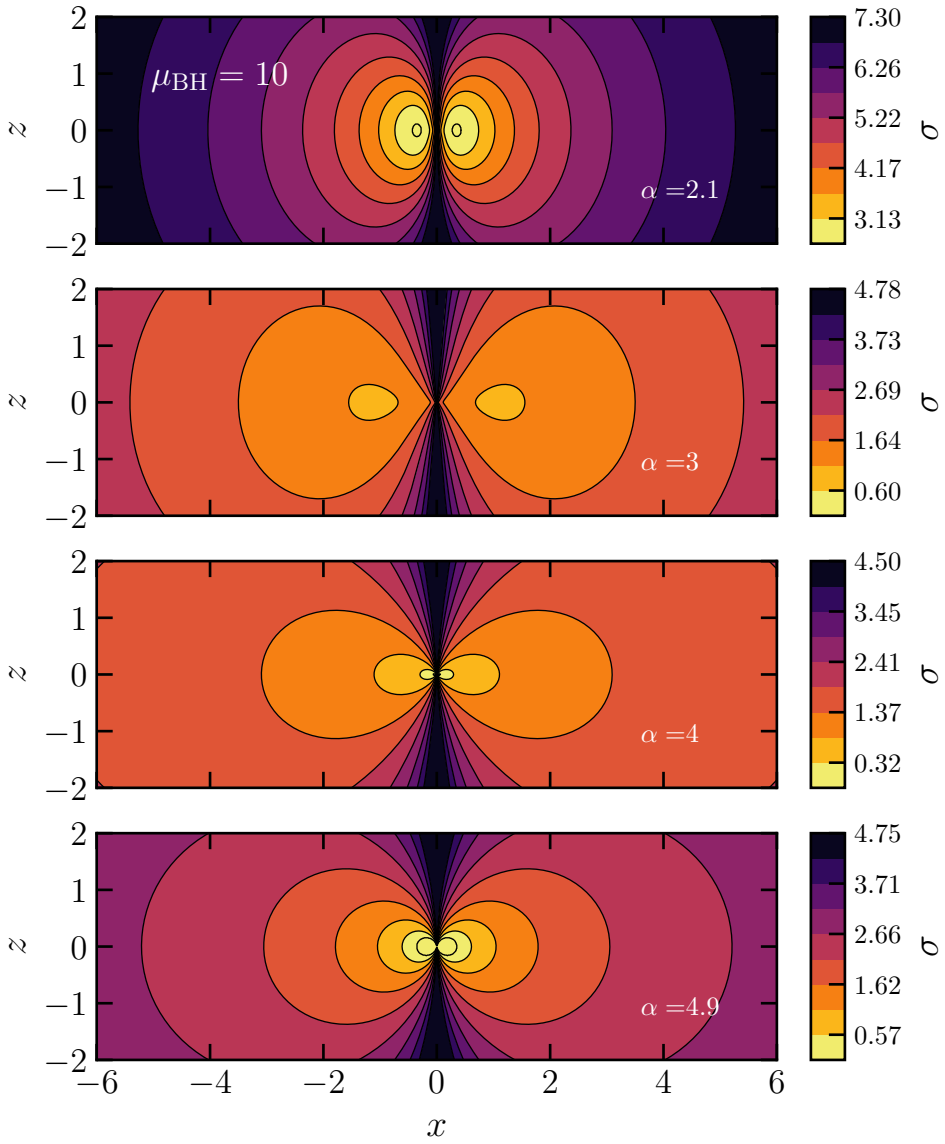

Figure 6.7: Entropy maps in the meridional plane for power-law tori in equilibrium in the gas self-gravity and the black hole gravitational potential with $\alpha = 2.1$, $\alpha = 3$, $\alpha = 4$ and $\alpha = 4.9$ (from top to bottom), for a monoatomic adiabatic index $\gamma = 5/3$ and for a black hole with $\mu_{\rm BH} = 10$.

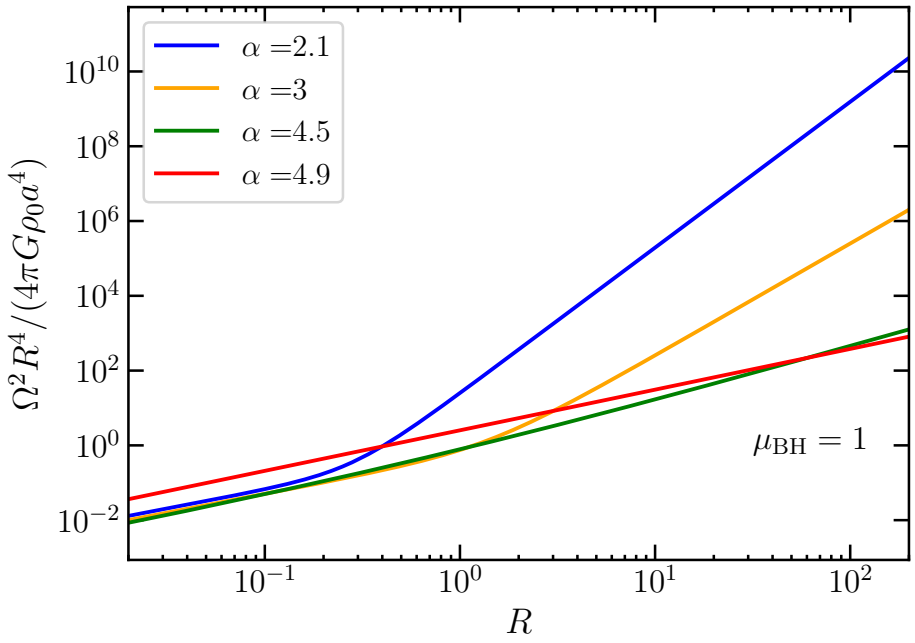

Figure 6.8: Radial angular momentum squared profiles for self-gravitating power-law tori in the presence of central black hole with $\mu_{\rm BH} = 1$, for $\alpha = 2.1$, $\alpha = 3$, $\alpha = 4$, $\alpha = 4.5$ and $\alpha = 4.9$.

$$c_2(R,z) = (\alpha^2-1)r^{\alpha-3}\Big[A_{12}R^6 + A_{13}R^4z^2 + A_{14}R^2z^4 + (\alpha-1)A_4z^6 + \\ + 5f(\alpha)(A_{15}R^2 + A_{16}z^2)R^2z^2r^{2\alpha+3}\Big],$$

and

$$c_3(R,z) = (\alpha+1)^2 f(\alpha)^{-1}\big[A_{17}R^8 + A_{18}R^6z^4 + A_{19}R^4z^4 + A_{20}R^2z^6 + A_4z^8\big] + \\ + 5(\alpha+1)^2(\alpha-1)\big[h(\alpha)R^2 + z^2\big]\big[A_{21}R^2 + A_{22}z^2\big]R^2z^2r^{2\alpha+3}.$$

In the numerator of eq. 6.22 there are coefficients $c_i(R,z)$ of powers of the black hole mass parameter $\mu_{\rm BH}$ that depend on the R and z coordinates. The coefficients of the coordinates A_i, which appear in the functions $c_i(R,z)$, depend on the values of α and γ. We denote with $c_i(R,z)$ functions that depend on the coordinates, which can depend also on α and γ, recalling that choosing the model implies the choice of α and γ, and so the polynomials A_i are constants and the functions $c_i(R,z)$ depend only on R and z.

The coefficients A_i for $i = 10, .., 29$ are positive for every value of α in the range considered and the γ values of interest, and we recall that the functions $f(\alpha)$, $g(\alpha)$ and $h(\alpha)$ are positive in the same range of α. Looking at the functions

$c_1(R,z)$, $c_2(R,z)$ and $c_3(R,z)$, we see that the powers of z are all even, and, since the coefficients A_i are positive, the functions $c_i(R,z)$ are positive for every R and z, for α in the range $2 < \alpha < 5$. Therefore the numerator of eq. 6.22 is positive. The denominator of eq. 6.22 is positive, because all the coefficients of R, z and r are positive, and z appears only squared. Thus the first inequality of the criterion is satisfied everywhere, for every value of α in the range $2 < \alpha < 5$, for the biatomic and monoatomic adiabatic index.

Substituting the vertical partial derivative of the pressure and the radial and vertical partial derivatives of the entropy and of the angular momentum squared in eq. 6.2, we obtain the other condition for stability

$$20R^3z^2\frac{c_4(R,z)\mu_{\rm BH}^3+c_5(R,z)\mu_{\rm BH}^2+c_6(R,z)\mu_{\rm BH}+c_7(R,z)}{(\alpha^2-1)\Big[2(\alpha-1)\mu_{\rm BH}r^{\alpha-3}+(\alpha+1)\big[g(\alpha)R^2+4(\alpha-1)z^2\big]\Big]}>0, \quad (6.23)$$

with

$$c_4(R,z)=2(\alpha-2)f(\alpha)\big[(\alpha-1)\gamma-\alpha\big]r^{2(\alpha-3)},$$

$$c_5(R,z)=(\alpha-2)\big[A_{23}R^2+A_{24}z^2\big]r^{\alpha-3},$$

$$c_6(R,z)=(\alpha-2)^{-1}\big[A_{25}R^4+A_{26}R^2z^2+A_{27}z^4\big],$$

and

$$c_7(R,z)=(\alpha+1)^2f(\alpha)^{-1}\big[h(\alpha)R^2+4z^2\big]\big[A_{29}R^4+A_{30}R^2z^2+A_7z^4\big]r^{3-\alpha}.$$

Also here functions of the coordinates that multiply powers of $\mu_{\rm BH}$ appear at the numerator. The denominator of eq. 6.23 is positive because the coefficients of R, r and z are positive in the range $2 < \alpha < 5$, and z is squared. The polynomials of α and γ that multiply the coordinates, A_i for $i = 23, .., 29$, are positive in the range $2 < \alpha < 5$ and for the γ of interest. The functions $c_i(R,z)$ for $i = 5, .., 7$ are functions of R, r and even powers of z thus they are positive everywhere. Therefore without considering the first term at the numerator $c_4(R,z)\mu_{\rm BH}^3$, the inequality 6.23 is verified. We now study the sign of $c_4(R,z)$. $c_4(R,z)$ is a function of r and the multiplicative coefficient is positive for

$$\alpha > \frac{\gamma}{\gamma-1}, \quad (6.24)$$

condition that we have already found in the systems in equilibrium in the black hole potential only (eq. 6.19). It follows that $c_4(R,z)$ is negative for $\alpha < 2.5$ for a monoatomic gas with $\gamma = 5/3$ and it is negative for $\alpha < 3.5$ for a biatomic gas with $\gamma = 7/5$. Thus, in these cases, the systems are unstable when

$$|c_4(R,z)|\mu_{\rm BH}^3 > c_5(R,z)\mu_{\rm BH}^2+c_6(R,z)\mu_{\rm BH}+c_7(R,z). \quad (6.25)$$

Considering the case when $c_4(R,z)$ is negative, the first requirement for the instability, at fixed distance, is that the black hole is massive, in fact since $c_4(R,z)$ multiplies the third power of $\mu_{\rm BH}$, if $\mu_{\rm BH}$ is small the term that can be reason of instability is smaller than the other linear terms of $\mu_{\rm BH}$ and the inequality 6.23 for the stability is satisfied.

The other property to take in account is the radial distance r from the center, i.e. from the black hole. We consider the radial distance dependence of the terms that appear at the numerator and at the denominator of eq. 6.22. Considering that the terms $\propto (R^2+z^2)=r^2$, we obtain

$$\frac{Ar^{2(\alpha-3)}\mu_{\rm BH}^3 + Br^{2(\alpha-3)}\mu_{\rm BH}^2 + Cr^4\mu_{\rm BH} + Dr^{6(3-\alpha)}}{Er^{\alpha-3}\mu_{\rm BH} + Fr^2} > 0. \tag{6.26}$$

The only term that can be negative is A. For $\alpha \lesssim 3.5$ we get

$$\frac{Ar\mu_{\rm BH}^3 + Br\mu_{\rm BH}^2 + Cr^4\mu_{\rm BH} + Dr^{-3}}{Er^{\frac{1}{2}}\mu_{\rm BH} + Fr^2} > 0. \tag{6.27}$$

whereas for $\alpha \lesssim 2.5$ we get

$$\frac{Ar^{-1}\mu_{\rm BH}^3 + Br^{-1}\mu_{\rm BH}^2 + Cr^4\mu_{\rm BH} + Dr^3}{Er^{-\frac{1}{2}}\mu_{\rm BH} + Fr^2} > 0. \tag{6.28}$$

We note that for $r \to 0$ the term $c_4(R,z)\mu_{\rm BH}^3$ that can cause instability (see eq. 6.25) is dominant because its dependence with r is linear. So the instability can be present close to the center and not at larger radii.

Equation 6.23 is not well defined on the R axis, thus we have to use the equation 6.8 derived from the dispersion relation. Substituting the radial partial derivative of the pressure, the normalized entropy and the angular momentum evaluated at $z=0$, we obtain the condition for stability

$$\frac{c_8(R)\mu_{\rm BH}^2 + c_9(R)\mu_{\rm BH} + c_{10}(R)}{3\gamma(\alpha^2-1)f(\alpha)\big[2(\alpha-1)f(\alpha)\mu_{\rm BH}R^{\alpha-3} + (\alpha+1)g(\alpha)R^2\big]} > 0, \tag{6.29}$$

with

$$c_8(R) = 2(\alpha-1)^2 f(\alpha)^2 A_{30} R^{2(\alpha-3)},$$

$$c_9(R) = (\alpha^2-1)A_{31}R^{\alpha-1},$$

$$c_{10}(R) = (\alpha+1)^2 g(\alpha) A_{32}.$$

Equation 6.29 has the same form as equation 6.22, but now the coefficients of the powers of $\mu_{\rm BH}$ are functions of the R coordinate only, because we have imposed

that $z = 0$. The denominator is positive because $f(\alpha)$ and $g(\alpha)$ are positive for α in tha range $2 < \alpha < 5$. All the functions $c_i(R)$ at the numerator are positive, because the polynomials of α and γ A_i are positive for the values of (α, γ) considered, as shown graphically in Appendix A. Thus eq. 6.29 is satisfied and the systems are stable along the R axis.

In conclusion we have shown that the systems composed of the power-law tori and the central black hole in equilibrium in the gravitational potentials of both the components are everywhere stable according to the Solberg-Høiland criterion, thus only for linear axysimmetric perturbations, for the values of α that satisfies the condition 6.19 dependent on γ. In the cases in which the condition 6.19 is not satisfied the systems can experience instability especially close to the center, and the region of instability is larger for more massive black holes.

We could speculate that these central instabilities can produce turbulence that could drive the inflow of the gas to the center via turbulent viscosity. For example, considering models of obscuring molecular tori in AGNs, the instabilities could cause inflow of gas that fuels the accretion disc around the black hole. But it is also possible that the instabilities could produce convective motions without producing significant inflows. The behaviour of the central regions of the tori under the instability should be studied with hydro-dynamical simulations. Running hydro-dynamical simulations one could check the stability also against non-axisymmetric perturbations and study the behaviour of the gas under instability in the central regions of the systems.

Chapter 7

Stability of weakly magnetized tori

In this chapter we consider the possible application of our models to system composed, for simplicity, of plasma, in the assumptions that the plasma is permeated by a weak magnetic field, i.e. the plasma has a high β parameter (see sec. 2.5).

The condition of stability for plasma permeated by a weak magnetic field is different from the Solberg-Høiland stability criterion. As we noted in sec. 2.5, for a high β plasma the unperturbed system satisfies the unmagnetized hydrodynamic equations, but the MHD equations must be used when the effect of perturbations is studied.

As the Solberg-Høiland stability criterion, the generalized magnetic criterion of stability that we are going to apply (Balbus, 1995) considers the response of the system to axisymmetric linear perturbations. In practice, in the presence of a weak magnetic field, the criterion of stability is the same as the Solberg-Høiland criterion, except for replacing the angular momentum with the angular velocity. So for the stability of a plasma the gradient of the angular velocity is important, rather than that of the angular momentum.[1] For many systems this condition is too restrictive, so they are unstable when permeated by a weak magnetic field and, as we will see, also the models under consideration are unstable when they are permeated by a weak magnetic field. We recall that the condition for stability does not hold for strong magnetic fields because the unperturbed systems are stationary only in the absence of strong magnetic fields.

Since we are dealing with a plasma, in this section, we consider the monoatomic adiabatic index $\gamma = 5/3$.

The dispersion relation for a weakly magnetized rotating, stratified fluid is

$$\omega^2 = -R\left(x\frac{\partial\Omega^2}{\partial R} - \frac{\partial\Omega^2}{\partial z}\right) - \frac{3}{5\rho}\left(x\frac{\partial P}{\partial z} - \frac{\partial P}{\partial R}\right)\left(x\frac{\partial\sigma}{\partial z} - \frac{\partial\sigma}{\partial R}\right). \tag{7.1}$$

[1] We recall that also for thin discs the magneto-rotational instability derives from a condition on the angular velocity. The condition for stability requires that the angular velocity increases outward (Balbus and Hawley, 1991; Chandrasekhar, 1960)

As seen in sec. 2.5, the magnetic field does not appear in the dispersion relation, and thus in the stability condition, for weakly magnetized plasma. Imposing that $\omega^2 > 0$ for stability, we obtain the conditions for generalized magneto rotational stability for stationary baroclinic systems (Balbus, 1995)

$$\frac{3}{5\rho}\left(\frac{\partial P}{\partial R}\frac{\partial \sigma}{\partial R}+\frac{\partial P}{\partial z}\frac{\partial \sigma}{\partial z}\right)-R\frac{\partial \Omega^2}{\partial R}<0 \tag{7.2}$$

and

$$\frac{\partial P}{\partial z}\left[\frac{\partial \Omega^2}{\partial R}\frac{\partial \sigma}{\partial z}-\frac{\partial \Omega^2}{\partial z}\frac{\partial \sigma}{\partial R}\right]<0. \tag{7.3}$$

As before, in the application of equations 7.2 and 7.3, polynomials of α will appear. The polynomials are not explicitly functions of γ because we are considering $\gamma = 5/3$. The polynomials are indicated with B_i, and once chosen the model, so the value of α, they are numerical constants. The polynomials B_i for $i = 1, .., 14$ are listed in Appendix B, and they are positive for α in the range $2 < \alpha < 5$, as checked graphically.

As usual, we are going to consider first the stability of the systems in equilibrium in the gas self-gravity (sec. 7.1), then in equilibrium in the black hole gravitational potential (sec. 7.2) and, finally, we consider the systems in equilibrium in both gas self-gravity and black hole potential (sec. 7.3).

7.1 Magnetic stability of self-gravitating power-law tori without the central black hole

Fig. 7.1 shows the angular velocity profiles in the equatorial plane of the power-law tori for different values of α. We note that the angular velocity decreases with R for every values of α, with a slope steeper for larger values of α. We recall that the magneto-rotational instability criterion requires that the angular velocity must increase radially (Balbus and Hawley, 1991; Chandrasekhar, 1960).

Substituting the radial and vertical partial derivatives of the pressure and of the normalized entropy and the radial partial derivative of the squared angular velocity in eq. 7.2, we obtain the condition for stability

$$\frac{B_1R^6+B_2R^4z^2+B_3R^2z^4+96(\alpha-1)^2z^6}{5(\alpha-1)f(\alpha)\left[g(\alpha)R^2+4(\alpha-1)z^2\right]R^2r^\alpha}<0. \tag{7.4}$$

The fraction in eq. 7.4 is function of R, r and even powers of z, all the coefficients of the coordinates (B_i and the others), functions of α, are positive in the range of α considered, as shown in Appendix B, or easily checked analytically. Thus the fraction in eq. 7.4 is positive and the first inequality is not satisfied everywhere, for every values of α in the range $2 < \alpha < 5$.

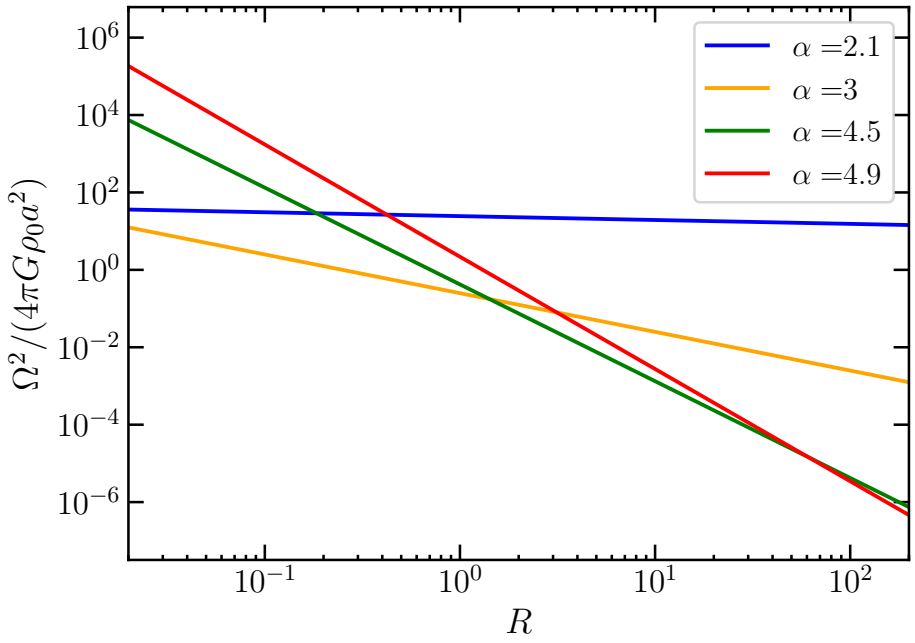

Figure 7.1: Radial angular velocity squared profiles for self-gravitating power-law tori without a central black hole, for $\alpha = 2.1$, $\alpha = 3$, $\alpha = 4$, $\alpha = 4.5$ and $\alpha = 4.9$.

Substituting the radial and vertical partial derivative of the angular momentum and of the normalized entropy and the vertical partial derivative of the pressure in eq. 7.3, we obtain the second condition for stability

$$4z^2 \frac{\left[(\alpha-1)(6-\alpha)R^2+4z^2\right]\left[B_4R^4+B_5R^2z^2+8B_6z^4\right]}{3(\alpha-1)(\alpha-2)^{-1}f(\alpha)^2\left[g(\alpha)R^2+4(\alpha-1)z^2\right]R^2r^{3\alpha}} < 0. \tag{7.5}$$

As before, the fraction in eq. 7.5 is function of R, r and even powers of z. All the coefficients of the coordinates, functions of α, are positive in the range of α considered $2 < \alpha < 5$. The sign of some of them is easily checked analytically, while the polynomials B_i are plotted in Appendix B. Thus the fraction in eq. 7.4 is positive. Also the second inequality is not satisfied everywhere, for every values of α in the range $2 < \alpha < 5$, except for $z = 0$ that it is not well defined.

As usual to consider the behaviour of the systems on the R axis we start from the dispersion relation (eq. 7.1) and imposing that ω^2 has to be positive we get

$$\frac{3}{5\rho}\frac{\partial P}{\partial z}\frac{\partial \sigma}{\partial z}x^2+\left[R\frac{\partial \Omega^2}{\partial z}-\frac{3}{5\rho}\left(\frac{\partial P}{\partial R}\frac{\partial \sigma}{\partial z}-\frac{\partial P}{\partial z}\frac{\partial \sigma}{\partial R}\right)\right]x+\frac{3}{5\rho}\frac{\partial P}{\partial R}\frac{\partial \sigma}{\partial R}-R\frac{\partial \Omega^2}{\partial R} < 0. \tag{7.6}$$

Evaluating it at $z = 0$, where all the vertical partial derivatives get null, we obtain

$$\frac{3}{5\rho}\left(\frac{\partial P}{\partial R}\frac{\partial \sigma}{\partial R}\right)\Bigg|_{z=0} - R\frac{\partial \Omega^2}{\partial R}\Bigg|_{z=0} < 0. \tag{7.7}$$

Substituting the radial partial derivative of the angular momentum, of the normalized entropy and of the pressure evaluated at $z = 0$ in eq. 7.7, we obtain the condition for stability

$$\frac{B_1 g(\alpha)^{-1}}{5(\alpha-1)R^{\alpha-2}} < 0. \tag{7.8}$$

Since the term B_1 is positive for every value of α in the range $2 < \alpha < 5$, this last condition is not verified and the systems are not stable along the R axis.

In conclusion we have proved that the power-law tori in equilibrium in the gas self-gravity, permeated by a weak magnetic filed are unstable everywhere, for every value of α in the range $2 < \alpha < 5$.

7.2 Magnetic stability of power-law tori in equilibrium in the black hole gravitational potential

We consider here the magnetic stability criterion, in the case which the power-law tori are in equilibrium in the black hole gravitational potential. The rotational velocity in this case is Keplerian, $v_\phi^2 \propto 1/r$, thus the angular velocity decreases in the equatorial for every value of α. Substituting the radial and vertical partial derivatives of the pressure, of the normalized entropy and of the angular velocity squared in eqs. 7.2 and 7.3, we obtain the conditions for stability

$$\mu_{\rm BH}\frac{(B_7 R^2 + 4z^2)}{5(\alpha+1)R^2 r^3} < 0 \tag{7.9}$$

and

$$4\mu_{\rm BH}^2 z^2 \frac{(2\alpha-1)}{3(\alpha+1)Rr^{\alpha+6}} < 0. \tag{7.10}$$

As before the terms that appear in eqs. 7.9, 7.10 are positive. In the numerator of eq. 7.9 there are functions of R and z^2 and the coefficients that multiply the coordinates are positive. The term in the numerator of eq. 7.10 is positive for every α in the range $2 < \alpha < 5$, and the fraction multiplies z^2. The denominator of eqs. 7.9, 7.10 are both positive, because they are functions of R and r, and the multiplicative coefficients are positive. Therefore eqs. 7.9 and 7.10 are not satisfied everywhere, for every value of α in the range $2 < \alpha < 5$, except for the latter equation along the z axis, where it is not well defined.

To study the stability along the R axis, we have to use the condition for stability found at $z = 0$ (eq. 7.7). Substituting in eq. 7.7 the physical properties gradients of the systems in equilibrium in the black hole gravitational potential, we get the following condition for stability

$$\frac{B_7 \mu_{\rm BH}}{5(\alpha+1)R^3} < 0. \tag{7.11}$$

Since the term B_7 and the coefficient at the denominator are positive, the inequality 7.11 is not satisfied and the systems are unstable also along the R axis.

In conclusion, the power-law tori weakly magnetized in equilibrium in the black hole potential are unstable everywhere, for every value of α in the range $2 < \alpha < 5$.

7.3 Magnetic stability of power-law tori in equilibrium in the gravitational potential of both black hole and gas

In this section we study the stability of weakly magnetized power-law tori with a central black hole in equilibrium in the gas self-gravity and the black hole gravitational potential. Fig. 7.2 shows the angular velocity profiles in the equatorial plane of the power-law tori with a central black hole with $\mu_{\rm BH} = 1$, for different values of α. We note that the angular velocity decreases with R for every values of α, with nearly the same slopes for all the profiles close to the center (i.e. in the region of the black hole influence) and then with a different slope steeper for larger values of α, same as fig. 7.1.

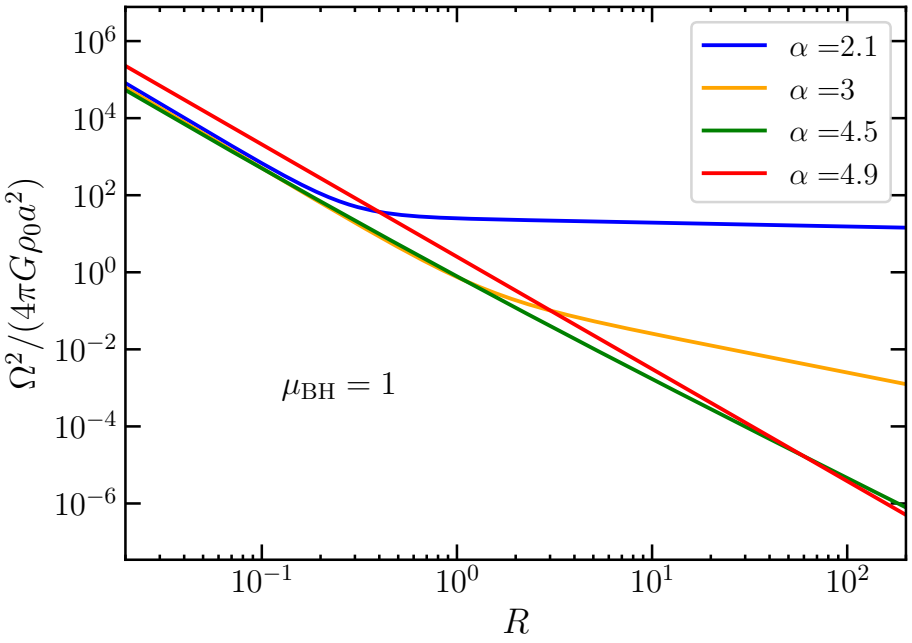

Figure 7.2: Radial angular velocity squared profiles for self-gravitating power-law tori with a central black hole with $\mu_{\rm BH} = 1$, for $\alpha = 2.1$, $\alpha = 3$, $\alpha = 4$, $\alpha = 4.5$ and $\alpha = 4.9$.

Substituting the radial and vertical partial derivatives of the pressure, of the normalized entropy and of the squared angular velocity in equations 7.2 and 7.3, we obtain the following conditions for stability:

$$\frac{d_1(R,z)\mu_{\rm BH}^2 + d_2(R,z)\mu_{\rm BH} + d_3(R,z)}{5(\alpha^2-1)\Big[2\mu_{\rm BH}r^{\alpha-3} + (\alpha+1)f(\alpha)^{-1}\big[g(\alpha)R^2 + 4(\alpha-1)z^2\big]\Big]r^{\alpha}} < 0 \qquad (7.12)$$

and

$$\frac{4z^2\big[d_4(R,z)\mu_{\rm BH}^3 + d_5(R,z)\mu_{\rm BH}^2 + d_6(R,z)\mu_{\rm BH} + d_4(R,z)\big]}{3(\alpha+1)\Big[2r^{\alpha-3}\mu_{\rm BH} + 3(\alpha+1)f(\alpha)^{-1}\big[g(\alpha)R^2 + 4(\alpha-1)z^2\big]\Big]Rr^{3\alpha}} < 0, \quad (7.13)$$

with

$$d_1(R,z) = 2\big[B_7R^2 + 12z^2\big]r^{2(\alpha-3)},$$

$$d_2(R,z) = (\alpha+1)\big[B_8R^4 + B_9R^2z^2 + 96(\alpha-1)z^4\big]r^{\alpha-3},$$

$$d_3(R,z) = (\alpha+1)^2f(\alpha)^{-1}\big[B_1R^6 + B_2R^4z^2 + 8(\alpha-1)B_3R^2z^4 + 96(\alpha-1)^2z^6\big],$$

$$d_4(R,z) = 2(2\alpha-1)r^{3(\alpha-3)},$$

$$d_5(R,z) = f(\alpha)^{-1}(\alpha-1)r^{2(\alpha-3)}\big[B_{10}R^2 + B_{11}z^2\big],$$

$$d_6(R,z) = f(\alpha)^{-2}(\alpha+1)r^{\alpha-3}\big[B_{12}R^4 + B_{13}R^2z^2 + 8(7\alpha-8)(\alpha-1)^2(\alpha+1)z^4\big],$$

and

$$d_7(R,z) = (\alpha-1)(\alpha-2)(\alpha+1)^2f(\alpha)^{-3}\big[B_4R^4 + B_5R^2z^2 + B_6z^4\big].$$

Once again in the conditions for stability for the systems in equilibrium in the gas self-gravity and the black hole potential, powers of the black hole mass parameter $\mu_{\rm BH}$ appear. The coefficients that multiply $\mu_{\rm BH}$, indicated with $d_i(R,z)$ are functions of the R and z coordinates. The coordinates themselves are multiplied by the coefficients B_i, that are functions of α only, and are listed in Appendix B and studied graphically (figs. B.1-B.2). We recall that all the polynomials B_i are positive for α in the range $2 < \alpha < 5$, and that once chosen the model, i.e. the value of α, these polynomials are numerical constants. For the other coefficients of the coordinates that appear in $d_i(R,z)$, explicitally written, the study of the

sign is easy to check analytically in the range of α considered, and they are not plotted.

Therefore we note that all the functions $d_i(R,z)$ for $i = 1,..,7$ are positive everywhere because the coefficients of the coordinates are positive and the powers of z that appear in them are even. Thus, since the parameter $\mu_{\rm BH}$ is positive defined, the numerators of eqs. 7.12 and 7.13 are positive. The denominators of eqs. 7.12, 7.13 are positive, so the conditions for stability in the presence of a weak magnetic field are everywhere not satisfied, except in the z axis, where the second equation is not well defined. As usual, we consider the condition obtained by considering the dispersion relation at $z = 0$ (eq. 7.7). Substituting the radial partial derivatives of the pressure, of the normalized entropy and of the angular velocity squared in eq. 7.7, we obtain the condition for stability

$$\frac{d_1(R)\mu_{\rm BH}^2 + d_2(R)\mu_{\rm BH} + d_3(R)}{5(\alpha^2-1)f(\alpha)\big[2(\alpha-1)f(\alpha)\mu_{\rm BH}R^{\alpha-3} + (\alpha+1)g(\alpha)R^2\big]R^\alpha} < 0, \qquad (7.14)$$

with

$$d_1(R) = 2(\alpha-1)^2 f(\alpha) B_7 R^{2(\alpha-3)},$$

$$d_2(R) = (\alpha-1)(\alpha^2-1) f(\alpha)^2 B_8 R^{\alpha-1},$$

$$d_3(R) = (\alpha+1)^2 B_1.$$

For the considerations already noted, the denominator of eq. 7.14 is positive. At the numerator appear functions of R coordinate that multiply powers of $\mu_{\rm BH}$. The functions $d_i(R)$ are positive for every R in the α range considered, therefore the numerator of eq. 7.14 is positive. The inequality for stability 7.14 is not satisfied along the R axis for every α in the range $2 < \alpha < 5$. Therefore, we have shown that the power-law tori in equilibrium in the gas self-gravity and the black hole gravitational potential are unstable everywhere for every value of α in range $2 < \alpha < 5$.

In this chapter, we showed that the power-law tori are unstable both in the self-gravitating case and in the presence of a central black hole, when they are permeated by a weak magnetic field. This instability is a generalized form of magneto-rotational instability (Balbus and Hawley, 1991; Chandrasekhar, 1960), in which the stratification of the fluid is considered. The magneto-rotational instability appears in many dynamical plasma models. The physical reason of instability is that the magnetic field tends to force the system to a rigid rotation. Since the angular velocity, usually, decreases outward, a fluid element in the inner orbits is accelerated by the magnetic field and, increasing its rotation velocity, it tends to go inward (Balbus, 1995). The magneto-rotational instability is the

likely process to drive the accretion flow in thin discs. In the magnetic stability criterion for baroclinic system, there are also gradients of the pressure and the entropy. To study the behaviour of the power-law tori under the magnetic instability, running magneto-hydro-dynamics simulations is necessary, corroborated with further detailed theoretical analysis.

Conclusions and future perspectives

In this final section, we summarize the conclusions and the results obtained in this work and describe a few future perspective about this study.

The main conclusions about this work are the following:

- We presented models of self-gravitating gaseous tori in the absence and the presence of a central black hole. We took as starting point the analytic potential-density pairs presented by Ciotti and Bertin (2005). The models have power-law density distributions with power-law index α in the range $2 < \alpha < 5$. We computed analytically the surface densities of the systems when projected face-on and edge-on. The edge-on surface density diverge for tori with $\alpha < 3$, but we found that these tori have infinite mass so a truncation radius has to be considered in a possible astrophysical application. The edge-on surface density distributions have a peanut shape, that reflects the toroidal geometry, whereas the contours of equal face-on surface density are circles. The face-on projected surface density profiles are power laws, thus without a central depression. We found that for different values of α the properties of the tori can change significantly. The self-gravitating tori without the central black hole with $\alpha < 2.44$ do not admit circular orbits, but the addition of other components can change this undesirable property. For instance, with addition of the black hole of sufficiently high mass circular orbits can exist also for $\alpha < 2.44$.

- From the integration of the axisymmetric stationary Euler equation we found the rotation velocity and the temperature distributions for the self-gravitating power-law tori without external potential. These systems have baroclinic distributions, with angular velocity that depends on both R and z. The isorotational surfaces move away from cylinders slightly for α near the central values in the range $2 < \alpha < 5$ and in a marked way for the values of α near the limits of the range. When the systems are interpreted as dominated by turbulence, or composed of discrete gas clouds, we found that the rotational velocity and the velocity dispersion are of the same order of magnitude: a high velocity dispersion and thus pressure support is expected to maintain the systems thick.

- We computed the physical properties of the power-law tori in the external potential of the black hole and in equilibrium in the gas self-gravity and the black hole potential. In the former, we found that the temperature and the rotational velocity distributions are spherically symmetric. The rotation velocity has a Keplerian behaviour $v_\phi^2 \propto 1/r$. In the latter we found a rotation velocity and temperature distributions that are characterised by a marked axisymmetric distribution at large radii from the center, and a rounder, nearly spherical distribution close to the center. Of course, the models are significantly affected by the value of the black hole mass.

- We proved that the self-gravitating power-law tori without external potential are everywhere stable, for every values of α in the range considered, against linear axisymmetric perturbations. For some values of α the power-law tori in equilibrium in the gas and the black hole potentials can experience instability in the central regions. In particular the condition of stability on the value of α, which depends only on the value of the adiabatic index γ, is

$$\alpha > \frac{\gamma}{\gamma - 1}.$$

  The instability appear mainly in the models with low values of α.

- Finally, we shown that the power-law tori are everywhere unstable , for every value of α in the range considered, when they are permeated by a weak magnetic field, both in the presence and in the absence of the black hole.

The work done in this thesis can be considered a starting point of a more extended investigation of the properties of power-law tori and their application to astrophysical systems. A possible future development is extending the models including also other components. For instance, it would be interesting to consider the system composed of the torus with the central black hole surrounded by galactic components such as a spheroid (for instance a singular isothermal sphere) or a disc (for instance a Kuzmin disc). It is useful to explore whether the models remain stable with the addition of these components and how the system dynamics is modified.

Running numerical hydro-dynamic simulations is the way to study the evolution of the systems with the central black hole under instability of the central regions, to see what kinds of processes this instability drives. Since the Solberg-Høiland criterion analyses the linear stability to axisymmetric perturbations, hydrodynamic simulations will be useful also to study the stability of the unmagnetized fluid models against non-linear or non-axisymmetric perturbations. For the models permeated by a weak magnetic field, magneto-hydro-dynamics numerical simulations can study the behaviour of the power-law tori under instability with or without the central black hole.

Finally, there are the astrophysical applications with fits to observational data. Through the use of specific tools, like, for example, the Monte Carlo Markov chains, it will be possible to fit, with these models, observational data of specific astrophysical objects. In the thesis we showed examples of applications to the molecular tori of AGN, and from qualitative comparisons we found that the main properties of the models are similar to those inferred from the observational data. Fitting the models to the data of AGN central obscurers will show whether these models can be applied to explain the dynamics of the dusty molecular tori. As far as we known, these would be the first self-consistent dynamical models applied to this kind of systems. Moreover, an attempt of data fitting can be done also for the toroidal accretion discs around the black holes, to explore whether these models can be applied also to describe the dynamics of these astrophysical objects.

Acknowledgements I warmly thank my supervisors Prof. Carlo Nipoti, for the continuous help in structuring and writing this work and his constant presence, and Prof. Luca Ciotti for suggesting and driving the work. I want to thank both for the enlightening discussions about every topic. I thank my colleagues of the research group headed by Carlo Nipoti and Federico Marinacci, for their useful comments. A special thank to Raffaele Pascale for the very useful help in the construction of the figures shown in this work. Finally, I want to thank my colleagues and friends Laura Di Federico and Elena Marcuzzo for being always helpful and present for every question and problem.

Appendix A

This Appendix and the next contain the lists and the plots of the polynomials of α, or also of γ, that appear in the analytic computing of several expressions in this work. We recall that the power-law density distribution $\rho \propto R^2 r^{-\alpha}$ is defined for α in range $2 < \alpha < 5$.

Recurring functions of α are

$$f(\alpha) = (\alpha - 2)^2(5 - \alpha)(7 - \alpha), \tag{A.1}$$

$$g(\alpha) = 16 + \alpha(5 - \alpha)(\alpha - 4), \tag{A.2}$$

$$h(\alpha) = -\alpha^2 + 7\alpha - 6. \tag{A.3}$$

$f(\alpha)$ is positive in the range $2 < \alpha < 5$, as easily to check, the functions $g(\alpha)$ and $h(\alpha)$ are plotted for α in range $2 < \alpha < 5$ in fig. A.1 (upper panels). They are positive in the α range considered.

In the following, polynomials of α, with coefficients dependent on γ, that appear in the stability conditions (chap. 6), are listed. For the polynomials A_4, A_7 and A_{11} is easily to check that they are positive for α in $2 < \alpha < 5$, for any $\gamma > 1/2$, $\gamma > \alpha/4$ (≈ 1.25 for largest α), and $\gamma > 1$, respectively. The other polynomials A_i for $i = 1, .., 32$, $i \neq 4$, $i \neq 7$ and $i \neq 11$ are plotted in figs. A.1-A.4 for α in range $2 < \alpha < 5$, and for biatomic $\gamma = 7/5$ and monoatomic adiabatic index $\gamma = 5/3$. As shown in the figures, they are positive for the values of (α, γ) considered. The polynomials A_i for $i = 1, .., 32$, are

$$\begin{aligned} A_1 = g(\alpha)\big[&(-\alpha^5 + 14\alpha^4 - 73\alpha^3 + 192\alpha^2 - 276\alpha + 192)\gamma + \\ &+ 2(\alpha^5 - 15\alpha^4 + 83\alpha^3 - 217\alpha^2 + 276\alpha - 144)\big], \end{aligned}$$

$$\begin{aligned} A_2 = 4\big[&(-\alpha^6 + 11\alpha^5 - 35\alpha^4 + 17\alpha^3 + 132\alpha^2 - 268\alpha + 192)\gamma + \\ &+ 2(\alpha^6 - 14\alpha^5 + 71\alpha^4 - 168\alpha^3 + 178\alpha^2 - 48\alpha - 36)\big], \end{aligned}$$

$$A_3 = 16(\alpha - 1)\big[(-\alpha^3 + 13\alpha^2 - 36\alpha + 40)\gamma + 2(-4\alpha^2 + 7\alpha - 9)\big],$$

$$A_4 =32(\alpha-1)^2(2\gamma-1),$$

$$A_5 =g(\alpha)(\alpha^3-5\alpha^2+4\alpha+12)\gamma+ \\ +2\alpha(\alpha^5-16\alpha^4+97\alpha^3-282\alpha^2+388\alpha-204)\big],$$

$$A_6 =4(\alpha-1)^2\big[(\alpha-1)(-\alpha^3+13\alpha^2-36\alpha-44)\gamma-4\alpha\big],$$

$$A_7 =8(4\gamma-\alpha)(\alpha-1)^2,$$

$$A_8 =(-\alpha^5+14\alpha^4-73\alpha^3+192\alpha^2-276\alpha+192)\gamma-2g(\alpha)(\alpha-3)^2,$$

$$A_9 =(\alpha^2-3\alpha+4)\gamma-(\alpha-1)^2,$$

$$A_{10} =(3-\alpha)\gamma+(\alpha-1)^2,$$

$$A_{11} =5(\alpha+1)f(\alpha)(\alpha(\gamma-1)+1),$$

$$A_{12} =(-3\alpha^5+40\alpha^4-197\alpha^3+496\alpha^2-680\alpha+448)\gamma-4g(\alpha)(\alpha-1)(\alpha-3),$$

$$A_{13} =4\big[(-3\alpha^4+33\alpha^3-131\alpha^2+233\alpha-88)\gamma-4(\alpha-2)(5-\alpha)(\alpha^2-3\alpha+3)\big],$$

$$A_{14} =16\big[(5-\alpha)(\alpha^2-2\alpha+3)\gamma+4\alpha^3-6\alpha^2+12\alpha-11\big],$$

$$A_{15} =\alpha(-3\alpha^4+28\alpha^3-69\alpha^2+60\alpha-8)\gamma-4(\alpha-1)^2(\alpha+1)(\alpha-2)(6-\alpha),$$

$$A_{16} =4(\alpha-1)\big[(3\alpha(\alpha-1))\gamma-4(\alpha+1)(\alpha-2)\big],$$

$$A_{17} =g(\alpha)\big[(-\alpha^5+14\alpha^4-73\alpha^3+192\alpha^2-276\alpha+192)\gamma-2(\alpha-3)^2\big],$$

$$A_{18} =4\big[(-\alpha^7+19\alpha^6-148\alpha^5+627\alpha^4-1061\alpha^3+2524\alpha^2-2284\alpha+960)\gamma+ \\ -2g(\alpha)(\alpha-3)(\alpha^3-7\alpha^2+14\alpha-12)\big],$$

$$A_{19} =(\alpha^6-12\alpha^5+49\alpha^4-82\alpha^3+68\alpha^2-8\alpha+32)\gamma+ \\ +2(-\alpha^6+12\alpha^5-51\alpha^4+102\alpha^3-118\alpha^2+88\alpha-48),$$

$$A_{20} = 32(\alpha-1)\big[(-\alpha^3+8\alpha^2-17\alpha+18)\gamma+\alpha^3-7\alpha^2+14\alpha-12\big],$$

$$A_{21} = \alpha g(\alpha)\gamma - 2(\alpha-1)^2(\alpha-2)(6-\alpha),$$

$$A_{22} = 4(\alpha-1)((\gamma-2)\alpha+4),$$

$$\begin{aligned}A_{23} =&(-3\alpha^5+33\alpha^4-105\alpha^3+127\alpha^2-36\alpha+32)\gamma+\\ &+2\alpha(-2\alpha^4+21\alpha^3-58\alpha^2+37\alpha+34),\end{aligned}$$

$$A_{24} = +4\big[(3\alpha^2-2\alpha+7)\gamma-2\alpha(2\alpha+1)\big],$$

$$\begin{aligned}A_{25} =&(\alpha^8-23\alpha^7+201\alpha^6-869\alpha^5+2030\alpha^4-2500\alpha^3+1416\alpha^2-256\alpha+96)\gamma+\\ &-2\alpha(\alpha^7-23\alpha^6+205\alpha^5-917\alpha^4-2230\alpha^3-2896\alpha^2+1780\alpha-348),\end{aligned}$$

$$\begin{aligned}A_{26} =&(\alpha^5+10\alpha^4-25\alpha^3+22\alpha^2+6\alpha-4)\gamma+\\ &+2\alpha(\alpha^4-12\alpha^3+46\alpha^2-80\alpha+53),\end{aligned}$$

$$A_{27} = 8(\alpha-1)^2\big[2(\alpha^2+3\alpha-4)\gamma-\alpha(5\alpha-7)\big],$$

$$\begin{aligned}A_{28} =&(-\alpha^6+14\alpha^5-69\alpha^4+140\alpha^3-52\alpha^2-176\alpha+192)\gamma+\\ &+2\alpha(\alpha^5-16\alpha^4+97\alpha^3-282\alpha^2+388\alpha-204),\end{aligned}$$

$$A_{29} = 4(\alpha-1)^2\big[(-\alpha^3+13\alpha^2-36\alpha^{+}44)\gamma-4\alpha(\alpha-1)\big],$$

$$A_{30} = 6\gamma+(2\alpha-7)(\alpha-1),$$

$$A_{31} = 6\gamma(-3\alpha^3+31\alpha^2-96\alpha+112)+g(\alpha)(3\alpha^2-17\alpha+34),$$

$$A_{32} = 6(-\alpha^3+11\alpha^2-38\alpha+48)\gamma+g(\alpha)(\alpha-3)(8-\alpha).$$

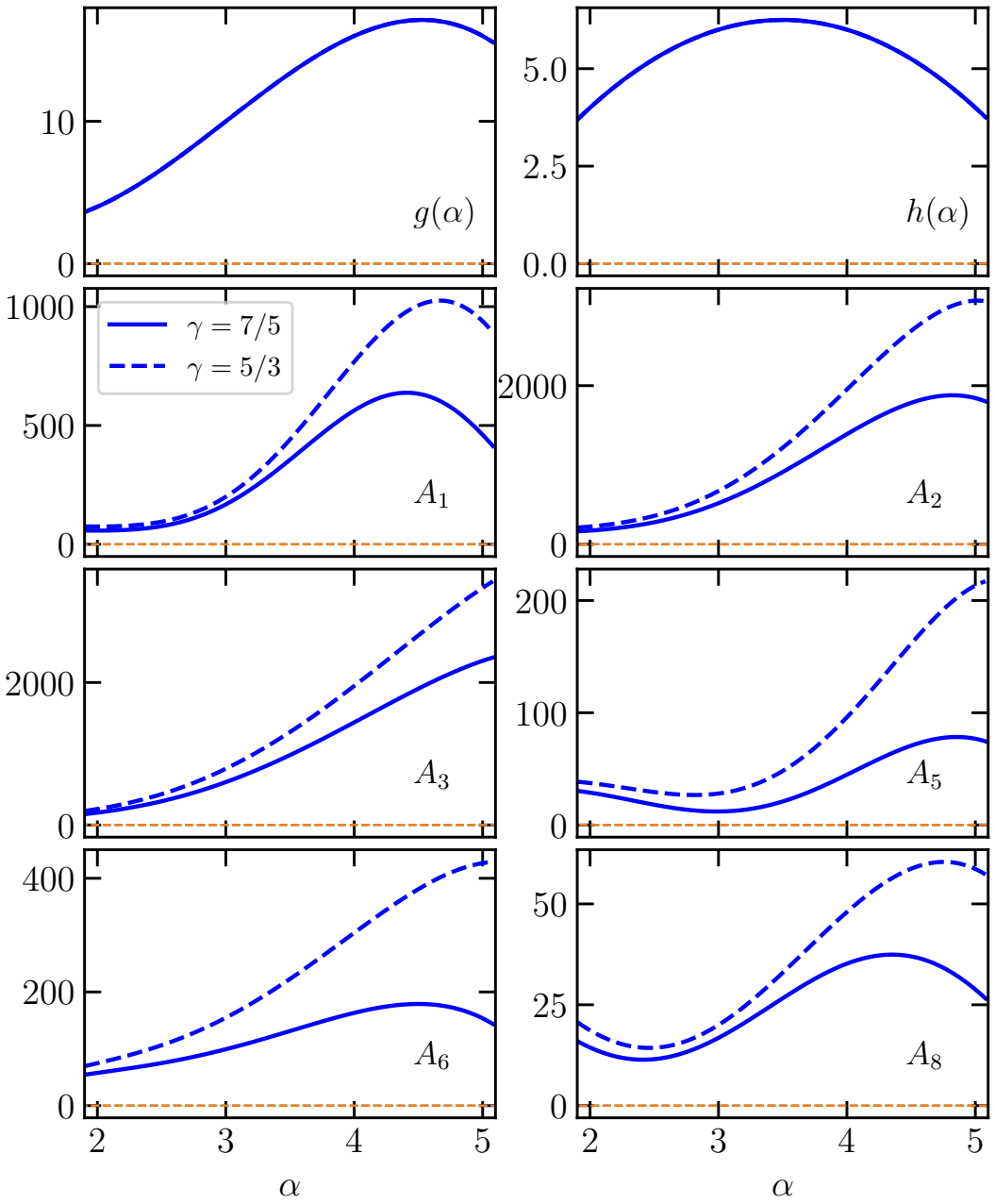

Figure A.1: Upper panels: the polynomials of α, $g(\alpha) = 16+\alpha(5-\alpha)(4-\alpha)$ (left) and $h(\alpha) = -\alpha^2+7\alpha-6$ (right) for the values of α in the range $2 < \alpha < 5$. From the middle-up to the lower panels: the polynomials A_1-A_3, A_5, A_6 and A_8 for biatomic and monoatomic adiabatic index, $\gamma = 7/5$ and $\gamma = 5/3$, for the values of α in range $2 < \alpha < 5$.

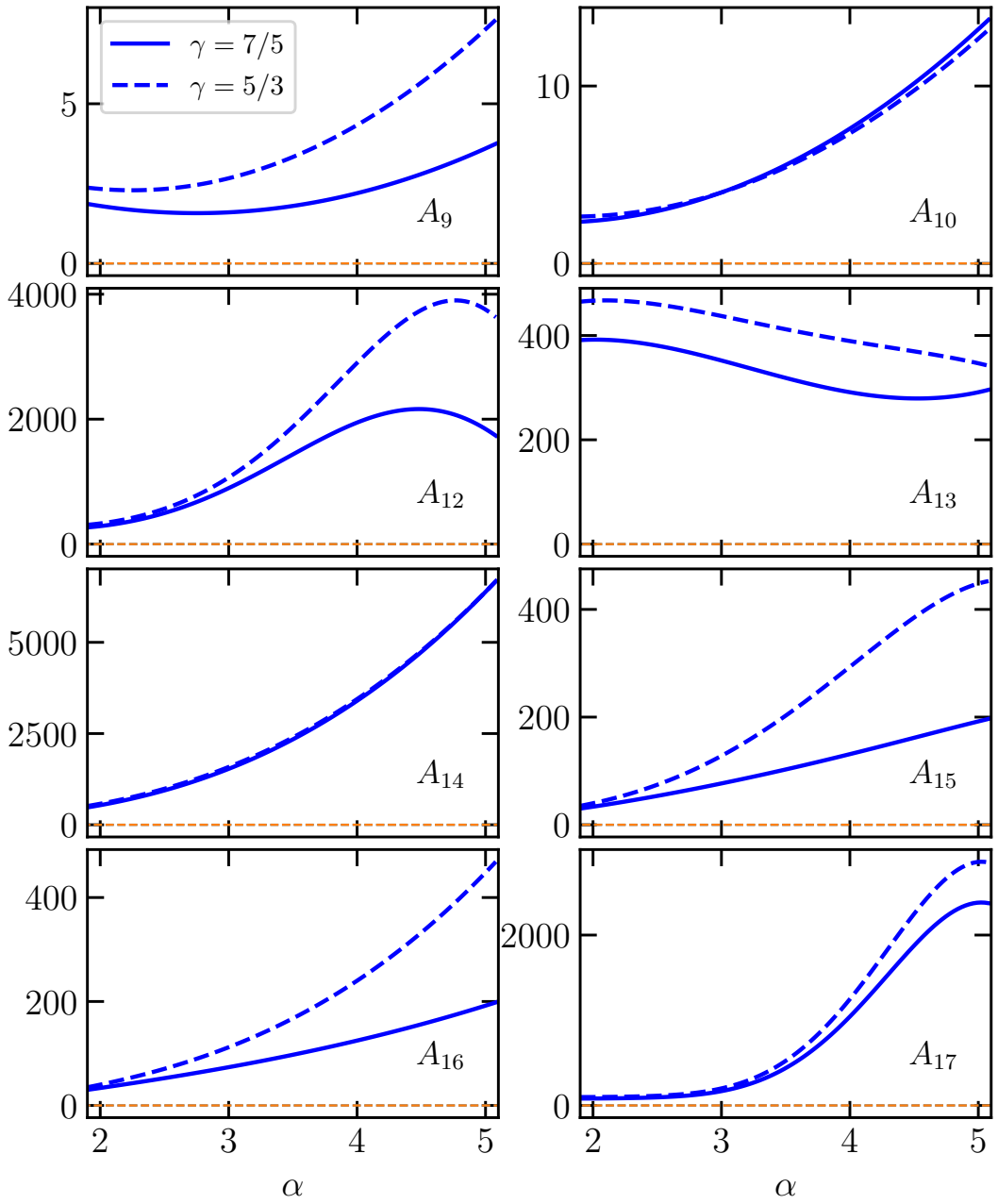

Figure A.2: The polynomials A_9, A_{10}, and A_{12}-A_{17} for biatomic and monoatomic adiabatic index, $\gamma = 7/5$ and $\gamma = 5/3$, for the values of α in the range $2 < \alpha < 5$.

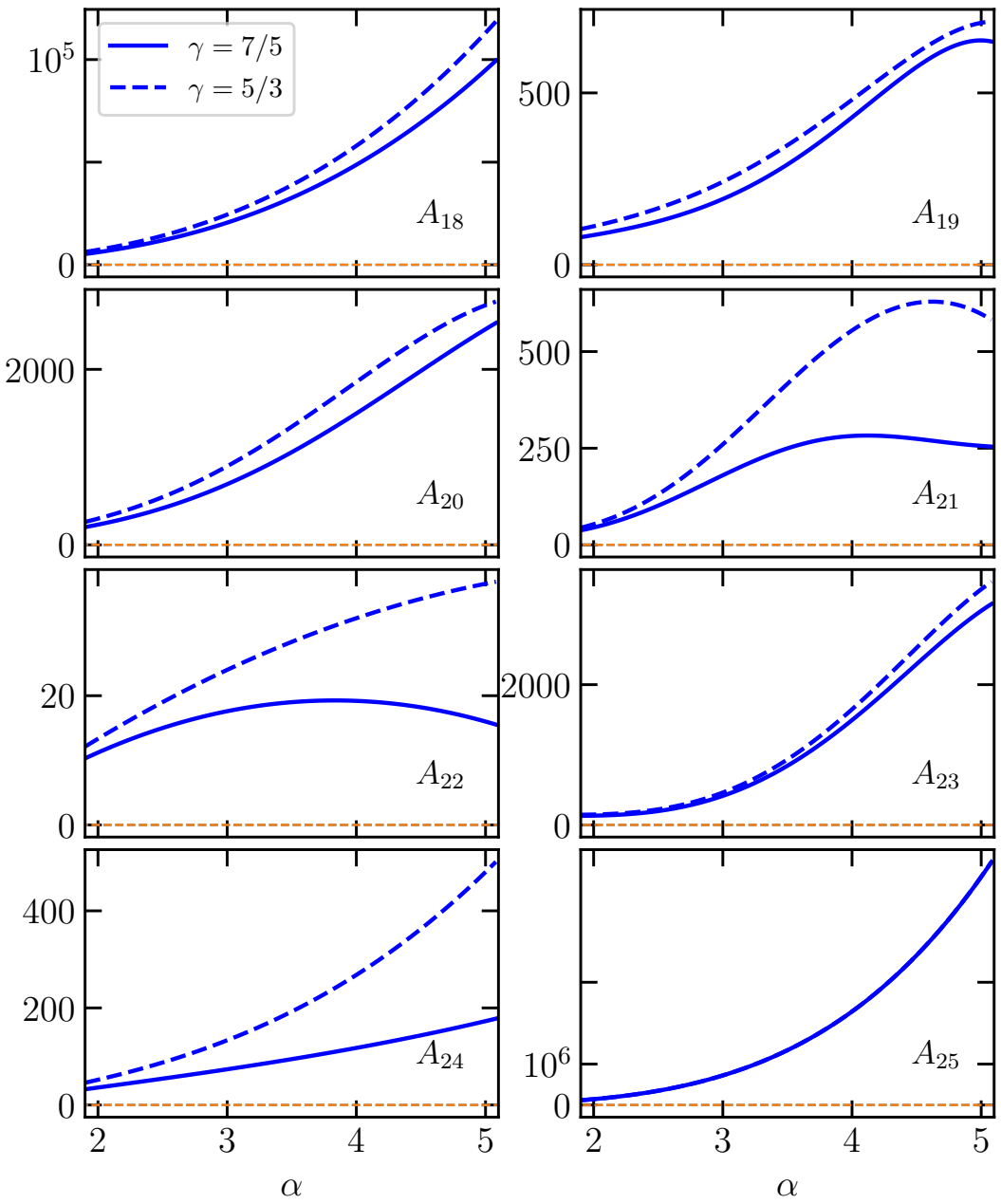

Figure A.3: The polynomials A_{18}-A_{25}, for biatomic and monoatomic adiabatic index, $\gamma = 7/5$ and $\gamma = 5/3$, for the values of α in the range $2 < \alpha < 5$.

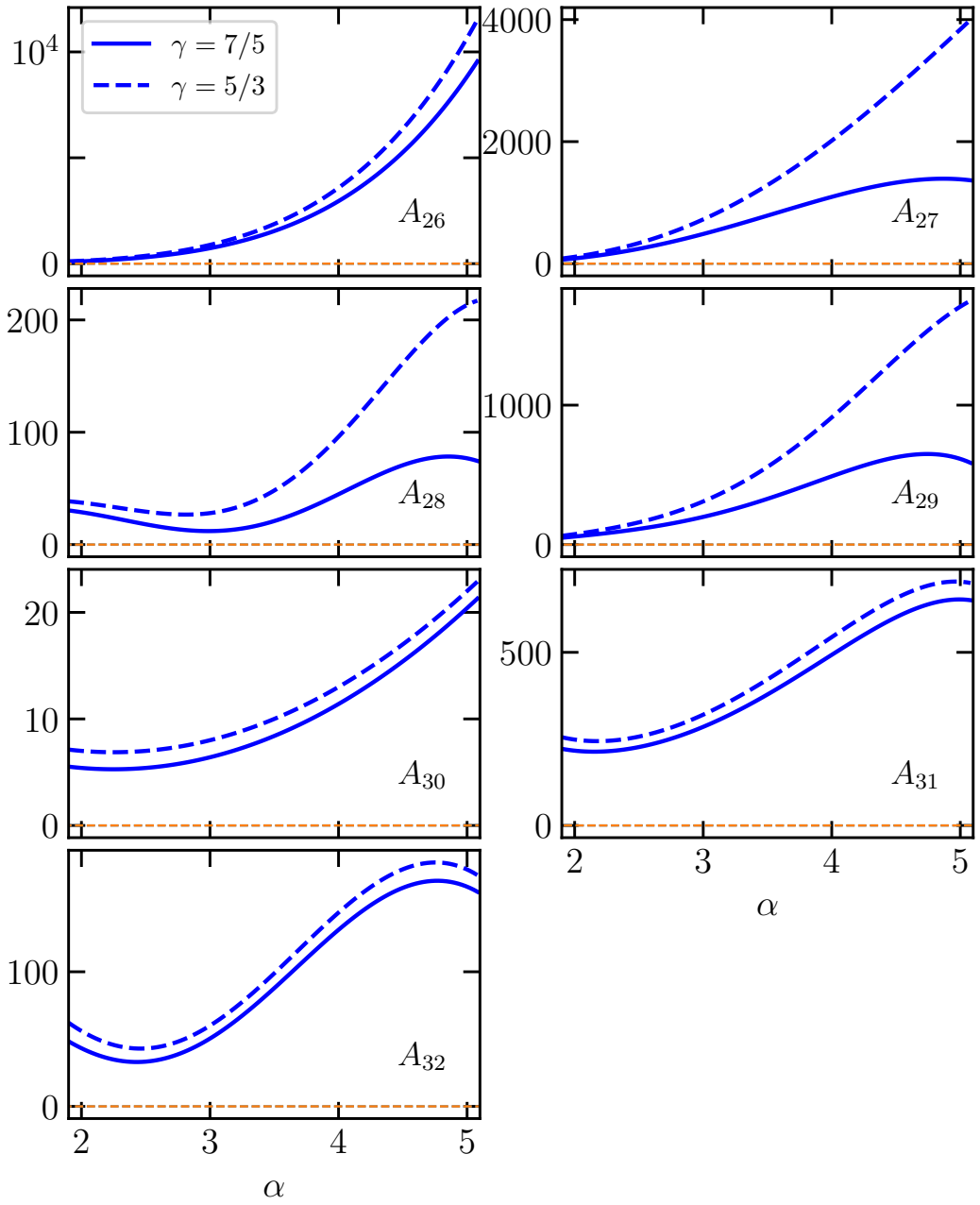

Figure A.4: The polynomials A_{26}-A_{32}, for biatomic and monoatomic adiabatic index, $\gamma = 7/5$ and $\gamma = 5/3$, for the values of α in the range $2 < \alpha < 5$.

Appendix B

In the following polynomials of α that appear in chap. 7 are listed. The polynomials B_i for $i = 1, .., 13$, $i \neq 6$ are plotted in figs B.1 and B.2, for α in range $2 < \alpha < 5$. From the graphic study we note that all they are positive in the range of α considered. For the polynomial B_6, it is easy to check analytically that it is positive for α in $2 < \alpha < 5$. The polynomials B_i for $i = 1, .., 13$, are

$B_1 = g(\alpha)(-\alpha^5 + 20\alpha^4 - 133\alpha^3 + 382\alpha^2 - 476\alpha + 224)$,

$B_2 = 4(-\alpha^6 + 19\alpha^5 - 131\alpha^4 + 433\alpha^3 - 668\alpha^2 + 468\alpha^{-}104)$,

$B_3 = 32(\alpha - 1)(\alpha^2 + 4\alpha - 3)$,

$B_4 = \alpha^6 - 14\alpha^5 + 77\alpha^4 - 212\alpha^3 + 380\alpha^2 - 408\alpha + 192$,

$B_5 = \alpha^4 - 12\alpha^3 + 55\alpha^2 + 80\alpha + 44$,

$B_6 = 8(\alpha - 1)^2(\alpha + 4)$,

$B_7 = -2\alpha^2 + 9\alpha + 23$,

$B_8 = 3\alpha^5 - 44\alpha^4 + 237\alpha^3 - 564\alpha^2 + 712\alpha - 384$,

$B_9 = 4(-5\alpha^3 + 48\alpha^2 - 75\alpha + 40)$,

$B_{10} = -3\alpha^4 + 30\alpha^3 - 71\alpha^2 + 116\alpha - 32$,

$B_{11} = 4(7\alpha^2 - 4\alpha + 7)$,

$B_{12} = -\alpha^8 + 21\alpha^7 - 187\alpha^6 + 879\alpha^5 - 2220\alpha^4 + 3084\alpha^3 - 2208\alpha^2 + 568\alpha + 96$,

$B_{13} = 4(\alpha - 1)(-\alpha^5 + 4\alpha^4 + 51\alpha^3 - 150\alpha^2 + 120\alpha - 8)$.

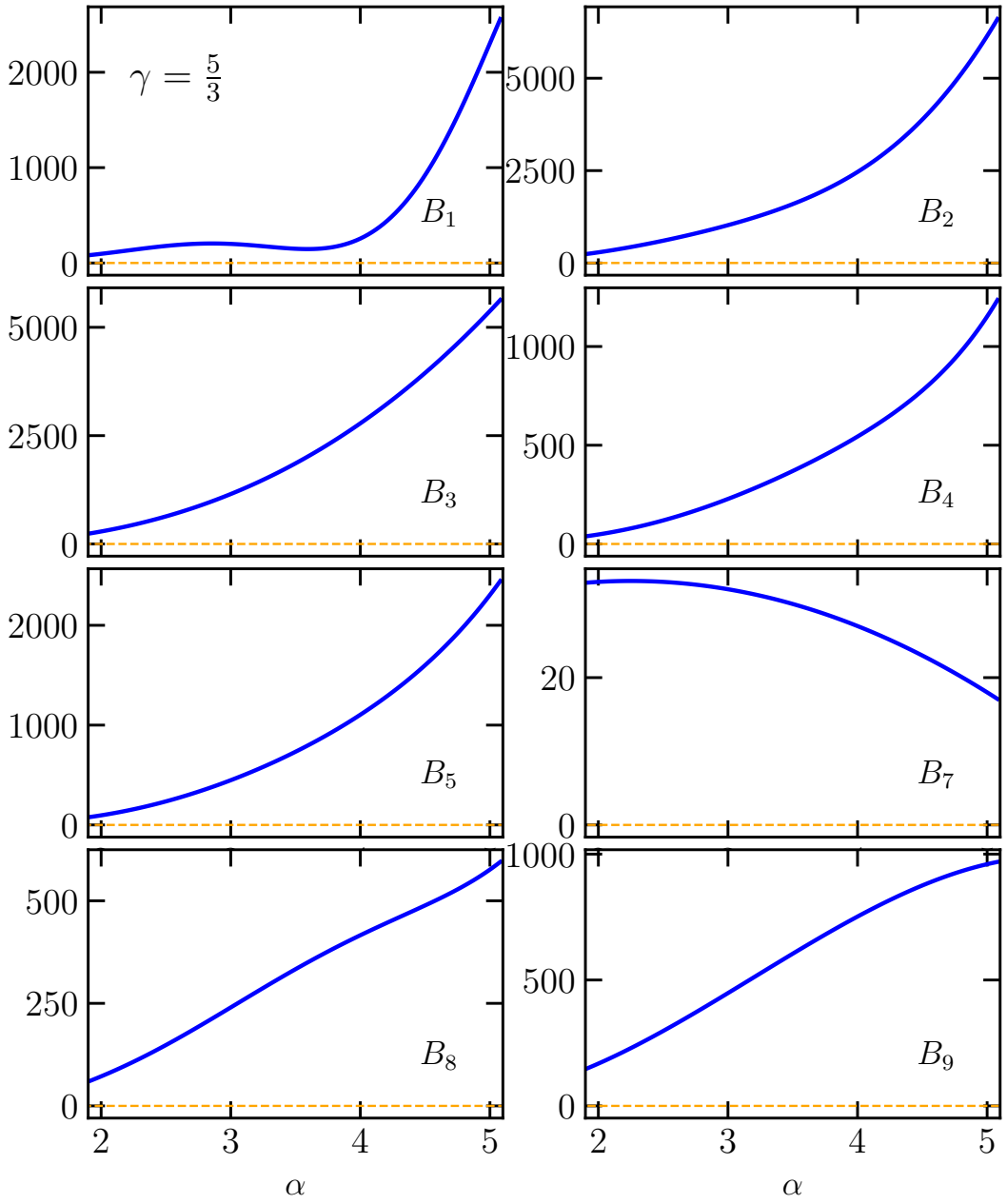

Figure B.1: The polynomials B_1-B_8, for the values of α in the range $2 < \alpha < 5$.

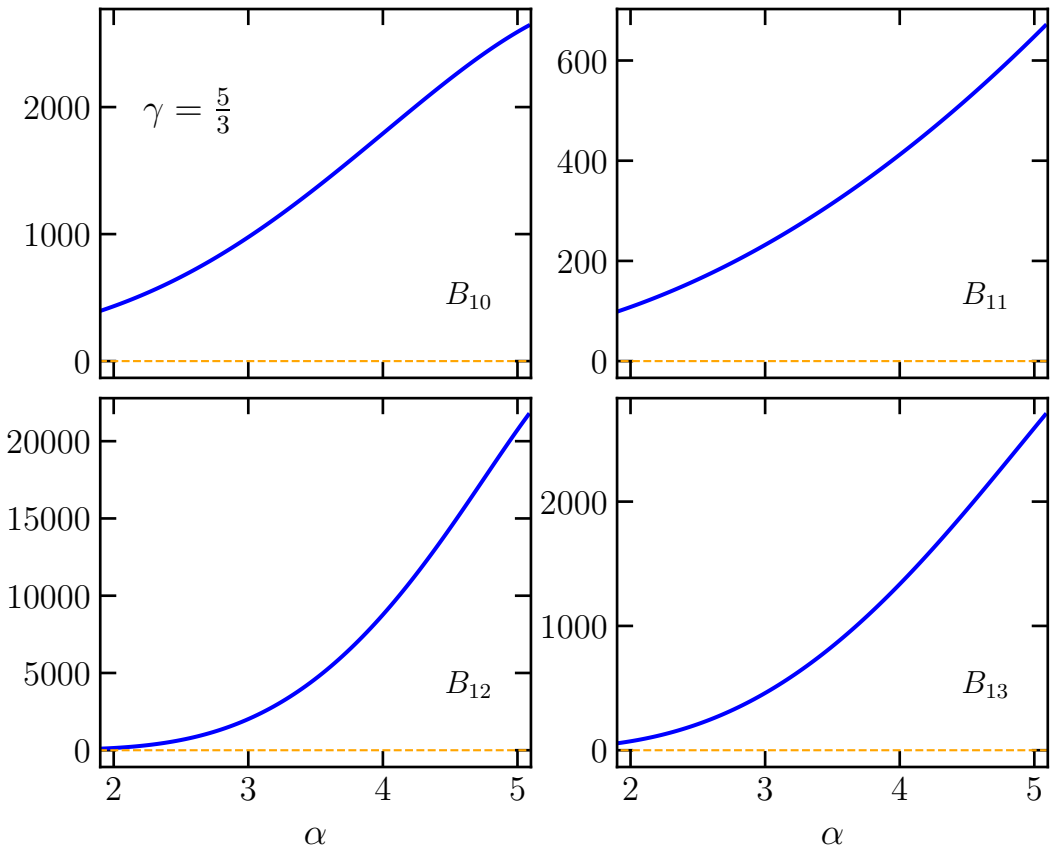

Figure B.2: The polynomials B_9-B_{15}, for the values of α in the range $2 < \alpha < 5$.

Bibliography

M. A. Abramowicz. Super-Eddington black hole accretion: Polish doughnuts and slim disks. In Andrea Merloni, Sergei Nayakshin, and Rashid A. Sunyaev, editors, *Growing Black Holes: Accretion in a Cosmological Context*, pages 257–273, January 2005.

M. A. Abramowicz, M. Calvani, and L. Nobili. Thick accretion disks with super-Eddington luminosities. *ApJ*, 242:772–788, December 1980.

R. R. J. Antonucci and J. S. Miller. Spectropolarimetry and the nature of NGC 1068. *ApJ*, 297:621–632, October 1985.

S. Balbus. Hydrodyamics: lecture notes, Formation Interuniversitaire de Physique. *https://www2.physics.ox.ac.uk/contacts/people/balbus* , 2017.

S. A. Balbus and J. F. Hawley. A powerful local shear instability in weakly magnetized disks. I - Linear analysis. II - Nonlinear evolution. *ApJ*, 376:214–233, July 1991.

Steven A. Balbus. General Local Stability Criteria for Stratified, Weakly Magnetized Rotating Systems. *ApJ*, 453:380, November 1995.

M. Barnabè, L. Ciotti, F. Fraternali, and R. Sancisi. Hydrostatic models for the rotation of extra-planar gas in disk galaxies. *A&A*, 446(1):61–69, January 2006.

J. Binney and S. Tremaine. *Galactic Dynamics: Second Edition*. Princeton University Press, 2008.

S. Chandrasekhar. The Stability of Non-Dissipative Couette Flow in Hydromagnetics. *Proceedings of the National Academy of Science*, 46(2):253–257, Feb 1960.

L. Ciotti and G. Bertin. A simple method to construct exact density-potential pairs from a homeoidal expansion. *A&A*, 437(2):419–427, July 2005.

C. Clarke and B. Carswell. *Principles of Astrophysical Fluid Dynamics*. January 2014.

F. Combes, S. García-Burillo, A. Audibert, L. Hunt, A. Eckart, S. Aalto, V. Casasola, F. Boone, M. Krips, S. Viti, K. Sakamoto, S. Muller, K. Dasyra, P. van der Werf, and S. Martin. ALMA observations of molecular tori around massive black holes. *A&A*, 623:A79, March 2019.

Enrico Fermi. *Thermodynamics*. 1956.

Richard P. Feynman. *Feynman lectures on physics. Volume 2: Mainly electromagnetism and matter*. 1964.

I. García-Bernete, C. Ramos Almeida, A. Alonso-Herrero, M. J. Ward, J. A. Acosta-Pulido, M. Pereira-Santaella, A. Hernán-Caballero, A. Asensio Ramos, O. González-Martín, N. A. Levenson, S. Mateos, F. J. Carrera, C. Ricci, P. Roche, I. Marquez, C. Packham, J. Masegosa, and L. Fuller. Torus model properties of an ultra-hard X-ray selected sample of Seyfert galaxies. *MNRAS*, 486(4):4917–4935, July 2019.

L. Mestel. On the galactic law of rotation. *MNRAS*, 126:553, January 1963.

Ramesh Narayan and Insu Yi. Advection-dominated Accretion: Self-Similarity and Bipolar Outflows. *ApJ*, 444:231, May 1995a.

Ramesh Narayan and Insu Yi. Advection-dominated Accretion: Underfed Black Holes and Neutron Stars. *ApJ*, 452:710, October 1995b.

Carlo Nipoti. *Lecture notes, Gas dynamics in galaxies*. 2019.

B. Paczyński. Thick Accretion Disks around Black Holes (Karl-Schwarzschild-Vorlesung 1981). *Mitteilungen der Astronomischen Gesellschaft Hamburg*, 57: 27, January 1982.

B. Paczyński and P. J. Wiita. Thick Accretion Disks and Supercritical Luminosities. *A&A*, 88:23, August 1980.

Bohdan Paczyński. Advection Dominated Accretion Flows. A Toy Disk Model. *ACTA*, 48:667–676, December 1998.

M. J. Rees, M. C. Begelman, R. D. Blandford, and E. S. Phinney. Ion-supported tori and the origin of radio jets. , 295(5844):17–21, January 1982.

N. I. Shakura and R. A. Sunyaev. Black holes in binary systems. Observational appearance. *A&A*, 24:337–355, January 1973.

F. H. Shu. *The physics of astrophysics. Volume II: Gas dynamics.* 1992.

Mattia C. Sormani, Emanuele Sobacchi, Gabriele Pezzulli, James Binney, and Ralf S. Klessen. Models of rotating coronae. *MNRAS*, 481(3):3370–3381, December 2018.

Jean-Louis Tassoul. *Theory of rotating stars*. 1978.

C. Megan Urry and Paolo Padovani. Unified Schemes for Radio-Loud Active Galactic Nuclei. , 107:803, September 1995.